NLO QCD Corrections To Higgs Radiation Off Heavy Quarks At Hadron Colliders

Dissertation

zur Erlangung des Doktorgrades

des Fachbereichs Physik

der Universität Hamburg

vorgelegt von

Benedikt Plümper

aus Soest

Hamburg

2001

Gutachter der Dissertation:	Prof. Dr. P.M. Zerwas Prof. Dr. B.A. Kniehl
Gutachter der Disputation:	Prof. Dr. P.M. Zerwas Prof. Dr. J. Bartels
Datum der Disputation:	21.01.2002
Dekan des Fachbereichs Physik und Vorsitzender des Promotionsausschusses:	Prof. Dr. F.-W. Büßer

Abstract

This thesis is the first step towards a solid theoretical description of Higgs radiation off heavy quarks at hadron colliders, $P\bar{P}/PP \to Q\bar{Q}H$. For Higgs masses roughly below 120 GeV $t\bar{t}H$ production can probably increase the Higgs discovery potential at the TEVATRON and represents a substantial contribution to the Higgs signal at the LHC. Providing that the branching ratio of the decay of the Higgs boson into $b\bar{b}$ is known, this process offers in addition the opportunity of a first direct measurement of the top Yukawa coupling which allows an insight into the generation of fermion masses.
The calculation of the next-to-leading order QCD corrections to $Q\bar{Q}H$ production is presented in this thesis. Including these corrections drastically reduces the dependence of the cross section on the renormalization and factorization scales, rendering the prediction theoretically reliable. At the central scale, which is defined as half the threshold energy, the next-to-leading order QCD corrections slightly reduce the cross section of $t\bar{t}H$ production at the TEVATRON by roughly 20% and increase it by the same amount at the LHC.
The prediction of the cross section of $b\bar{b}H$ production is more involved due to the large mass splitting of the bottom quark and the Higgs boson. First numerical results of the next-to-leading order predictions of the corresponding cross section are presented.

Zusammenfassung

Diese Doktorarbeit ist der erster Schritt zu einer fundierten theoretischen Beschreibung der Higgsstrahlung von schweren Quarks an Hadronbeschleunigern, $P\bar{P}/PP \to Q\bar{Q}H$. Für Higgsmassen unterhalb von ungefähr 120 GeV kann $t\bar{t}H$-Produktion vermutlich die Möglichkeit der Higgsentdeckung am TEVATRON erhöhen, und sie stellt einen bedeutenden Beitrag zum Higgssignal am LHC dar. Vorausgesetzt, daß das Verzweigungsverhältnis des Higgsbosonzerfalls in $b\bar{b}$ bekannt ist, bietet dieser Prozess außerdem die Möglichkeit einer ersten direkten Messung der Top-Yukawa-Kopplung, die Einsichten in den Erzeugungsmechanismus von Fermionmassen erlaubt.
Die Berechnung der QCD-Korrekturen zur $Q\bar{Q}H$-Produktion in nächst höherer Ordnung wird in dieser Doktorarbeit präsentiert. Die Einbeziehung dieser Korrekturen reduziert die Abhängigkeit des Wirkungsquerschnittes von den Renormierungs- und Faktorisierungskalen drastisch, was die Vorhersage theoretisch verlässlich macht. An der zentralen Skala, die als halbe Schwellenenergie definiert ist, reduzieren die QCD-Korrekturen in nächst höherer Ordnung den Wirkungsquerschnitt der $t\bar{t}H$-Produktion am TEVATRON um 20% und erhöhen ihn um den gleichen Betrag am LHC.
Die Vorhersagen des Wirkungsquerschnittes der $b\bar{b}H$-Produktion ist komplizierter wegen der großen Massenaufspaltung zwischen dem Bottomquark und dem Higgsboson. Erste numerische Resultate der Vorhersage des entsprechenden Wirkungsquerschnittes in nächst höherer Ordnung werden vorgestellt.

Contents

1 Introduction **1**

2 General Framework **5**

2.1 Particles and Forces 5

2.2 The Higgs–Kibble Mechanism 7

2.3 The Generation of Fermion Masses 9

2.4 Next-to-Leading Order Corrections 10

2.5 Renormalization 12

2.6 The Parton Model 15

2.7 Factorization 15

3 Conventions and LO Cross Section **19**

3.1 Notations and Conventions 19

3.2 Standard Matrix Elements 21

3.3 The Input Parameters 22

3.4 The LO Predictions for $P\bar{P}/PP \to t\bar{t}H$ 23

4 Virtual Corrections **25**

4.1 Preliminaries 25

4.2 The Renormalization Constants 26

4.3 Five-Point Functions 27

4.4 The Endpoint Contribution 30

4.5 Avoiding Numerical Instabilities 33

4.6 The Coulomb Singularity 34

5 Real Corrections **37**

5.1 General Remarks . . . 37
5.2 The Four-Particle Phase Space . . . 38
5.3 The Dipole Subtraction Formalism . . . 39
5.4 The Subtraction Function . . . 41
5.5 The Readded Subtraction Function . . . 43
5.6 The Slicing Method . . . 45
5.7 Leading Threshold Logarithms . . . 47

6 Numerical Results for $t\bar{t}H$ Production **49**

6.1 The NLO Cross Section at the TEVATRON . . . 49
6.2 The NLO Cross Section at the LHC . . . 52
6.3 Distributions . . . 55
6.4 Leading Threshold Corrections . . . 60

7 Outlook to $b\bar{b}H$ Production **63**

7.1 Discussion of Large Logarithmic Corrections . . . 63
7.2 $b\bar{b}H$ Production at the TEVATRON . . . 64
7.3 $b\bar{b}H$ Production at the LHC . . . 65

8 Summary and Conclusions **71**

A The Standard Matrix Elements **73**

A.1 The $q\bar{q}$ Channel . . . 73
A.2 The gg Channel . . . 74

B The LSZ Factors **77**

C The One-Loop Integrals **79**

C.1 Notations . . . 79
C.2 The Divergent Scalar Three- and Four-Point Integrals . . . 81
C.3 The Singularity Structure . . . 82

D Details of the Subtraction Formalism **85**

D.1 The Colour Operators 85

D.2 Final-State Emitter and Final-State Spectator 85

D.3 Final-State Emitter and Initial-State Spectator 87

D.4 Initial-State Emitter and Final-State Spectator 88

D.5 Initial-State Emitter and Initial-State Spectator 89

Bibliography **91**

Chapter 1

Introduction

The Standard Model (SM) of high-energy physics [1–9] (for a review see Ref. [10]) has widely been tested and verified in parts up to the level of quantum corrections. The experiments performed at LEP1 and SLC provided precise information about the couplings of the light fermions to the weak gauge bosons [11]. Measurements of the triple-gauge self-couplings became possible at LEP2 [11]. All results can be explained within the SM. Despite all success, one part of the SM has not been established experimentally yet, the mechanisms of electroweak symmetry breaking. The Higgs–Kibble mechanism [12–17], implemented in the SM, predicts the existence of a new particle, the Higgs boson, which up to now has never been detected. Therefore the search for the Higgs boson is one of the key issues of existing and future collider experiments [18, 19]. The facilities which are available for this purpose within the next decade are the proton–antiproton collider TEVATRON [20] with a center-of-mass (CM) energy of 2 TeV and the proton–proton collider LHC [21–23] with a CM energy of 14 TeV.

The mass of the Higgs boson is one of the free parameters of the SM and the last that has not been measured so far. This ignorance complicates the search for the Higgs particle. However, the range of this parameter can be restricted. The strongest limits on the Higgs mass have been obtained from the LEP experiments. Their direct search leads to a lower bound of 114.1 GeV at 95% Confidence Level (CL) [24]. However, LEP also provides tantalising hints that the Higgs boson is light enough to be found at the TEVATRON or later at the LHC. First of all, evidences occurred for a Higgs mass around 115.6 GeV [24]. In addition, if assuming that the SM is the correct theory to describe the electroweak interaction, electroweak precision tests lead to a Higgs mass below 212 GeV at 95% CL [25, 26]. This limit is obtained by exploiting the Higgs-mass dependence of electroweak radiative corrections. However, in models beyond the SM it is not fully conclusive [27–29].

At the TEVATRON a Higgs boson can be discovered at the 5σ level up to a mass of 120 GeV. Evidences at the 3σ level can be obtained up to a Higgs mass of 180 GeV, and the Higgs particle can be excluded up to 190 GeV with 95% CL [20]. At the LHC a Higgs boson can be discovered for all relevant Higgs masses ($\lesssim 1$ TeV) [21].

At the LHC the largest production channel for a Higgs particle is gluon fusion, $gg \to H$ [30–32]. Unfortunately, this signal is plagued by a very large background. The next largest cross section is given by weak-boson fusion [33–36], $qq \to qqV^*V^* \to qqH$, where V is the W or the Z boson, followed by Higgs-strahlung off W, Z bosons [37–39], $q\bar{q} \to V^* \to VH$. The strength of Higgs radiation off heavy quarks [40–42], $q\bar{q}, gg \to Q\bar{Q}H$ with $Q = b, t$, is of the same order of magnitude as Higgs-strahlung. At the TEVATRON the largest production channel is again gluon fusion. The cross sections of weak-boson fusion and Higgs-strahlung are of the same order of magnitude, while Higgs radiation off heavy quarks is much smaller than the previous production channels.

A light Higgs boson with a mass below 140 GeV decays dominantly into $b\bar{b}$ [43, 44]. The subdominant channels are $\tau^+\tau^-$ and $c\bar{c}$ with branching ratios of a few per cent. The loop-mediated decay into gg is of the same strength as the preceding ones but is not suited for the experimental search due to large background event rates. For masses above 140 GeV the decay into heavy vector bosons develops the largest branching ratios. The $t\bar{t}$ channel opens for masses larger than 350 GeV. A window between 80 GeV and 150 GeV opens for the rare decay into $\gamma\gamma$ with a branching ratio of order 10^{-3}. Nevertheless, this channel is experimentally very promising.

Higgs radiation off heavy quarks [40–42], $P\bar{P}/PP \to Q\bar{Q}H + X$, is an important channel for Higgs physics, although its cross section is roughly two orders of magnitude smaller than the dominant production channel. At the LHC $t\bar{t}H$ production, with the Higgs boson subsequently decaying into $b\bar{b}$, provides a major discovery channel for Higgs masses below 120 GeV and contributes substantially to the 5σ discovery contour. Since the top quarks predominantly decay into bottom quarks, the signal consists of four b quarks and two W's. If one of the latter is required to decay leptonically, a single charged lepton with high transverse momentum and missing energy due to the escaping neutrino can be used for tagging [45]. This signal has a very low background and is hence well suited for the experimental search since the ratio of the signal rates to the background rates is essential for the data analysis. In addition, $t\bar{t}H$ production contributes to the signal of the rare Higgs decay into $\gamma\gamma$. This signal is very promising for Higgs masses below 160 GeV. For the TEVATRON it is not yet clear whether sufficiently many events for the Higgs radiation off top quarks can be extracted. A recent study [46] concludes that this channel can be seen, but the cross section used in this work seems to be overestimated.

In the SM, the coupling of the bottom quark to the Higgs is a factor m_b/m_t smaller than the one of the top quark. However, in supersymmetric extensions the $b\bar{b}H$ coupling can be strongly enhanced [47]. The Minimal Supersymmetric Standard Model (MSSM) contains two Higgs doublets, one giving mass to the up-type fermions and the other to the down-type fermions. Consequently the physical spectrum includes five Higgs bosons. The ratio of the two vacuum expectation values is denoted by the parameter $\tan\beta$. In scenarios with large values of $\tan\beta$ the $b\bar{b}H$ coupling can be of the same strength as the $t\bar{t}H$ coupling. Therefore, Higgs radiation off bottom quarks plays a more important rôle in supersymmetric models than in the SM. For the bottom quarks additional complications

in the calculation of the cross section occur. The smallness of the bottom mass leads to radiative corrections involving large logarithms which potentially cause problems with the perturbative description of the process in the parton model.

Despite its importance for the discovery of the Higgs boson, the $Q\bar{Q}H$ production offers further opportunities. In the Born approximation of this process the Higgs couples solely to the heavy quark. Presumed that the branching ratio of the decay of the Higgs boson into $b\bar{b}$ is known, this reaction therefore permits a measurement of the corresponding Yukawa coupling with an expected uncertainty of roughly 15% [45,48]. Within the SM this coupling is fixed by the quark mass and the vacuum expectation value of the Higgs field due to the Higgs–Kibble mechanism. Hence measuring these three quantities independently provides an experimental test of the Higgs sector of the SM. If the Higgs is too light to decay into a pair of top quarks, $t\bar{t}H$ production is the only way to determine the Yukawa coupling of the top quark directly. As mentioned above, in the MSSM the $Q\bar{Q}H$ coupling involves $\tan\beta$. Therefore this additional quantity has also to be determined independently to ensure the test of the Higgs sector. Due to the intrinsic uncertainties of hadron colliders, a precise measurement of the Yukawa coupling of the heavy quarks will not be possible until the next generation of e^+e^- colliders. Again, Higgs radiation off heavy quarks [49–53] plays an important rôle for this purpose.

Aside from the Yukawa coupling, $Q\bar{Q}H$ production is a pure process of Quantum Chromodynamics (QCD) in Leading Order (LO). The LO prediction for its cross section is plagued by sizable uncertainties. As will be shown later, the uncertainty due to the renormalization and the factorization scale dependence is roughly a factor two to three for the cross section at LO. Hence, the Next-to-Leading Order (NLO) corrections are inevitable for a reliable prediction of the cross section, because they reduce the scale dependence significantly. An estimate of these corrections was obtained in the Effective Higgs–Approximation (EHA) in Ref. [54]. Since this approximation is only valid if the Higgs mass is much smaller than the quark mass, it is considered to work at most for $t\bar{t}H$ production. The quality of the approximation is not clear at all and therefore the full calculation is needed.

The topic of this thesis is to provide a solid theoretical prediction for the cross section of Higgs radiation off heavy quarks. For this purpose the calculation of the full NLO QCD corrections, including the applied techniques and numerical results, is presented. In addition, the special complications for treating $b\bar{b}H$ production are discussed. The results for $t\bar{t}H$ production have recently been published [55] (a longer paper is in preparation [56]). Parts of them have independently been worked out by another group [57, 58]. The results of the two groups have been compared before publication, and they agree.

The calculation of the NLO QCD corrections to the processes $P\bar{P}/PP \to Q\bar{Q}H$ is quite involved. The complexity in the virtual corrections is running up to pentagon diagrams. The treatment of infrared divergent five-point functions is available in the literature only for the case of massless particles [59, 60], but not for the case of several internal and external masses. In addition, the numerical evaluation of five-point tensor integrals is not straight forward, since the usual covariant decomposition becomes unstable at the phase

space boundary. A method to stabilize the algorithm in this phase space region had to be developed. Due to the large number of diagrams and the appearance of four- and five-point functions, the separation of the infrared (soft and collinear) divergences from the virtual corrections is quite involved. This separation is also a problem for the real corrections due to the complexity of the matrix element. An extension [61] of the dipole subtraction method [62, 63], which includes massive QCD partons, was adopted to extract the divergences of the real corrections and to combine them with the ones of the virtual corrections.

The thesis is organized as follows: After setting the general framework in Chapter 2, the conventions, input parameters, and the LO predictions are given in Chapter 3. The virtual and the real corrections are treated in Chapter 4 and 5, respectively. The numerical results for the NLO predictions for $t\bar{t}H$ production and the leading threshold logarithms are presented in Chapter 6. Chapter 7 provides first numerical results of the calculation of the cross section for $b\bar{b}H$ production and a discussion about the treatment of the large logarithms containing the small bottom mass. The conclusions are drawn in Chapter 8. Some details of special interest are presented in the appendices.

Chapter 2

General Framework

2.1 Particles and Forces

It is commonly believed that the appropriate way to describe the fundamental forces in nature is the concept of a *quantum field theory with local gauge invariance* [64–67]. In such a theory the Lagrangian $\mathcal{L}$ describing the kinematics and interactions of the fundamental particles is invariant under a local gauge transformation $U(\theta_i(x))$ which acts on the fields $\Psi_l(x)$ of the theory:

$$\mathcal{L}[U(\theta_i(x))\Psi_l(x)] \;=\; \mathcal{L}[\Psi_l(x)]. \tag{2.1}$$

Here $\theta_i(x)$ are the continuous local parameters of a Lie group, called *gauge group*, with generators T_i. The gauge invariance of the theory requires one vector field for each generator. These fields describe vector particles, the *gauge bosons*, which mediate the force described by the gauge theory.

Following this idea the Standard Model (SM) of electroweak [1–3] and strong [4–9] interaction was developed in the last decades. The gauge group of the SM is $G_{SM} = SU(3)_C \otimes SU(2)_W \otimes U(1)_Y$. The first group, $SU(3)_C$, is the non-Abelian symmetry group of Quantum Chromodynamics (QCD), the second one, $SU(2)_W$, is the non-Abelian symmetry group of the weak isospin, and the last one, $U(1)_Y$, is the Abelian symmetry group of the weak hypercharge. The corresponding vector fields are the eight gluon fields $G^a_\mu (a = 1, \ldots, 8)$ of QCD, the three vector fields $W^i_\mu\,(i = 1, 2, 3)$, and the gauge field B_μ of the Abelian $U(1)_Y$.

The physical mass eigenstates consist of the charged bosons $W^\pm$ and the neutral bosons Z and A. The fields that correspond to the $W^\pm$ are superpositions of the first two components of the isospin triplet W^i_μ,

$$W^\pm_\mu \;=\; \frac{1}{\sqrt{2}}\left(W^1_\mu \mp i\, W^2_\mu\right), \tag{2.2}$$

while the fields corresponding to Z and A result from a rotation of the fields B_μ and W^3_μ by the *weak mixing angle* θ_W,

$$\begin{pmatrix} A_\mu \\ Z_\mu \end{pmatrix} = \begin{pmatrix} \cos\theta_W & \sin\theta_W \\ -\sin\theta_W & \cos\theta_W \end{pmatrix} \begin{pmatrix} B_\mu \\ W^3_\mu \end{pmatrix}. \tag{2.3}$$

The Lagrangian of the gauge sector is gauge-invariant and contains three parts corresponding to the three subgroups of G_{SM},

$$\mathcal{L}_{\text{gauge}} = -\frac{1}{4} G^a_{\mu\nu}\, G^{a,\mu\nu} - \frac{1}{4} W^i_{\mu\nu}\, W^{i,\mu\nu} - \frac{1}{4} B_{\mu\nu}\, B^{\mu\nu}, \tag{2.4}$$

with the field-strength tensors

$$G^a_{\mu\nu} = \partial_\mu G^a_\nu - \partial_\nu G^a_\mu - g_s\, f^{abc}\, G^b_\mu\, G^c_\nu, \tag{2.5}$$
$$W^i_{\mu\nu} = \partial_\mu W^i_\nu - \partial_\nu W^i_\mu - g_W\, \epsilon^{ijk}\, W^j_\mu\, W^k_\nu, \tag{2.6}$$
$$B_{\mu\nu} = \partial_\mu B_\nu - \partial_\nu B_\mu. \tag{2.7}$$

The quantities g_s and g_W are the couplings of $SU(3)_C$ and $SU(2)_W$, respectively, and f^{abc} and ϵ^{ijk} denote the structure constants of the two groups.

The matter content of the SM consists of two basic constituents: *leptons* and *quarks*. The left- and the right-handed components of these spin-$\frac{1}{2}$ fermions are treated differently by the $SU(2)_W \otimes U(1)_Y$ subgroup as required by the experimentally observed parity violation [68]. While the left-handed parts are $SU(2)_W$ doublets, the right-handed parts are weak-isospin singlets. Both leptons and quarks carry weak isospin and weak hypercharge but only the latter carry colour charge and therefore couple to the gluons of QCD. Leptons as well as quarks are grouped into three families. The members of two different families have the same quantum numbers but differ in mass.

Although experimental evidences for neutrino oscillations, and therefore for neutrino masses, exist [69, 70] these effects can safely be neglected in the context of collider experiments which are of interest in this work. In this approximation the right-handed component of a massless neutrino decouples completely from all particles of the SM and can therefore be omitted.

The Lagrangian of the fermionic part of the SM is also gauge-invariant and can be written as

$$\mathcal{L}_{\text{fermion}} = \sum_{l=1}^{3} \bar{\Psi}^l_L \not{D} \Psi^l_L + \sum_{q=1}^{3} \bar{\Psi}^q_L \not{D} \Psi^q_L + \sum_{e=1}^{3} \bar{\Psi}^e_R \not{D} \Psi^e_R + \sum_{u=1}^{3} \bar{\Psi}^u_R \not{D} \Psi^u_R + \sum_{d=1}^{3} \bar{\Psi}^d_R \not{D} \Psi^d_R. \tag{2.8}$$

The $\Psi_{L,R}$ denote the three families which are listed in Table 2.1 together with their quantum numbers for the $SU(2)_W \otimes U(1)_Y$ subgroup. The summation in Eq. (2.8) is done over all

				I	I_3	Y	Q
$\Psi_L^l =$	$\begin{pmatrix} \nu_e \\ e \end{pmatrix}_L$	$\begin{pmatrix} \nu_\mu \\ \mu \end{pmatrix}_L$	$\begin{pmatrix} \nu_\tau \\ \tau \end{pmatrix}_L$	$1/2$ $1/2$	$1/2$ $-1/2$	-1 -1	0 -1
$\Psi_R^e =$	e_R	μ_R	τ_R	0	0	-2	1
$\Psi_L^q =$	$\begin{pmatrix} u \\ d \end{pmatrix}_L$	$\begin{pmatrix} c \\ s \end{pmatrix}_L$	$\begin{pmatrix} t \\ b \end{pmatrix}_L$	$1/2$ $1/2$	$1/2$ $-1/2$	$1/3$ $1/3$	$2/3$ $-1/3$
$\Psi_R^u =$	u_R	c_R	t_R	0	0	$4/3$	$2/3$
$\Psi_R^d =$	d_R	s_R	b_R	0	0	$-2/3$	$-1/3$

Table 2.1: The quantum numbers of leptons and quarks.

leptons l and all quarks q, the latter includes the summation over the colour degrees. D_μ is the covariant derivative which depends on the fermion quantum numbers,

$$D_\mu \;=\; \partial_\mu + i\, g_s\, G_\mu^a\, t_a + i\, g_W\, W_\mu^i\, I_i + i\, g_Y\, B_\mu\, \frac{Y}{2}, \tag{2.9}$$

where t_a, I_i, and Y are the generators of the three gauge groups and g_Y is the coupling of $U(1)_Y$.

2.2 The Higgs–Kibble Mechanism

Due to the different quantum numbers of the left- and right-handed particles it is not possible to add an explicit mass term for the fermions to the Lagrangian without breaking the gauge symmetry. A mass term for the vector bosons is not gauge-invariant either. The discrepancy between the restriction to massless particles and the experimentally observed masses of the fermions and the weak gauge bosons are overcome by the *Higgs–Kibble mechanism* [12–17] which extends the idea of Spontaneous Symmetry Breaking (SSB).

If a Lagrangian is invariant under a continuous symmetry transformation, its ground state $|0\rangle$ may be invariant or not. A generator T for which $|0\rangle$ is not invariant is called a *broken generator*. The Nambu-Goldstone theorem [71–73] states that for each broken generator of a global symmetry group there exists a massless boson, called *Goldstone boson*. If there is at least one broken generator the symmetry is said to be *broken spontaneously*.

The introduction of a Higgs-sector is up to now the only known way to implement masses of gauge bosons into a local gauge theory leading to a weakly interacting perturbative theory. Scalar fields interact with each other in such a way that the ground state acquires a non-zero field-strength, breaking the electroweak symmetries spontaneously. Due to

gauge invariance the Goldstone bosons are not physical scalar particles but deliver the longitudinal part of the gauge bosons which are now massive.

The minimal implementation of the Higgs–Kibble mechanism, as in the SM, requires a single complex $SU(2)_W$ doublet $\Phi(x)$ with hypercharge $Y_\Phi = 1$:

$$\Phi(x) \;=\; \begin{pmatrix} \phi^+(x) \\ \phi^0(x) \end{pmatrix}. \tag{2.10}$$

To generate SSB the Higgs potential

$$V(\Phi) \;=\; -\mu^2 \left(\Phi^\dagger\Phi\right) + \frac{\lambda}{4}\left(\Phi^\dagger\Phi\right)^2, \qquad \mu^2, \lambda > 0, \tag{2.11}$$

of the gauge-invariant Lagrangian

$$\mathcal{L}_H \;=\; (D_\mu\Phi)^\dagger\,(D^\mu\Phi) - V(\Phi) \tag{2.12}$$

is constructed in such a way that it possesses a minimum at $\Phi_0^\dagger\Phi_0 = \frac{2\mu^2}{\lambda} = \frac{v^2}{2} > 0$. For perturbation theory one vacuum-expectation value has to be chosen to define the field excitations. A convenient choice is

$$\Phi_0 \;=\; \begin{pmatrix} 0 \\ \frac{v}{\sqrt{2}} \end{pmatrix}, \tag{2.13}$$

which is not $SU(2)_W \otimes U(1)_Y$ symmetric and fixes the gauge. All four generators of this group are broken, but the linear combination

$$Q \;=\; I_3 + \frac{Y}{2} \tag{2.14}$$

is not. Therefore only three bosons become massive while one remains massless which is the photon.

One can separate Φ from Φ_0,

$$\Phi(x) \;=\; \Phi_0 + \begin{pmatrix} \phi^+(x) \\ \frac{1}{\sqrt{2}}\left(\eta(x) + i\,\chi(x)\right) \end{pmatrix}, \tag{2.15}$$

where $\eta(x)$ and $\chi(x)$ are real fields with vanishing vacuum expectation values. As already mentioned above, the Goldstone bosons in gauge theories are not physical. Therefore they are also called *would-be Goldstone bosons*. Indeed the fields $\chi(x)$ and $\phi^+(x)$ can be transformed away by a gauge transformation. This special gauge is called *unitary gauge*.

Contrary to the unphysical fields $\phi^\pm(x)$ and $\chi(x)$, the field $\eta(x)$ corresponds to a physical particle, the *Higgs particle*. It has spin 0 and the mass

$$M_H \;=\; \sqrt{2}\,\mu. \tag{2.16}$$

The Higgs mass M_H is the last undetermined parameter of the SM. The experimentally allowed range for M_H is restricted by lower bounds from the direct search at LEP and indirect constraints from precision tests in the electroweak sector of the SM. The present lower bound from LEP is [24]

$$M_H \;>\; 114.1\,\mathrm{GeV} \tag{2.17}$$

at the 95% Confidence Level (CL).

Physical observables on the Z-resonance and of the muon decay as well as the top and the W mass have been measured very precisely. Hence they are sensitive to quantum corrections which depend on all parameters of the SM. Since the Higgs mass enters these quantum corrections only with logarithmical sensitivity the bounds on M_H coming from electroweak precision tests are not very stringent. The latest results yield [25, 26]

$$M_H \;<\; 212\,\mathrm{GeV} \tag{2.18}$$

at the 95% CL.

In addition to the lower and upper limits for the Higgs mass, a direct hint for a Higgs boson of 115.6 GeV has been found at LEP [24].

The vacuum expectation value v can be extracted from other quantities in various ways which differ in the treatment of higher-order corrections. A possibility appropriate for our purpose is the use of the Fermi constant G_F,

$$v^2 \;=\; \frac{1}{\sqrt{2}\,G_F}. \tag{2.19}$$

2.3 The Generation of Fermion Masses

The Higgs–Kibble mechanism can not only be used for creating masses for the gauge bosons but also for the generation of fermion masses. Denoting the charge conjugate of Φ by $\tilde{\Phi}$,

$$\tilde{\Phi} = i\,\sigma_2\,\Phi^* = \begin{pmatrix} \phi^{0*} \\ -\phi^- \end{pmatrix}, \tag{2.20}$$

the gauge-invariant Yukawa interaction $\mathcal{L}_{\mathrm{Yuk}}$ between fermionic and Higgs fields,

$$\mathcal{L}_{\mathrm{Yuk}} \;=\; -\sum_{l,e} \bar{\Psi}^l_L G_{le} \Psi^e_R \Phi - \sum_{q,d} \bar{\Psi}^q_L G_{qd} \Psi^d_R \Phi - \sum_{q,u} \bar{\Psi}^q_L \tilde{G}_{qu} \Psi^u_R \tilde{\Phi} + \mathrm{h.c.}, \tag{2.21}$$

yields the mass terms for the fermions after SSB

$$\mathcal{L}_{\mathrm{ferm-mass}} \;=\; -\sum_{l,e} \bar{\psi}^l_{e_L} G_{le} \psi^e_R \frac{v}{\sqrt{2}} - \sum_{q,d} \bar{\psi}^q_{d_L} G_{qd} \psi^d_R \frac{v}{\sqrt{2}} - \sum_{q,u} \bar{\psi}^q_{u_L} \tilde{G}_{qu} \psi^u_R \frac{v}{\sqrt{2}} + \mathrm{h.c.}, \tag{2.22}$$

where the components of the weak-isospin doublets $\left(\Psi_L^l\right)^T = \left((\psi_{\nu_L}^l)^T, (\psi_{e_L}^l)^T\right)$, $(\Psi_L^q)^T = \left((\psi_{u_L}^q)^T, (\psi_{d_L}^q)^T\right)$ and the weak-isospin singlets $\Psi_R = \psi_R$ have been used. The Yukawa couplings G_{le}, G_{qd}, and $\tilde{G}_{qu}$ are 3×3 matrices in flavour space. To obtain the mass eigenvalues one has to diagonalize these matrices by biunitary transformations:

$$\begin{aligned} \mathrm{diag}(m_e) &= \frac{v}{\sqrt{2}}\, U_L^l\, G_{le}\, U_R^{e\dagger}, \\ \mathrm{diag}(m_u) &= \frac{v}{\sqrt{2}}\, \tilde{U}_L^q\, \tilde{G}_{qu}\, \tilde{U}_R^{u\dagger}, \\ \mathrm{diag}(m_d) &= \frac{v}{\sqrt{2}}\, U_L^q\, G_{qd}\, U_R^{d\dagger}. \end{aligned} \tag{2.23}$$

The simultaneous transformations of the fields,

$$\begin{array}{lll} \psi_{e_L}^l \to U_L^l\, \psi_{e_L}^l, & \psi_{d_L}^q \to U_L^q\, \psi_{d_L}^q, & \psi_{u_L}^q \to \tilde{U}_L^q\, \psi_{u_L}^q, \\ \psi_R^e \to U_R^e\, \psi_R^e, & \psi_R^d \to U_R^d\, \psi_R^d, & \psi_R^u \to \tilde{U}_R^u\, \psi_R^u, \end{array} \tag{2.24}$$

in $\mathcal{L}_{\mathrm{fermion}} + \mathcal{L}_{\mathrm{Yuk}}$ drop out for couplings that conserve weak isospin but remain as

$$V^{q/l} = \tilde{U}_L^{q/l} U_L^{q/l\dagger} \tag{2.25}$$

in the interactions involving the charged fields $W^\pm$ and $\phi^\pm$. In the approximation of vanishing neutrino masses, the mass degeneracy allows to choose the transformation of the neutrino fields as $\tilde{U}_L^l = U_L^l$. Therefore V^l becomes the unit matrix. For the quark sector this matrix $V^{\mathrm{CKM}} \equiv V^q$ remains and is known as the Cabibbo-Kobayashi-Maskawa (CKM) matrix [74–76].

Eq. (2.23) shows the relation between the fermion masses, the vacuum expectation value and the $q\bar{q}H$ Yukawa coupling which in case of one quark reads

$$g_{q\bar{q}H} = \frac{\sqrt{2}}{v}\, m_q. \tag{2.26}$$

This is an essential prediction of the generation of the fermion masses via the Higgs–Kibble mechanism. Measuring these three parameters independently allows to test this prediction and therewith the Higgs sector of the SM.

2.4 Next-to-Leading Order Corrections

Since it is impossible to obtain a closed analytical solution of the fundamental equations describing a chosen process within the SM the most important tool used for calculating physical observables is perturbation theory. Transition amplitudes are expanded in power series of small dimensionless parameters which usually are the gauge couplings of the theory.

The Leading Order (LO) is the lowest order with non-vanishing coefficient, the Next-to-Leading Order (NLO) the next higher order. Furthermore for the diagrammatic approach the number of loops in a diagram is important. The case of no loops is called Born or tree level. In this work the virtual NLO corrections are provided by one-loop corrections and therefore the two expressions "virtual NLO" and "one-loop" are interchangeable. Please note that this is only the case if LO and tree-level coincide.

One-loop virtual diagrams lead to integrals of the form

$$\int \frac{d^4k}{(2\pi)^4} \frac{1, k_\mu, k_\mu k_\nu, \dots}{[k^2 - m_0^2]\,[(k+k_1)^2 - m_1^2]\,[(k+k_2)^2 - m_2^2]\,\dots}\,, \tag{2.27}$$

where k is the loop momentum, which is not fixed by the external momenta, and the k_i are linear combinations of the external momenta. The denominator is built up by propagators with momenta $k + k_i$ and masses m_i, and the numerator by couplings and factors stemming from fermion propagators. Since these integrals are, in general, divergent one has to regularize them which is most conveniently done by Dimensional Regularization (DR) [77, 78] because it is technically simple and it preserves all symmetries of the SM:

$$\int \frac{d^4k}{(2\pi)^4} \to \mu_{DR}^{4-D} \int \frac{d^Dk}{(2\pi)^D}. \tag{2.28}$$

The new mass μ_{DR} is introduced to keep the action dimensionless. For $D = 4 - 2\varepsilon$ the divergences occur as $\frac{1}{\varepsilon}$ and $\frac{1}{\varepsilon^2}$ poles in NLO.

There are two kinds of divergences which can be separated in a unique way, one at infinite loop momentum k and the other one at finite values of k. The former are called UltraViolet (UV) divergences. They produce only $\frac{1}{\varepsilon}$ poles and are removed by renormalization (see Section 2.5). The latter are InfraRed (IR) divergences and can only appear if massless particles are involved. In our notation they are subclassified into soft and collinear divergences. The former occur at specific values of k and the latter from regions where the loop momentum k becomes collinear with an external light-like momentum p ($k \cdot p \to 0$). Only the overlap of soft and collinear divergences leads to $\frac{1}{\varepsilon^2}$ poles. Since the UV divergences can clearly be distinguished from the IR ones, they can be regularized independently which leads to the possibility of introducing two independent masses μ_{UV} and μ_{IR} in Eq. (2.28) for UV and IR divergences, respectively.

Quantities that do not depend on the long-distance behaviour of the theory are *infrared safe* [79–82]. They do not contain any soft or collinear divergences. Inclusive cross sections belong to the class of infrared-safe quantities. For an inclusive cross section one has to sum over all indistinguishable initial as well as final states.

In the case of a hadron–hadron scattering into the final state $a + b + X$,

$$A + B \;\to\; a + b + X, \tag{2.29}$$

the process

$$A + B \;\to\; a + b + g + X \tag{2.30}$$

is physically indistinguishable from the process (2.29) if the gluon is soft or collinear to another parton. In addition, it is of the same order in perturbation theory as the virtual corrections to (2.29). Therefore this process has to be included when calculating the NLO corrections to (2.29). Corrections like (2.30) are called *real corrections*. In this work the two processes (2.29) and (2.30) are not distinguished at all and the real corrections include the whole gluon spectrum instead of only the soft and collinear parts.

Due to the vanishing gluon mass real corrections contain soft and possibly collinear divergences, which cancel the soft and partly the collinear divergences of the virtual corrections. The remaining collinear divergences are removed by the renormalization of the parton densities. This procedure is called *factorization* and will be explained in Section 2.7.

In summary, the NLO corrections $\Delta\sigma^{\text{NLO}}$ to the total cross section σ contain three parts: the virtual corrections, the real corrections, and the collinear counter term,

$$\Delta\sigma^{\text{NLO}} = \sigma^{\text{virtual}} + \sigma^{\text{real}} + \sigma^{\text{coll}}. \tag{2.31}$$

2.5 Renormalization

As already mentioned in the previous section, calculating higher-order corrections leads to UV divergences which are regularized, e.g., by DR. The idea of *renormalization* is to calculate physical quantities with *bare* parameters that are divergent. These bare parameters are then renormalized leading to a finite result for all physical quantities. This remarkable feature is called *renormalizability* and was first proven by 't Hooft [83, 84] for non-Abelian gauge theories with SSB.

The bare parameters and fields are expressed in terms of *renormalized* parameters and fields by means of a renormalization transformation:

$$\begin{aligned}
\text{gluon field renormalization:} \quad & G_\mu^0 = \sqrt{Z_G}\, G_\mu = \left(1 + \frac{1}{2}\,\delta Z_G\right) G_\mu, \\
\text{quark field renormalization:} \quad & \psi_Q^0 = \sqrt{Z_Q}\, \psi_Q = \left(1 + \frac{1}{2}\,\delta Z_Q\right) \psi_Q, \\
\text{mass renormalization:} \quad & m_Q^0 = m_Q + \delta m_Q, \\
\text{coupling renormalization:} \quad & g_s^0 = g_s + \delta g_s.
\end{aligned} \tag{2.32}$$

The bare quantities are labeled by a superscript 0. The quantities with a δ are called *renormalization constants* and contain the UV divergences. The divergences are unique but there is a freedom in choosing the finite part shifted into the renormalization constants. This choice defines the *renormalization scheme*. The actual numerical prediction for a physical quantity is independent of the renormalization scheme used for the calculation.

The most common renormalization schemes are the *on-shell scheme* [85–89] mostly used in calculating electroweak corrections and the *modified Minimal Subtraction ($\overline{MS}$) scheme*

[90] which is the preferred one for calculating QCD corrections. In this work the on-shell scheme is used for massive quarks and the $\overline{MS}$ scheme for all massless particles.

- In the on-shell scheme the renormalized masses are chosen as the poles of the propagators. In addition the renormalization constants of the fields are adjusted such that all external self-energies vanish. This leads to two conditions on the renormalized one-particle-irreducible two-point function $\hat{\Gamma}_Q(p)$ of a massive quark:

$$\lim_{p^2\to m_Q^2} \hat{\Gamma}_Q(p)\,\psi_Q(p) = 0, \tag{2.33}$$

$$\lim_{p^2\to m_Q^2} \frac{\not{p}+m_Q}{p^2-m_Q^2}\hat{\Gamma}_Q(p)\,\psi_Q(p) = i\,\psi_Q(p). \tag{2.34}$$

  In NLO $\hat{\Gamma}_Q(p)$ contains the tree-level two-point function, the one-loop self-energy, and the counter terms,

$$\hat{\Gamma}_Q(p) = i[\not{p}-m_Q] + i\left[\not{p}\Sigma_Q^P(p^2) + m_Q\Sigma_Q^S(p^2)\right] + i\left[(\not{p}-m_Q)\delta Z_Q + \delta m_Q\right]. \tag{2.35}$$

  The two on-shell conditions Eq. (2.33) and (2.34) can be rewritten as:

$$\delta m_Q = m_Q\Big[\Sigma_Q^P(m_Q^2) + \Sigma_Q^S(m_Q^2)\Big], \tag{2.36}$$

$$\delta Z_Q = -\Sigma_Q^P(m_Q^2) - 2\,m_Q^2\frac{\partial}{\partial p^2}\,\Big[\Sigma_Q^P(p^2) + \Sigma_Q^S(p^2)\Big]\Big|_{p^2=m_Q^2}. \tag{2.37}$$

- In the *Minimal Subtraction (MS) scheme* [91] the renormalization constants only contain divergences but no finite terms. As in the case of a massive quark, the two-point functions of a massless quark and a gluon contain three contributions at the one-loop level:

$$\hat{\Gamma}_q(p) = i\not{p} + i\not{p}\,\Sigma_q^P(p^2) + i\not{p}\,\delta Z_q, \tag{2.38}$$

$$\hat{\Gamma}^{ab}_{\mu\nu}(k) = -ig_{\mu\nu}\,\delta^{ab}k^2 - i\left(g_{\mu\nu} - \frac{k_\mu k_\nu}{k^2}\right)\delta^{ab}k^2\,\Pi_T(k^2) - i\left(g_{\mu\nu} - \frac{k_\mu k_\nu}{k^2}\right)\delta^{ab}k^2\,\delta Z_G, \tag{2.39}$$

  where $\Pi_T(k^2)$ denotes the vacuum polarization. The condition of the finiteness of the renormalized two-point functions leads to the renormalization conditions of the MS scheme:

$$\delta Z_q = -\,\Sigma_q^P(p^2)\big|_{\rm div}\,, \tag{2.40}$$

$$\delta Z_G = -\,\Pi_T(k^2)\big|_{\rm div}\,. \tag{2.41}$$

The renormalization constant of the QCD coupling is determined by the condition of the finiteness of the corrections to the $q\bar{q}g$ vertex $\Gamma^a_{ji,\mu}$,

$$(-i\,g_s)T^a_{ji}\gamma_\mu\left(\frac{\delta g_s}{g_s}+\frac{1}{2}\,\delta Z_G+\delta Z_Q\right) \;=\; -\,\Gamma^a_{ji,\mu}\big|_{\rm div}\,, \tag{2.42}$$

where a, i, j are the colour indices of the gluon and the two quarks. The renormalization constants δZ_q, δZ_G, and δg_s defined above do not depend on the scale μ_{UV}. Hence this *ad hoc* introduced parameter does not drop out in the renormalized quantities. The dependence on μ_{UV} is absorbed by the introduction of a scale dependent coupling $\alpha_s(\mu_{UV})$. By comparison with other renormalization schemes one can interpret μ_{UV} as the renormalization scale which is usually denoted by μ_R. The dependence of the strong coupling on μ_R is described by the renormalization group equation [91–93]. The $\overline{MS}$ scheme differs from the MS scheme by absorbing some general finite terms in the renormalization constants. It makes use of the fact that UV poles always occur in the combination

$$\Delta_{UV}=\frac{\Gamma(1+\varepsilon)}{\varepsilon}\,(4\pi)^\varepsilon=\frac{1}{\varepsilon}-\gamma_E+\log(4\pi) \tag{2.43}$$

with the Euler constant $\gamma_E = 0.5772156649\ldots$ and the Gamma function $\Gamma(x)$.

In this work the $\overline{MS}$ scheme for the QCD coupling g_s is altered in such a way that the heavy quarks are decoupled from the running of α_s. For the explicit form of the renormalization constants see Chapter 4.

Note that the vacuum expectation value as well as the Higgs field and mass are not renormalized in this work because at the one-loop level neither of them receives QCD corrections. Electroweak corrections would affect all these parameters and fields, however, they are ignored here.

When calculating S-matrix elements one has to take the Lehmann–Symanzik–Zimmermann (LSZ) factors $\mathcal{Z} = 1+\delta\mathcal{Z}$ [94] for all external fields into account. The term $\delta\mathcal{Z}$ is connected to the renormalized one-loop self-energy of the corresponding particle. The second condition of the on-shell scheme, Eq. (2.34), is chosen in such a way that the LSZ factor is equal to one. When using the $\overline{MS}$ scheme these LSZ factors differ from unity, see Appendix B.

When summing all orders of perturbation theory, the result for a physical quantity is independent of the artificially introduced renormalization scale. In practice one has to truncate the series at a certain order n which leads to a dependence on the renormalization scale of order $n+1$. The remaining renormalization-scale dependence quantifies part of the theoretical uncertainty caused by unknown higher-order corrections.

2.6 The Parton Model

The parton model of hadrons is based on the following assumptions: (i) hadrons are made up of constituents, their *partons*, which are identified with the quarks and gluons of QCD, (ii) every parton carries a longitudinal momentum which is a fraction ξ of the hadron's momentum p^μ with $0 \leq \xi \leq 1$ and only a negligible transverse momentum, (iii) for the hard scattering of the partons all hadron and parton masses can be neglected, and (iv) the typical time of the hard scattering process is much smaller than the interaction time of the partons with each other. Therefore the partons can be treated as quasi-free particles which scatter incoherently.

The parton model allows to separate the hard (short-distance) from the soft (long-distance) interactions. In this way it is possible to calculate the former in perturbative QCD (pQCD) and to convolve the partonic cross section $\hat{\sigma}$ with the probability density $f_{i,A}(\xi)$ to find a parton i in hadron A with momentum ξp^μ. These probability densities are called *parton densities*. In case of hadron–hadron scattering the convolution reads

$$\sigma_{AB}(p_1, p_2) = \sum_{i,j} \int_0^1 dx_1\, dx_2\, \hat{\sigma}_{ij}(x_1 p_1, x_2 p_2)\, f_{i,A}(x_1)\, f_{j,B}(x_2). \tag{2.44}$$

Here the sum extends over all initial partons i, j which lead to the chosen final state. The parton densities contain all the soft properties of the model which are not accessible by perturbation theory. Since they cannot be calculated they have to be determined from experiment, e.g., from deep inelastic scattering in ep collisions at HERA [95, 96].

2.7 Factorization

In Section 2.4 the term σ^{coll} was introduced to cancel the remaining collinear divergences after adding virtual and real corrections in Eq. (2.31). The *factorization theorem* [97] states that these remaining divergences are process-independent and can be absorbed by a redefinition of the parton density functions. In analogy to renormalization, physical quantities are calculated using collinear divergent bare parton densities. The parton densities are then renormalized. This leads to the cancellation of the process-independent collinear divergences and hence to a finite result. The renormalized parton densities in terms of the bare ones read:

$$f_q(x, \mu_F^2) = f_q^0(x) + \frac{\alpha_s}{2\pi}(f_q^0 \otimes F^{qq})(x, \mu_F^2) + \frac{\alpha_s}{2\pi}(f_g^0 \otimes F^{qg})(x, \mu_F^2), \tag{2.45}$$

$$f_g(x, \mu_F^2) = f_g^0(x) + \frac{\alpha_s}{2\pi}(f_q^0 \otimes F^{gq})(x, \mu_F^2) + \frac{\alpha_s}{2\pi}(f_g^0 \otimes F^{gg})(x, \mu_F^2). \tag{2.46}$$

The convolution is defined as

$$(f \otimes g)(x, \mu^2) = \int_x^1 \frac{d\xi}{\xi} f(\xi, \mu^2)\, g\left(\frac{x}{\xi}, \mu^2\right), \tag{2.47}$$

and the $F^{ab}(x,\mu_F^2)$ read

$$F^{ab}(x,\mu_F^2) = -\frac{\Gamma(1+\varepsilon)}{\varepsilon}\left(\frac{4\pi\mu_F^2}{\mu_{IR}^2}\right)^{\varepsilon} P^{ab}(x) + C^{ab}(x). \tag{2.48}$$

A new scale μ_F is introduced, the *factorization scale*. It distinguishes the soft from the hard region. While the first term in Eq. (2.48) containing all divergences is unique the finite term C^{ab} involves some freedom. This choice defines the *factorization scheme*. In the $\overline{MS}$ scheme [98] they are zero by definition while in the DIS scheme [99] they are adjusted in such a way that the structure function F_2 of the proton remains unchanged after factorization.

The *Altarelli–Parisi splitting functions* $P^{ab}(x)$ describe the probability for the emission of a parton a with momentum fraction x from a parton b [100]:

$$P^{qq}(x) = C_F\left[\frac{1+x^2}{(1-x)_+} + \frac{3}{2}\delta(1-x)\right] = C_F\left[\frac{1+x^2}{1-x}\right]_+, \tag{2.49}$$

$$P^{qg}(x) = T_R\left[x^2+(1-x)^2\right], \tag{2.50}$$

$$P^{gq}(x) = C_F\left[\frac{1+(1-x)^2}{x}\right], \tag{2.51}$$

$$P^{gg}(x) = 2C_A\left[\frac{x}{(1-x)_+} + \frac{1-x}{x} + x(1-x)\right] + \frac{11C_A - 4T_R N_f}{6}\delta(1-x), \tag{2.52}$$

where $C_A = 2\,T_R N_C = 3$ and $C_F = T_R\frac{N_C^2-1}{N_C} = \frac{4}{3}$ are the Casimir operators of the $SU(3)_C$ group with the number of colours $N_C = 3$ and the customary normalization $T_R = \frac{1}{2}$. N_f denotes the number of light quarks. The "+" distribution is defined in the usual way:

$$\int_0^1 dx\,[f(x)]_+\,g(x) = \int_0^1 dx\,f(x)\,[g(x)-g(1)]\,. \tag{2.53}$$

The splitting functions can be written in terms of regularized splitting functions plus an infrared sensitive part:

$$P^{ab}(x) = P^{ab}_{\rm reg}(x) + \delta^{ab}\left[2\,\mathbf{T}_a^2\left(\frac{1}{1-x}\right)_+ + \gamma_a\delta(1-x)\right], \tag{2.54}$$

where the square of the colour operators $\mathbf{T}_a$ are the Casimir operators $\mathbf{T}_g^2 = C_A$ and $\mathbf{T}_q^2 = C_F$, and $\gamma_g = \frac{11C_A-4T_RN_f}{6}$ and $\gamma_q = \frac{3}{2}C_F$ are the anomalous dimensions.

The convolution in Eq. (2.44) has now to be expressed in terms of renormalized parton

densities. The NLO corrections to the hadronic cross section then reads:

$$\begin{aligned}\Delta\sigma_{AB}^{\mathrm{NLO}}(p_1,p_2) &= \sum_{i,j}\int_0^1 dx_1\,dx_2\,\Delta\hat{\sigma}_{ij}^{\mathrm{NLO}}(x_1p_1,x_2p_2)\,f_{i,A}(x_1)\,f_{j,B}(x_2)\\ &- \sum_{i,j}\int_0^1 dx_1\,dx_2\,\hat{\sigma}_{ij}^{\mathrm{LO}}(x_1p_1,x_2p_2)\left(\frac{\alpha_s}{2\pi}\sum_k(f_{k,A}\otimes F^{ik})(x_1,\mu_F^2)\right)f_{j,B}(x_2)\\ &- \sum_{i,j}\int_0^1 dx_1\,dx_2\,\hat{\sigma}_{ij}^{\mathrm{LO}}(x_1p_1,x_2p_2)\;f_{i,A}(x_1)\left(\frac{\alpha_s}{2\pi}\sum_l(f_{l,B}\otimes F^{jl})(x_2,\mu_F^2)\right).\end{aligned} \tag{2.55}$$

The quantity $\Delta\hat{\sigma}_{ij}^{\mathrm{NLO}}$ contains the virtual and the real corrections to the partonic cross section. Hence this first term is equal to the sum $\sigma^{\mathrm{virtual}}+\sigma^{\mathrm{real}}$ in Eq. (2.31). The remaining two terms in Eq. (2.55) provide the expression for the collinear counter-term σ^{coll}.

The statements about the renormalization scale at the end of Section 2.5 also hold for the factorization scale μ_F. When summing all orders of perturbation theory any physical quantity is independent of μ_F but when truncating this series a dependence on it remains and is part of the theoretical uncertainty.

Chapter 3

Conventions and LO Cross Section

3.1 Notations and Conventions

In LO two partonic processes contribute to the hadronic processes $PP/P\bar{P} \to Q\bar{Q}H$:

$$\begin{aligned} q(p_1) + \bar{q}(p_2) &\to Q(p_3) + \bar{Q}(p_4) + H(p_5), \\ g(p_1) + g(p_2) &\to Q(p_3) + \bar{Q}(p_4) + H(p_5). \end{aligned}$$

Typical diagrams of these processes are depicted in Fig. 3.1. The $p_a^\mu = (p_a^0, \mathbf{p}_a), (a = 1, \ldots, 5)$ denote the momenta of the massless incoming and of the massive outgoing particles with masses $m_i = \sqrt{p_i^2}$. The following invariants are defined:

$$\hat{s} = (p_1 + p_2)^2, \qquad s_{ij} = (p_i + p_j)^2, \qquad t_{ai} = (p_a - p_i)^2, \tag{3.1}$$

with $a = 1, 2$ and $i, j = 3, 4, 5$. Only six of the ten variables above are independent since one momentum can be eliminated by momentum conservation. The squared partonic Centre-of-Mass (CM) energy $\hat{s}$ is related to the hadronic CM energy squared s by $\hat{s} = x_1 x_2 s$ where x_1 and x_2 are the momentum fractions of the incoming partons.

The partonic cross section $\hat{\sigma}_{ab}$ for the partonic process $a + b \to \ldots$ is given by

$$\hat{\sigma}_{ab} = \frac{1}{2\hat{s}} \int d\mathrm{PS} \frac{1}{N_c(c_a) N_s(s_a) N_c(c_b) N_s(s_b)} \sum_{\text{colour}} \sum_{\text{spin}} |\mathcal{M}|^2 , \tag{3.2}$$

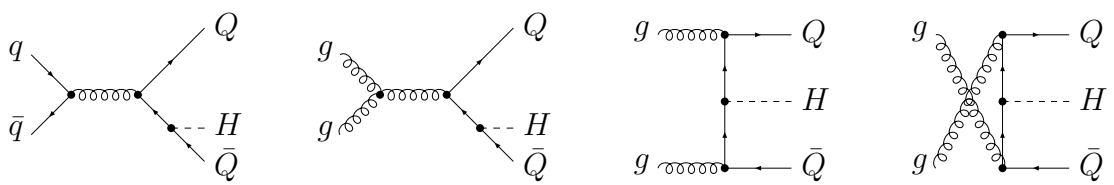

Figure 3.1: Typical LO diagrams.

where $N_c(c_a)$ and $N_s(s_a)$ denote the number of the colour and spin degrees of freedom of the incoming particles, respectively. The colour and spin quantum numbers are labeled by c_a and s_a, respectively. The integral over the 3-particle Phase Space (PS) in four dimensions is given by

$$\begin{aligned}\int d\mathrm{PS} &= \int \left(\prod_{i=3}^{5} \frac{d^3\mathbf{p}_i}{(2\pi)^3\, 2p_i^0}\right) (2\pi)^4 \delta^4(p_1+p_2-p_3-p_4-p_5) \\ &= \frac{1}{8(2\pi)^5} \int d\Omega_3\, d\beta\, dp_3^0\, dp_4^0. \end{aligned} \tag{3.3}$$

The variables in the second line of Eq. (3.3) are defined in the partonic Centre-of-Mass System (CMS) with the beam pipe along the z axis,

$$p_1^\mu = (E,0,0,E), \qquad p_2^\mu = (E,0,0,-E). \tag{3.4}$$

The solid angle of the outgoing quark is denoted by $d\Omega_3 = d\cos(\theta_3)\, d\phi_3$. In addition, α and β are the polar and azimuthal angles of $\mathbf{p}_4$ relative to $\mathbf{p}_3$, respectively. The angle α is determined by

$$\cos(\alpha) = \frac{\mathbf{p}_3 \cdot \mathbf{p}_4}{|\mathbf{p}_3||\mathbf{p}_4|} = \frac{|\mathbf{p}_5|^2 - |\mathbf{p}_3|^2 - |\mathbf{p}_4|^2}{2|\mathbf{p}_3||\mathbf{p}_4|}, \tag{3.5}$$

where momentum conservation, $\mathbf{p}_3 + \mathbf{p}_4 + \mathbf{p}_5 = 0$, was used. The integration limits for the angles are

$$0 \le \theta_3 \le \pi, \qquad 0 \le \phi_3 \le 2\pi, \qquad 0 \le \beta \le 2\pi. \tag{3.6}$$

Due to rotational invariance around the beam axis the integration over ϕ_3 can be performed in a trivial way yielding a factor 2π.

The condition $|\cos(\alpha)| \le 1$ leads to the boundaries for p_3^0 and p_4^0 which are not independent. Employing energy conservation, $2E = p_3^0 + p_4^0 + p_5^0$, Eq. (3.5) yields

$$(p_4^0)_{\mathrm{max,min}} = \frac{(2E-p_3^0)(A_3+m_4^2-m_5^2) \pm \sqrt{(p_3^0)^2-m_3^2}\,\kappa(A_3,m_4^2,m_5^2)}{2A_3} \tag{3.7}$$

with the abbreviation

$$A_3 = 4E(E-p_3^0) + m_3^2 \tag{3.8}$$

and the Källén function

$$\begin{aligned}\kappa^2(x,y,z) &= x^2+y^2+z^2-2(xy+yz+zx) \\ &= (\sqrt{x}+\sqrt{y}+\sqrt{z})(\sqrt{x}-\sqrt{y}+\sqrt{z})(\sqrt{x}+\sqrt{y}-\sqrt{z})(\sqrt{x}-\sqrt{y}-\sqrt{z}). \end{aligned} \tag{3.9}$$

The limits for p_3^0 are reached when the integration interval for p_4^0 vanishes:

$$(p_3^0)_{\min} = m_3, \qquad (p_3^0)_{\max} = \frac{4E^2+m_3^2-(m_4+m_5)^2}{4E}. \tag{3.10}$$

To obtain the hadronic cross section, the partonic cross section, Eq. (3.2), has to be convolved with the parton densities as described in Eq. (2.44).

3.2 Standard Matrix Elements

The amplitude $\mathcal{M}$ depends on the invariants defined in Eq. (3.1), the colour indices c_a and c_i of the incoming and outgoing QCD particles, respectively, and the spin s_a and s_j of the initial- and final-state particles:

$$\mathcal{M} \;=\; \mathcal{M}(\hat{s}, s_{ij}, t_{ai}; c_a, c_j; s_a, s_j). \tag{3.11}$$

It can be decomposed into Lorentz invariant formfactors $F_{c,i}(\hat{s}, s_{ij}, t_{ai})$, colour structures $\mathcal{C}_c(c_a, c_j)$, and Standard Matrix Elements (SME) $\mathcal{M}_i$ incorporating the dependence on the spin and the polarization vectors:

$$\mathcal{M}(\hat{s}, s_{ij}, t_{ai}; c_a, c_j; s_a, s_j) \;=\; \sum_{c,i} \mathcal{M}_i(\hat{s}, s_{ij}, t_{ai}; s_a, s_j)\, \mathcal{C}_c(c_a, c_j)\, F_{i,c}(\hat{s}, s_{ij}, t_{ai}). \tag{3.12}$$

The square of the amplitude can then be calculated as

$$|\mathcal{M}|^2 \;=\; \sum_{c',c} \sum_{i',i} \left(\mathcal{M}_{i'}^{\dagger}\, \mathcal{M}_i\right) \left(\mathcal{C}_{c'}^{\dagger}\, \mathcal{C}_c\right) \left(F_{i',c'}^{*} F_{i,c}\right). \tag{3.13}$$

The advantages of this decomposition are manifold. The time-consuming calculation of the traces of Dirac matrices occurring from squaring the amplitude has only to be done once when computing $\mathcal{M}_i^{\dagger}\mathcal{M}_j$. The effort of computing the formfactors is smaller than contracting the amplitudes, both analytically and numerically. Especially when calculating virtual corrections this method reduces the analytical result and therefore the time for numerical evaluation tremendously since the contraction of the virtual amplitudes with the complete LO amplitude is avoided. In addition it simplifies by choosing different gauges for internal and external gluons. Owing to the avoidance of external ghosts a polarization sum which projects out the physical states is used for external gluons. The Feynman gauge is applied to the internal gluons leading to the simplest possible gluon propagator.

For the $q\bar{q}$ channel at LO solely one colour structure,

$$\mathcal{C}_1^{q\bar{q}} = i\, t^a_{c_4 c_3} t^a_{c_2 c_1}, \qquad |\mathcal{C}_1^{q\bar{q}}|^2 = 2, \tag{3.14}$$

and only four SME,

$$\begin{aligned}
\mathcal{M}_{1,1}^{q\bar{q}} &= [\bar{v}(p_2)\not{k}_1 u(p_1)]\,[\bar{u}(p_3)v(p_4)],\\
\mathcal{M}_{5,1}^{q\bar{q}} &= [\bar{v}(p_2)\not{k}_2 u(p_1)]\,[\bar{u}(p_3)v(p_4)],\\
\mathcal{M}_{10,1}^{q\bar{q}} &= [\bar{v}(p_2)\gamma^{\mu} u(p_1)]\,[\bar{u}(p_3)\gamma_{\mu}\not{p}_1 v(p_4)],\\
\mathcal{M}_{11,1}^{q\bar{q}} &= [\bar{v}(p_2)\gamma^{\mu} u(p_1)]\,[\bar{u}(p_3)\gamma_{\mu}\not{p}_2 v(p_4)],
\end{aligned} \tag{3.15}$$

are sufficient. The corresponding formfactors are

$$F_{1,1}^{q\bar{q}} = +\frac{2}{\hat{s}(s_{45}-m_Q^2)}, \qquad F_{5,1}^{q\bar{q}} = -\frac{2}{\hat{s}(s_{35}-m_Q^2)}, \qquad F_{10,1}^{q\bar{q}} = F_{11,1}^{q\bar{q}} = \frac{1}{2}\left(F_{5,1}^{q\bar{q}} - F_{1,1}^{q\bar{q}}\right). \tag{3.16}$$

For the gg channel the situation is much more involved. The polarization vector of the incoming gluon with momentum p_i^μ is denoted by ϵ_i^μ. In addition to the transversality condition $\epsilon_i \cdot p_i = 0$ they are requested to fulfill the gauge conditions

$$\epsilon_1 \cdot p_2 = \epsilon_2 \cdot p_1 = 0. \tag{3.17}$$

In our choice, twelve SME are needed for the gg channel at LO. They are listed in Appendix A together with the corresponding formfactors. The first three of the following colour structures are the ones of the t-, u-, and the s-channel, respectively, while the last one only contributes in NLO,

$$\begin{aligned} \mathcal{C}_1^{gg} &= i\, t^{c_1}_{c_4 c}\, t^{c_2}_{c c_3}, \\ \mathcal{C}_2^{gg} &= i\, t^{c_2}_{c_4 c}\, t^{c_1}_{c c_3}, \\ \mathcal{C}_3^{gg} &= f^{c_1 c_2 c}\, t^{c}_{c_4 c_3}, \\ \mathcal{C}_4^{gg} &= i\, d^{c_1 c_2 c}\, t^{c}_{c_4 c_3}. \end{aligned} \tag{3.18}$$

These four colour structures are not independent, e.g. $\mathcal{C}_3^{gg}$ can easily be expressed in terms of $\mathcal{C}_1^{gg}$ and $\mathcal{C}_2^{gg}$ by using the commutation relation of $t^c_{c_4 c_3}$. For calculating the square of the amplitude, the 4×4 matrix $(\mathcal{C}_i^{gg})^\dagger \mathcal{C}_j^{gg}$ has to be computed,

$$(\mathcal{C}_i^{gg})^\dagger \mathcal{C}_j^{gg} = \begin{pmatrix} \frac{16}{3} & -\frac{2}{3} & -6 & \frac{10}{3} \\ -\frac{2}{3} & \frac{16}{3} & 6 & \frac{10}{3} \\ -6 & 6 & 12 & 0 \\ \frac{10}{3} & \frac{10}{3} & 0 & \frac{20}{3} \end{pmatrix}. \tag{3.19}$$

3.3 The Input Parameters

For the numerical evaluation the Yukawa coupling $g_{Q\bar{Q}H} = \sqrt{2}\, m_Q / v$ is needed. In this work the vacuum expectation value v is extracted from the Fermi constant G_F via the tree-level relation Eq. (2.19), $v^2 = 1/(\sqrt{2}\, G_F)$. The numerical values of G_F and the top-quark mass m_t are given by $G_F = 1.16639 \times 10^{-5}\,\mathrm{GeV}^{-2}$ [101] and $m_t = 174\,\mathrm{GeV}$.

The Higgs mass will be varied between 80 and 280 GeV with a preferred value of 120 GeV.

Since the QCD parameter Λ_{QCD} is simultaneously fitted together with the parton densities, it is fixed by the choice of the latter. In this work CTEQ4 [102] is used for the parton densities. The parameters $\Lambda_5^{\mathrm{LO}} = 0.181\,\mathrm{GeV}$ and $\Lambda_5^{\overline{MS}} = 0.202\,\mathrm{GeV}$ are the corresponding values of Λ_{QCD} for the CTEQ4L and CTEQ4M parton densities at LO and at NLO using the $\overline{MS}$ scheme, respectively. The subscript 5 indicates that the number of light flavours is set to five.

The default value for the renormalization and the factorization scales is defined as half the threshold energy,

$$\mu_0 \quad = \quad (2m_t + M_H)/2. \tag{3.20}$$

To examine the scale dependence μ_R and μ_F will be varied from $\mu_0/5$ to $5\mu_0$.

3.4 The LO Predictions for $P\bar{P}/PP \to t\bar{t}H$

Figure 3.2 shows the LO approximation of the total cross section at the TEVATRON and the LHC for $P\bar{P}/PP \to t\bar{t}H+X$ as a function of the Higgs mass. Both the renormalization and the factorization scales are set to the central value, $\mu_R = \mu_F = \mu_0$. The cross section at the TEVATRON is multiplied by a factor 100 in order to be visible. It drops from 10 fb for $M_H = 100$ GeV to 0.3 fb for $M_H = 250$ GeV. At the LHC the cross section varies between 940 fb and 70 fb in the same Higgs mass range.

In Fig. 3.3 the scale dependence of the total cross section for a fixed value of $M_H = 120$GeV is plotted. Again the renormalization and the factorization scales are chosen to be equal, $\mu = \mu_R = \mu_F$, and the cross section at the TEVATRON is multiplied by 100. The dramatic variation of more than a factor of three at the TEVATRON and roughly a factor 2.5 at the LHC within the rather small interval $\mu_0/3 < \mu < 3\,\mu_0$ shows that the LO approximation

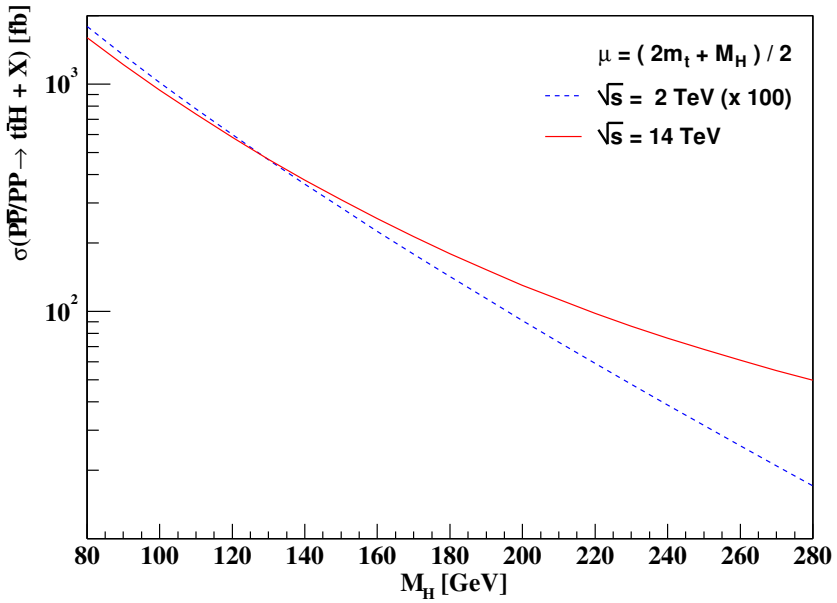

Figure 3.2: The total cross section for $P\bar{P}/PP \to t\bar{t}H + X$ in LO at the TEVATRON (dashed line) and the LHC (solid line).

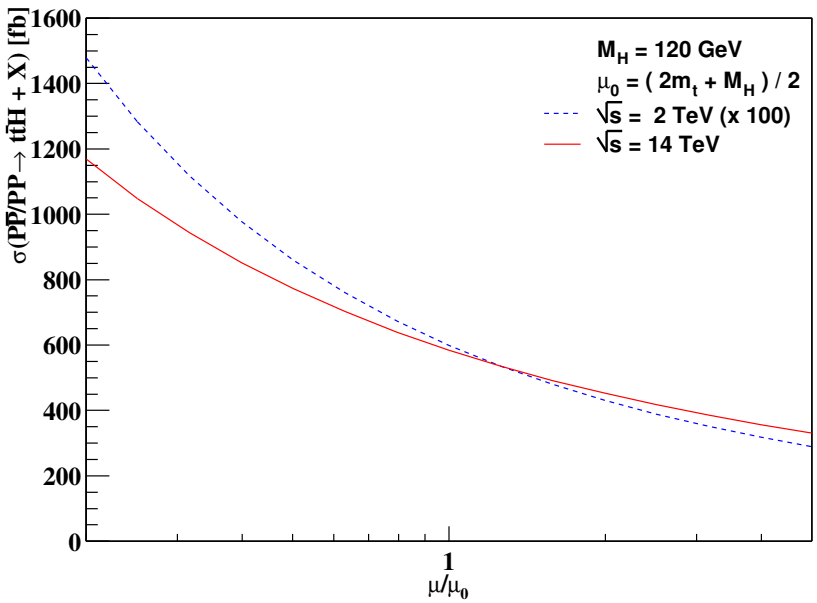

Figure 3.3: The scale dependence of the total cross section for $P\bar{P}/PP \to t\bar{t}H + X$ in LO at the TEVATRON (dashed line) and the LHC (solid line).

for the total cross section $P\bar{P}/PP \to t\bar{t}H + X$ is plagued by considerable uncertainties. This indicates that the LO results are not sufficient for a reliable prediction and underlines the need for the NLO corrections.

Chapter 4

Virtual Corrections

4.1 Preliminaries

For a consistent treatment of the virtual one-loop corrections the squared transition matrix element $|\mathcal{M}|^2$ has to be expanded into a power series of the strong coupling constant α_s,

$$|\mathcal{M}|^2 \;=\; |\mathcal{M}_{\rm LO}|^2 + 2{\rm Re}\left\{\mathcal{M}_{\rm LO}^\dagger \mathcal{M}_{\rm virtual}\right\} + \ldots, \tag{4.1}$$

for each channel, $q\bar{q}$ and gg. The diagrams contributing to $\mathcal{M}_{\rm virtual}$ are self-energies, vertex corrections, boxes, and pentagons. Typical representatives are depicted in Fig. 4.1. They are classified into three gauge-invariant groups. The first one contains all diagrams with closed fermion loops where the Higgs couples to one of the external heavy quarks. The second class includes all diagrams where the Higgs is radiated off from a closed fermion loop. All other diagrams containing at least one internal gluon in the loop are collected in the last class. Only diagrams of the first or the last group can be UV divergent. Since for the second set no corresponding ggH or $gggH$ coupling exists at tree level, which could produce a counter term, the sum of all diagrams in this group is UV finite. The Feynman gauge is applied to the internal gluons, hence ghosts have to be taken into account. In this gauge for the $q\bar{q}$ channel there are 2, 2, and 25 graphs in the three groups, respectively. For the gg channel the three classes contain 6, 20, and 108 diagrams. Each flavour in a closed loop is counted only once and tadpole diagrams are omitted since they vanish.

All UV and IR divergences are consistently regularized in Dimensional Regularization (DR); for the renormalization see Section 4.2. The loop integrals are reduced to standard integrals $B_{\mu\ldots}$, $C_{\mu\ldots}$, $D_{\mu\ldots}$, and $E_{\mu\ldots}$ (see Appendix C). The Passarino–Veltman reduction [103] to scalar integrals is applied to the tensor integrals. The tensor coefficients are calculated numerically in order to avoid huge algebraic expressions. The five-point function, which is particularly complicated, is discussed in Section 4.3 below.

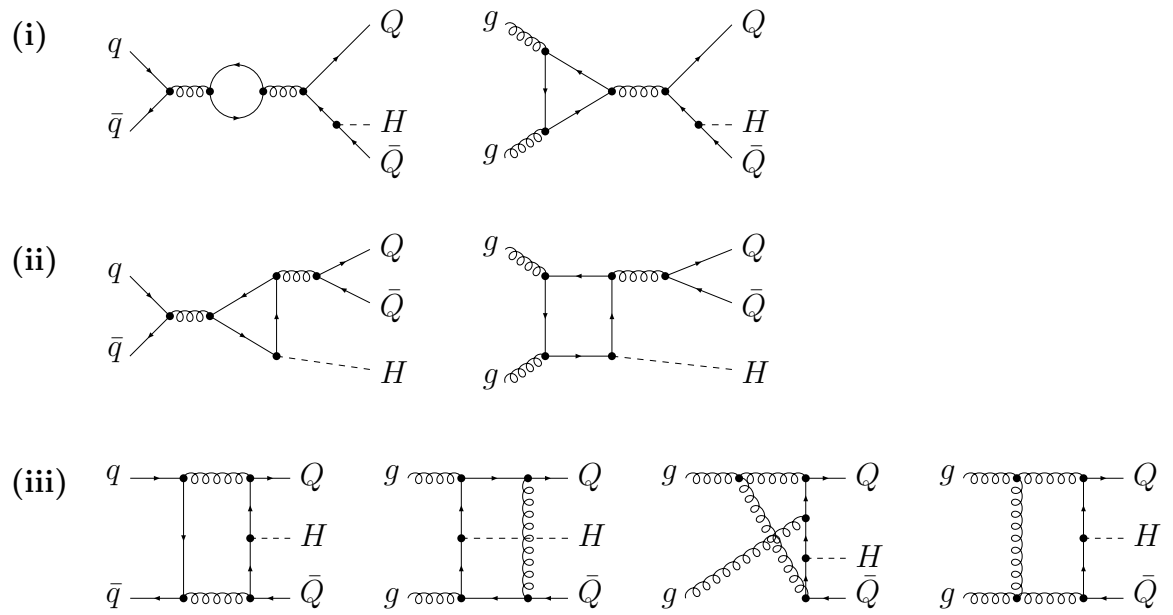

Figure 4.1: Some representatives of the gauge-invariant subsets (i)-(iii) of one-loop QCD diagrams, as described in the text.

For the calculation of the NLO term in Eq. (4.1) the virtual amplitude is decomposed into formfactors according to Eq. (3.12),

$$\mathcal{M}_{\text{virtual}} \;=\; \sum_{c,i} \mathcal{M}_i \, \mathcal{C}_c \, F_{i,c}^{\text{virtual}}. \tag{4.2}$$

Together with the analogous decomposition of the LO amplitude the contribution of the virtual corrections to the squared matrix element can be written as:

$$2\,\text{Re}\left\{\mathcal{M}_{\text{LO}}^{\dagger}\mathcal{M}_{\text{virtual}}\right\} \;=\; \sum_{c',c}\sum_{i',i}\left(\mathcal{M}_{i'}^{\dagger}\mathcal{M}_i\right)\left(\mathcal{C}_{c'}^{\dagger}\mathcal{C}_c\right) 2\,\text{Re}\left\{(F_{i',c'}^{\text{LO}})^{*}F_{i,c}^{\text{virtual}}\right\}. \tag{4.3}$$

4.2 The Renormalization Constants

As already mentioned in Section 2.5, the renormalization constants of the heavy quarks are determined in the on-shell scheme while the massless partons are renormalized in the $\overline{MS}$ scheme. For the renormalization constants of the gluon field as well as the strong coupling constant a modified $\overline{MS}$ scheme is adopted in which the contribution of the top quark is decoupled from the running of α_s. The explicit form of the renormalization constants

reads:

$$\delta m_Q = -\frac{\alpha_s}{4\pi} C_F\, m_Q \Big[3B_0(0;m_Q,m_Q)+4\Big], \tag{4.4}$$

$$\delta Z_Q = -\frac{\alpha_s}{4\pi} C_F \Big[B_0(0;m_Q,m_Q) - 4\,m_Q^2\, B_0'(m_Q^2;m_Q,0)\Big], \tag{4.5}$$

$$\delta Z_q = -\frac{\alpha_s}{4\pi} C_F\, \Delta_{UV}, \tag{4.6}$$

$$\delta Z_G = +\frac{\alpha_s}{4\pi}\left[\left(5-\frac{2}{3}N_f\right)\Delta_{UV} - \frac{2}{3}\sum_Q B_0(0;m_Q,m_Q)\right], \tag{4.7}$$

$$\delta g_s = -\frac{g_s}{2}\frac{\alpha_s}{4\pi}\left[\left(11-\frac{2}{3}N_f\right)\Delta_{UV} - \frac{2}{3}\sum_Q B_0(0;m_Q,m_Q)\right], \tag{4.8}$$

where the subscript UV emphasizes the UV property of the divergence and N_f denotes the number of light flavours. The scalar two-point function B_0 is defined in Eq. (C.1) and its derivative is given in Eq. (C.7).

Since the external self-energies of the massless particles do not vanish in the employed renormalization scheme, the LSZ factors for the external legs have to be taken into account. The derivation is presented in Appendix B. The result reads:

$$\delta\mathcal{Z}_q = -\frac{\alpha_s}{4\pi} C_F \Big[B_0(0;0,0) - \Delta_{UV}\Big], \tag{4.9}$$

$$\delta\mathcal{Z}_G = +\frac{\alpha_s}{4\pi}\left(5-\frac{2}{3}N_f\right)\Big[B_0(0;0,0) - \Delta_{UV}\Big]. \tag{4.10}$$

The explicit form of $B_0(0;0,0)$ is given in Eq. (C.6). Note that $\delta\mathcal{Z}_q$ and $\delta\mathcal{Z}_G$ contain IR divergences but are UV finite.

4.3 Five-Point Functions

The five-point functions are defined by

$$E_{\mu_1\cdots\mu_n} = \frac{(2\pi\mu)^{4-D}}{i\pi^2}\int d^Dk\,\frac{k_{\mu_1}\cdots k_{\mu_n}}{d_0d_1d_2d_3d_4} \tag{4.11}$$

with $d_i = (k+k_i)^2 - m_i^2 + 0i$.

In the case of a finite integral, and hence the feasibility of restricting D to four, a scalar five-point function can be expressed in terms of five scalar four-point functions [89,104,105],

$$E_0^{(D=4)} = \sum_{i=0}^{4} c_i D_0^{(D=4)}(i), \tag{4.12}$$

with real coefficients c_i. For the decomposition the integration momentum k is written as a linear combination of the four linearly independent momenta k_i. The integral $D_0(i)$ is obtained from E_0 by omitting the ith denominator d_i.

When dealing with soft or collinear divergent integrals the restriction to four dimensions is not possible anymore, and therefore the method above is not directly applicable. This problem is due to the use of DR. There are other regularization schemes that stick to four dimensions and thus circumvent this problem. Therefore the idea is to employ a mass regulator which works in four dimensions in an intermediate step and a definite transition from one regularization scheme to the other.

In detail the procedure works as follows [56]. In addition to the DR an infinitesimal mass regulator λ is introduced,

$$E_0^{(D)} \quad \to \quad E_0^{(D,\mathrm{mass})}, \tag{4.13}$$

where $E_0^{(D,\mathrm{mass})}$ reduces to $E_0^{(D)}$ if $\lambda = 0$. Now a new integral $E_{0,\mathrm{sing}}^{(D,\mathrm{mass})}$ with the same IR singularity structure as $E_0^{(D,\mathrm{mass})}$ is specified in a well-defined way. The new integrand is composed of three-point functions with purely kinematical prefactors which are regularization-scheme independent. Thus the difference $E_0^{(D,\mathrm{mass})} - E_{0,\mathrm{sing}}^{(D,\mathrm{mass})}$ is finite, uniquely defined, and regularization scheme independent in the limit $D \to 4$ and $\lambda \to 0$. Hence the limits $D \to 4$ and $\lambda \to 0$ commute and one obtains

$$E_0^{(D)} - E_{0,\mathrm{sing}}^{(D)} + \mathcal{O}(D-4) \quad = \quad E_0^{(D=4,\mathrm{mass})} - E_{0,\mathrm{sing}}^{(D=4,\mathrm{mass})} + \mathcal{O}(\lambda). \tag{4.14}$$

The simplest possible example for extracting the singular part is given by $E_0^{(D,\mathrm{mass})}(m_Q^2,$ $0,$ $0,$ $M_H^2,$ $m_Q^2,$ $s,$ $t_1,$ $s_1,$ $s_2,$ $t_2;$ $0,$ $m_Q,$ $m_Q,$ $m_Q,$ $m_Q)$, which occurs in diagrams with four internal heavy quarks and one internal gluon. In the limit $k \to 0$ two denominators remain finite,

$$\begin{aligned} d_2 &= k^2 + 2\,k\cdot k_2 + s - m_Q^2 \to s - m_Q^2, \\ d_3 &= k^2 + 2\,k\cdot k_3 + s_2 - m_Q^2 \to s_2 - m_Q^2, \end{aligned} \tag{4.15}$$

while the other three become singular,

$$d_0 = k^2 - \lambda^2 \to 0, \qquad d_1 = k^2 + 2\,k\cdot k_1 \to 0, \qquad d_4 = k^2 + 2\,k\cdot k_4 \to 0. \tag{4.16}$$

The function $E_{0,\mathrm{sing}}^{(D,\mathrm{mass})}$ is given by the three-point function that contains the three singular denominators multiplied by the other two denominators taken in the soft limit,

$$\begin{aligned} E_{0,\mathrm{sing}}^{(D,\mathrm{mass})}(m_Q^2,0,0,M_H^2,m_Q^2,s,t_1,s_1,s_2,t_2;0,m_Q,m_Q,m_Q,m_Q) \;=\; \\ \frac{1}{s-m_Q^2}\,\frac{1}{s_2-m_Q^2}\,C_0^{(D,\mathrm{mass})}(m_Q^2,m_Q^2,t_2;m_Q,0,m_Q). \end{aligned} \tag{4.17}$$

To obtain $E_{0,\mathrm{sing}}^{(D=4,\mathrm{mass})}$ or $E_{0,\mathrm{sing}}^{(D)}$ one only has to replace $C_0^{(D,\mathrm{mass})}$ by $C_0^{(D=4,\mathrm{mass})}$ or $C_0^{(D)}$, respectively. The explicit form of the singularity structure for all needed four- and five-point functions is given in Appendix C.

The decomposition of the five-point function into four-point functions, which works in four dimensions, can be applied to $E_0^{(D=4,\mathrm{mass})}$, and $E_0^{(D)}$ is obtained by

$$E_0^{(D)} = E_0^{(D=4,\mathrm{mass})} + \left[E_{0,\mathrm{sing}}^{(D)} - E_{0,\mathrm{sing}}^{(D=4,\mathrm{mass})}\right] + \mathcal{O}(D-4) + \mathcal{O}(\lambda), \tag{4.18}$$

where terms of higher order in $D-4$ or λ have been neglected. For the five-point scalar integrals it is possible to obtain a decomposition as in Eq. (4.12). For this purpose $E_0^{(D=4,\mathrm{mass})}$ is decomposed according to Eq. (4.12) with coefficients $\tilde{c}_i$,

$$E_0^{(D=4,\mathrm{mass})} = \sum_{i=0}^{4} \tilde{c}_i D_0^{(D=4,\mathrm{mass})}(i). \tag{4.19}$$

Next the procedure for switching between mass and dimensional regularization, Eq. (4.14), is applied to the four-point functions $D_0^{(D=4,\mathrm{mass})}(i)$,

$$D_0^{(D=4,\mathrm{mass})}(i) = D_0^{(D)}(i) - \left[D_{0,\mathrm{sing}}^{(D)}(i) - D_{0,\mathrm{sing}}^{(D=4,\mathrm{mass})}(i)\right] + \mathcal{O}(D-4) + \mathcal{O}(\lambda). \tag{4.20}$$

After inserting this into Eq. (4.18) one obtains

$$\begin{aligned} E_0^{(D)} &= \sum_{i=0}^{4} \tilde{c}_i D_0^{(D)}(i) - \sum_{i=0}^{4} \tilde{c}_i \left[D_{0,\mathrm{sing}}^{(D)}(i) - D_{0,\mathrm{sing}}^{(D=4,\mathrm{mass})}(i)\right] \\ &\qquad + \left[E_{0,\mathrm{sing}}^{(D)} - E_{0,\mathrm{sing}}^{(D=4,\mathrm{mass})}\right] + \mathcal{O}(D-4) + \mathcal{O}(\lambda) \\ &= \sum_{i=0}^{4} \tilde{c}_i D_0^{(D)}(i) + \mathcal{O}(D-4) + \mathcal{O}(\lambda). \end{aligned} \tag{4.21}$$

All integrals with subscript "sing" are linear combinations of independent three-point functions, which have either D dimensions or a mass regulator. The three-point functions with a mass regulator have zero coefficients because the decomposition method working in four dimensions is applicable. Since these coefficients are regularization-scheme independent, they are the same for both kinds of three-point functions. Hence the total sum of the integrals with subscript "sing" vanishes.

In this work Eq. (4.21) in D dimensions is used to calculate the five-point functions. Therefore all corresponding four-point functions are needed in D dimensions. They are listed in Appendix C together with the IR-divergent three-point functions. An alternative approach is to exploit Eq. (4.18) for the five-point as well as for the four-point functions. Hereby all IR divergences are embodied by three-point functions $C_{0,\mathrm{sing}}^{(D)}$. In this case the four-point functions are needed with mass regulator.

The decomposition of the five-point tensor integrals in terms of Lorentz covariants can be written as

$$\begin{aligned} E_\mu(p_1,p_2,p_3,p_4) &= \sum_{i=1}^{4} p_{i,\mu} E_i, \\ E_{\mu\nu}(p_1,p_2,p_3,p_4) &= \sum_{i,j=1}^{4} p_{i,\mu} p_{j,\nu} E_{ij} + \Delta g_{\mu\nu} E_{00}, \\ E_{\mu\nu\rho}(p_1,p_2,p_3,p_4) &= \sum_{i,j,k=1}^{4} p_{i,\mu} p_{j,\nu} p_{k,\rho} E_{ijk} + \sum_{i=1}^{4} \left(p_{i,\mu} \Delta g_{\nu\rho} + p_{i,\nu} \Delta g_{\mu\rho} + p_{i,\rho} \Delta g_{\mu\nu} \right) E_{00i}, \end{aligned} \tag{4.22}$$

where for the most general tensor in D dimensions the metric $g_{\mu\nu}$ is needed. It is more convenient to use $\Delta g_{\mu\nu} = g_{\mu\nu} - g_{\mu\nu}^{(D=4)}$ instead. Here $g_{\mu\nu}^{(D=4)}$ denotes the metric tensor in $D = 4$ dimensions, which can be expressed in terms of the four linearly independent vectors p_i,

$$g_{\mu\nu}^{(D=4)} = \sum_{i,j=1}^{4} \left(Z^{-1} \right)_{ij} p_{i,\mu} p_{j,\nu}, \qquad Z_{ij} = (p_i \cdot p_j). \tag{4.23}$$

None of the terms in Eq. (4.22) which are proportional to $\Delta g_{\mu\nu}$ contributes in the case of $Q\bar{Q}H$-production. The object $\Delta g_{\mu\nu}$ is of $\mathcal{O}(D-4)$ and can therefore only contribute if the corresponding tensor coefficient is divergent. The explicit tensor reduction reveals that they are finite. Only those covariants of tensor integrals receive divergent coefficients that are built by the singular regions in momentum space. Hence if the collinear divergence occurs for $k \to xp$ or the soft divergence at $k \to p$, only covariants corresponding to tensors of p alone become IR-divergent. Moreover, power counting shows that all relevant five-point integrals are UV finite.

4.4 The Endpoint Contribution

Within the subtraction formalism [61–63,106,107] the endpoint contribution is that part of the real corrections that has the same kinematics as the LO process and that is needed to cancel the IR divergences of the virtual corrections. Hence in a certain sense it belongs to the virtual corrections and is presented here although the real corrections will be treated in the next chapter.

For the endpoint contribution the LO amplitude has to be reordered in colour space. The matrix element

$$\left| \mathcal{M}_{\text{colour}}(j,k) \right|^2 = \langle \text{LO} | \, \mathbf{T}_j \cdot \mathbf{T}_k \, | \text{LO} \rangle \,, \tag{4.24}$$

will be used in the following, where j and k label initial as well as final-state partons. The explicit form of the colour operators $\mathbf{T}_j$ are given in Appendix D. The result of acting $\mathbf{T}_j \cdot \mathbf{T}_k$ on the colour structure $\mathcal{C}_m$ can be decomposed into a sum of colour structures,

$$(\mathbf{T}_j \cdot \mathbf{T}_k)\,\mathcal{C}_m \;=\; \sum_n c_{nm}^{jk} \mathcal{C}_n, \tag{4.25}$$

with real coefficients c_{nm}^{jk}. After defining the auxiliary formfactors

$$F_{i,n}^{\text{colour}}(j,k) \;=\; \sum_m c_{nm}^{jk} F_{i,m}^{\text{LO}}, \tag{4.26}$$

the colour-reordered matrix element can be calculated via

$$|\mathcal{M}_{\text{colour}}(j,k)|^2 \;=\; \sum_{c',c} \sum_{i',i} \Big[\mathcal{M}_{i'}^{\dagger} \mathcal{M}_i\Big] \Big[\mathcal{C}_{c'}^{\dagger} \mathcal{C}_c\Big] \Big[(F_{i',c'}^{\text{LO}})^* F_{i,c}^{\text{colour}}(j,k)\Big]. \tag{4.27}$$

For the $q\bar{q}$ channel $|\mathcal{M}_{\text{colour}}(j,k)|^2$ can be simplified to

$$|\mathcal{M}_{\text{colour}}(j,k)|^2 \;=\; c^{jk}\; |\mathcal{M}_{\text{LO}}|^2 \tag{4.28}$$

with the coefficients

$$c^{12} = c^{34} = +\frac{1}{6}, \qquad c^{13} = c^{24} = -\frac{7}{6}, \qquad c^{14} = c^{23} = -\frac{1}{3}. \tag{4.29}$$

This is possible because $\mathcal{M}_{\text{LO}}$ is proportional to $\mathcal{C}_1^{q\bar{q}}$, see Eq. (3.14), and the second independent colour structure $\mathcal{C}_2^{q\bar{q}}$ occurring in Eq. (4.25) is chosen to be orthogonal to $\mathcal{C}_1^{q\bar{q}}$, see Eq. (A.3).

The LO amplitude of the gg channel can be written in such a way that only the first two colour structures of Eq. (3.18) contribute. Therefore it is possible to restrict n to $1, 2$. The colour coefficients for the gg channel then read:

$$c_{nm}^{12} = \begin{pmatrix} -\frac{9}{4} & -\frac{3}{4} & 0 & +\frac{3}{4} \\ -\frac{3}{4} & -\frac{9}{4} & 0 & +\frac{3}{4} \end{pmatrix}, \qquad c_{nm}^{13} = c_{nm}^{24} = \begin{pmatrix} -\frac{3}{2} & 0 & 0 & 0 \\ +\frac{3}{4} & +\frac{3}{4} & 0 & -\frac{3}{4} \end{pmatrix},$$
$$c_{nm}^{34} = \begin{pmatrix} -\frac{7}{12} & -\frac{3}{4} & 0 & +\frac{3}{4} \\ -\frac{3}{4} & -\frac{7}{12} & 0 & +\frac{3}{4} \end{pmatrix}, \qquad c_{nm}^{14} = c_{nm}^{23} = \begin{pmatrix} +\frac{3}{4} & +\frac{3}{4} & 0 & -\frac{3}{4} \\ 0 & -\frac{3}{2} & 0 & 0 \end{pmatrix}. \tag{4.30}$$

The contributions to the endpoint $\mathcal{E}$ are structured by pairs of partons which occur in the combinations initial-initial, initial-final, and final-final. The origin of this structure will become clear when explaining the dipole subtraction formalism in Chapter 5. In the following a and b denote initial-state partons while j and k label final-state partons.

For each contribution the corresponding colour-reordered matrix element is multiplied by general functions $\mathcal{J}$,

$$\mathcal{E} = -\frac{\alpha_s}{2\pi}\left[\sum_{a\neq b}\mathcal{J}^{ab}\,|\mathcal{M}_{\text{colour}}(a,b)|^2+\sum_{a,j}\mathcal{J}^a_j\,|\mathcal{M}_{\text{colour}}(a,j)|^2+\sum_{j\neq k}\mathcal{J}_{jk}\,|\mathcal{M}_{\text{colour}}(j,k)|^2\right]. \tag{4.31}$$

The functions $\mathcal{J}$ are given by

$$\begin{aligned}
\mathcal{J}^{ab} &= \Delta_2(\hat{s})+\frac{\gamma_a}{\mathbf{T}_a^2}\,\Delta_1(\hat{s})-\frac{\pi^2}{3},\\
\mathcal{J}^a_j &= \Delta_2(m_Q^2-t_{aj})+\left(1+\ln\left(\bar{\mu}_Q^2\right)+\frac{\gamma_a}{\mathbf{T}_a^2}\right)\Delta_1(m_Q^2-t_{aj})-\frac{1}{2}\ln^2\left(\bar{\mu}_Q^2\right)\\
&\quad+\frac{1}{2}\ln\left(\bar{\mu}_Q^2\right)+\frac{1}{2}\ln\left(1+\bar{\mu}_Q^2\right)-2\text{Li}_2\left(-\bar{\mu}_Q^2\right)+\frac{3}{2}-\frac{2}{3}\pi^2+\frac{\bar{\mu}_Q^2}{2\left(1+\bar{\mu}_Q^2\right)},\\
\mathcal{J}_{jk} &= 2I_{\text{eik}}(\hat{\mu}_Q)+I_{\text{rem}}(\hat{\mu}_Q).
\end{aligned} \tag{4.32}$$

The integrals $I_{\text{eik}}(\hat{\mu}_Q)$ and $I_{\text{rem}}(\hat{\mu}_Q)$ are rather lengthy [61] and deferred to Appendix D. The following abbreviations for the poles in ε have been used

$$\Delta_1(m^2)=\frac{\Gamma(1+\varepsilon)}{\varepsilon}\left(\frac{4\pi\mu_{IR}^2}{m^2}\right)^{\varepsilon},\qquad \Delta_2(m^2)=\frac{\Gamma(1+\varepsilon)}{\varepsilon^2}\left(\frac{4\pi\mu_{IR}^2}{m^2}\right)^{\varepsilon}. \tag{4.33}$$

The two dimensionless parameters $\bar{\mu}_Q$ and $\hat{\mu}_Q$ are defined as

$$\bar{\mu}_Q^2 = \frac{m_Q^2}{2p_a\cdot p_j}=\frac{m_Q^2}{m_Q^2-t_{aj}}, \tag{4.34}$$

$$\hat{\mu}_Q^2 = \frac{m_Q^2}{(p_j+p_k)^2}=\frac{m_Q^2}{s_{jk}}. \tag{4.35}$$

The γ_a are called anomalous dimensions and are given by:

$$\gamma_q=\frac{3}{2}\,C_F,\qquad \gamma_g=\frac{11}{6}\,C_A-\frac{2}{3}\,T_R N_f. \tag{4.36}$$

The ε-poles in the endpoint contribution $\mathcal{E}$ exactly cancel the poles of the virtual corrections. This has been checked analytically against the results of Ref. [107] and also numerically. In addition, the sum of the virtual corrections and the endpoint contribution does not contain logarithms of the form $\alpha_s\ln(m_Q^2/\hat{s})$ for $\hat{s}\gg m_Q^2$ as explained in Ref. [61] since the subtraction function respects the so-called *quasi-collinear limit*. The avoidance of the terms $\alpha_s\ln(m_Q^2/\hat{s})$ is very useful for numerical stability in the high-energy limit.

4.5 Avoiding Numerical Instabilities

At the boundary of the PS the external momenta p_i are not linearly independent, which is equivalent to a vanishing Gram determinant $\det Z_{ij}$, with $Z_{ij} = (p_i \cdot p_j)$. Mathematically the boundary is a set of measure zero and does not disturb the integrability of the PS integral. But numerically a vanishing Gram determinant can cause instabilities because effectively zero divided by zero is evaluated in the Passarino–Veltman reduction. The adaptive Monte Carlo (MC) used for the PS integration generates most random points into the PS regions contributing most to the total result. In the small PS domain where the integrand is numerically unstable the evaluation yields a wrong result that can be far too large. Since the adaptive MC generates more and more points into this PS region, the integration leads to a wrong final result accompanied by a huge relative error.

Each rank of a tensor integral adds one factor of the Gram determinant in the denominator and hence increases the danger of numerical instabilities. Since the three- and four-point functions involve less external momenta than the five-point integral, the part of the PS boundary, in which the Gram determinant of the former tends to zero, is smaller than the corresponding region of the latter. In addition, the scalar five-point function is reduced to four-point functions and is hence evaluated less accurately than the scalar integrals with less external legs. Therefore the tensor integrals of the five-point function are more suspected to be endangered by numerical instabilities than tensor integrals of three- or four-point functions.

The simple solution of cutting-out all dangerous PS regions was rejected because of the potential loss of information contained in these domains. Instead an extrapolation procedure is employed to stabilize the integrand. First the dangerous PS regions were identified and described by cuts. When the MC integration routine dices a point inside this region, the matrix element is not only calculated directly but also an approximation of it is obtained by an extrapolation using results from the safe PS region. Both results are compared and if they deviate too much, a more precise extrapolation with more points is made. In the case of consistent extrapolations but a deviating direct result the value of the most reliable approximation is used. If in the end all extrapolated and the directly calculated results do not agree within a given accuracy the PS point is discarded. Owing to this procedure the integrand is calculated in a stable way and, in addition, the increasing generation of random points into the dangerous PS regions described above is avoided.

To be more precise, in terms of the PS parameterization (3.3) the Gram determinant can be written as

$$\begin{aligned} \det Z_{ij} &= \left(\frac{\hat{s}}{4}\right)^4 x_1\, x_2\, \beta_1\, \beta_2\, \sin^2\theta\, \sin^2\alpha\, \sin^2\beta \\ &= \left[\frac{\hat{s}^2}{8}\, \kappa(\tilde{x}_1^2, \tilde{x}_2^2, \tilde{x}_3^2)\, \sin\theta\, \sin\beta\right]^2, \end{aligned} \tag{4.37}$$

where $x_i = \frac{2}{\hat{s}} k_i^0$, $\beta_i = \sqrt{1 - k_i^2/(k_i^0)^2}$, and $\tilde{x}_i = x_i\, \beta_i$. One cut is applied to the dimen-

sionless quantity $\kappa(\tilde{x}_1^2, \tilde{x}_2^2, \tilde{x}_3^2) \sin\theta \sin\beta$ and another one to the azimuthal angle β around $\beta = 0$ and $\beta = \pi$. The latter is performed because most instabilities are already caught by this cut.

Inside the cuts first a one-dimensional extrapolation within the variable β is performed using a Fourier series with trigonometric functions. If necessary, this extrapolation is repeated with twice as many points. Secondly a similar extrapolation is carried out which is again one-dimensional but its independent variable does not coincide with the variable β but corresponds to a straight line through all integration variables of the three-particle PS. Again, if needed it is repeated with the number of points doubled. After each extrapolation the results are compared. If they agree within a given discrepancy, the most reliable result is returned else the next extrapolation is done. If no extrapolation fulfills the requirements the PS point is discarded.

The reliability of this procedure has been tested by choosing different extrapolation methods and by varying the PS cuts. It turned out that the result does not depend on the details of the procedure. This is a crucial requirement since otherwise one could not trust the result.

4.6 The Coulomb Singularity

Coulombic gluon exchange between the two outgoing heavy quarks enhances the QCD corrections near threshold, $\sqrt{\hat{s}} \gtrsim 2m_Q + M_H$. The generic diagram is depicted in Fig. 4.2. In the limit of vanishing gluon momentum the NLO matrix element, denoted by $\mathcal{M}_{\text{Coul}}$, becomes singular with a factor $1/\beta_{34}$,

$$\mathcal{M}_{\text{Coul}} = -\mathcal{M}_{\text{LO}} \otimes \frac{\pi\alpha_s}{4\beta_{34}} (\mathbf{T}_3\mathbf{T}_4), \tag{4.38}$$

where $\beta_{34} = \sqrt{1 - 4m_Q^2/s_{34}}$ is the relative velocity of the quark pair and tends to zero close to threshold. This is the well-known Sommerfeld rescattering correction [108]. At threshold the LO matrix element becomes constant. Averaging $1/\beta_{34}$ over the PS near threshold yields the Coulomb singularity for the partonic cross section

$$\sigma_{\text{Coul}} = \frac{8\alpha_s}{3}\sqrt{\frac{m_Q}{\mu_0}}\frac{C_{\text{Coul}}}{\beta}\sigma_{\text{LO}}, \tag{4.39}$$

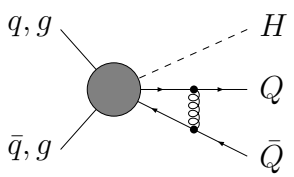

Figure 4.2: Generic diagram leading to the Coulomb singularity.

where $\mu_0 = m_Q + M_H/2$ is half the threshold energy and

$$\beta = \sqrt{1 - \frac{\mu_0^2}{\hat{s}}} \tag{4.40}$$

is proportional to the maximal value of β_{34}. The colour factor C_{Coul} is given by

$$C_{\text{Coul}} = -\frac{\langle \text{LO}| \mathbf{T}_3 \cdot \mathbf{T}_4 |\text{LO}\rangle}{\langle \text{LO}|\text{LO}\rangle}. \tag{4.41}$$

The explicit calculation results

$$C_{\text{Coul}}^{q\bar{q}} = -\frac{1}{6}, \quad C_{\text{Coul}}^{gg} = \frac{11}{42}\frac{(4m_Q^2 - M_H^2)^2 - \frac{9}{11}M_H^4}{(4m_Q^2 - M_H^2)^2 - \frac{9}{7}M_H^4}, \quad C_{\text{Coul}}^{e^+e^-} = +\frac{4}{3}. \tag{4.42}$$

For the $q\bar{q}$ channel it can directly be read off from Eq. (4.29). The quark pair is generated via a gluon and hence in a colour-octet state. $C_{\text{Coul}}^{q\bar{q}}$ is negative and quite small. In gg scattering two colour amplitudes contribute in LO. Since they are reweighted differently, as can be seen from Eq. (4.30), C_{Coul}^{gg} is not a simple number, but depends on the ratio M_H/m_Q. For Higgs masses roughly below 250 GeV the corrections are positive and in size comparable to the one of the $q\bar{q}$ channel.

Since $\langle\sqrt{\hat{s}}\rangle > 2\mu_0$, and owing to Eq. (4.42) no large Coulomb effects are expected at the TEVATRON nor the LHC. By contrast, in e^+e^- annihilation the situation is quite different [49–51]. Since the quark pair is produced in a colour-singlet state, $C_{\text{Coul}}^{e^+e^-}$ is positive and in addition relatively large. Therefore the cross section near threshold is strongly enhanced by the Coulomb singularity.

Chapter 5

Real Corrections

5.1 General Remarks

As already mentioned in Chapter 2, for the consistent treatment of the NLO corrections to a total cross section the real corrections have to be taken into account. For the process of interest in this work there are four different kinds of real corrections which contribute incoherently:

$$\begin{aligned} q(p_1) + \bar{q}(p_2) &\rightarrow Q(p_3) + \bar{Q}(p_4) + H(p_5) + g(p_6), \\ g(p_1) + g(p_2) &\rightarrow Q(p_3) + \bar{Q}(p_4) + H(p_5) + g(p_6), \\ g(p_1) + q(p_2) &\rightarrow Q(p_3) + \bar{Q}(p_4) + H(p_5) + q(p_6), \\ g(p_1) + \bar{q}(p_2) &\rightarrow Q(p_3) + \bar{Q}(p_4) + H(p_5) + \bar{q}(p_6). \end{aligned} \tag{5.1}$$

This list only contains the different partonic processes. Since each initial-state parton can come from each hadron, there are actually eight partonic reactions at the hadron level. Typical diagrams of the partonic processes are depicted in Fig. 5.1. While the transition matrix elements of all four reactions contain collinear divergences which are balanced by the factorization of the parton densities, only the first two processes are further affected by soft divergences. These divergences cancel the ones of the virtual corrections.

The diagrams are calculated with the program MadGraph [109] which automatically generates Feynman diagrams and a corresponding FORTRAN code to calculate tree-level

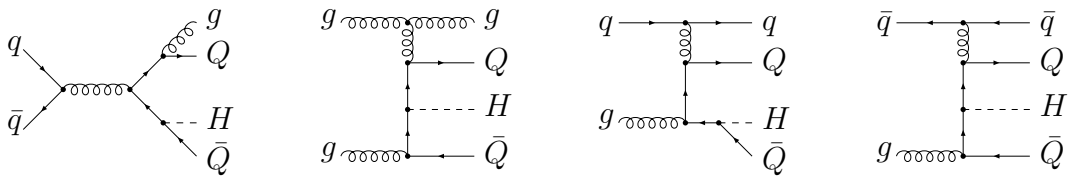

Figure 5.1: Some representatives for the four different kinds of real corrections.

helicity amplitudes by calling HELAS [110] subroutines. The results have been checked against a second independent calculation. Helicity-amplitude methods first sum the diagrams before squaring them. Hence the complexity grows linearly with the number of diagrams and not quadratically as in the case of trace techniques. However, the code generated by MadGraph is not designed for optimal speed or stability. Therefore a possible future improvement with respect to both, speed and stability, is the recalculation of the diagrams exploiting the Weyl–van der Waerden (WvdW) formalism [111–119] which is a special kind of the helicity-amplitude methods. It makes use of Weyl spinors instead of Dirac spinors. Since all four-vectors are expressed in terms of spinors, all spinor chains and all scalar products of four-vectors are reduced to the same mathematical objects, namely spinor products. Hence cancellations often take place at the analytical level and not only numerically. This leads to very compact results whose evaluation is numerically stable.

After calculating the amplitude, the obtained transition matrix element has to be integrated over the four-particle phase space. Since this integration leads to soft and collinear divergences, the singularities have to be treated properly. This is done by applying the dipole subtraction method, as explained in Section 5.3.

5.2 The Four-Particle Phase Space

The four-particle PS R_4 with total momentum p is most conveniently constructed from three two-particle PSs [120],

$$\begin{aligned} R_4(p^2, m_1^2, m_2^2, m_3^2, m_4^2) &= \int \left(\prod_{i=1}^{4} \frac{d^3\mathbf{p}_i}{(2\pi)^3\, 2p_i^0} \right) (2\pi)^4\, \delta^4 \left(p - \sum_{i=1}^{4} p_i \right) \\ &= \frac{1}{(2\pi)^8} \int\limits_{m_1+m_2}^{\sqrt{p^2}-m_3-m_4} 2M_1\, dM_1 \int\limits_{m_3+m_4}^{\sqrt{p^2}-M_1} 2M_2\, dM_2 \\ &\quad \times R_2(p^2, M_1, M_2)\, R_2(M_1^2, m_1, m_2)\, R_2(M_2^2, m_3, m_4), \end{aligned} \tag{5.2}$$

where m_i $(i = 1, \ldots, 4)$ are the masses of the final-state particles. This PS is only needed in four space-time dimensions. Its construction can be depicted as the decay of one incoming particle into two intermediate particles with virtuality $M_i = \sqrt{q_i^2}$ (see Fig. 5.2). The latter in turn decay into two particles, leading to a one-to-four process. The two-particle PS R_2 contains only the integration over a solid angle,

$$\begin{aligned} R_2(q^2, m_1, m_2) &= \left(\prod_{i=1}^{2} \frac{d^3\mathbf{p}_i}{(2\pi)^3\, 2p_i^0} \right) (2\pi)^4\, \delta^4 \left(q - \sum_{i=1}^{2} p_i \right) \\ &= (2\pi)\, \frac{\kappa(q^2, m_1^2, m_2^2)}{8q^2} \int d\Omega_1^*, \end{aligned} \tag{5.3}$$

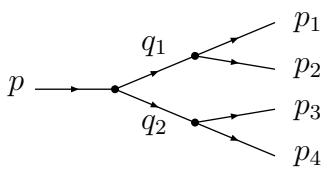

Figure 5.2: Structural diagram for constructing the four-particle PS from two-particle PSs.

where Ω_1^* denotes the solid angle of one of the final particles in the rest frame of q. Hence for constructing the momenta of the final-state particles in the CMS of the four-particle PS all momenta have to be boosted.

As in the case of the three-particle PS (see Section 3.1) the integration over the azimuthal angle around the beam axis in $R_2(p^2, M_1, M_2)$ can be performed in a trivial way due to rotational invariance. The result is a factor 2π.

5.3 The Dipole Subtraction Formalism

The total PS integral for the processes (5.1) cannot be performed directly in four dimensions due to the IR (soft and collinear) singularities. Two entirely different methods for solving this problem are available. In the first method the PS is subdivided into a part that leads to divergences and the finite remainder. The integration over the latter is finite and can be performed in four dimensions. The integration over the former requires regulators and will be explained later. This procedure is referred to as the *PS slicing method*. A recent review article can be found in Ref. [121].

The other possibility is to subtract an auxiliary function with the same pointwise singularity structure from the cross section. Since the difference is finite everywhere, the integration over this difference can be performed over the whole PS in four dimensions. Clearly the subtracted function has to be readded. The construction of such a function is very complicated but possible in a general way, because in the soft and collinear limits the squared matrix element of the real corrections fulfills the factorization properties of QCD [100, 122, 123]. In these limits the matrix element of the real corrections factorizes into the matrix element of the LO process times general process-independent factors. In addition, the PS of the massless particle that causes the singularities can be split from the remaining PS. The constructed auxiliary function can be chosen simple enough, so that it can be integrated over this one-particle PS analytically. This procedure is known as the *subtraction formalism* [61–63, 106, 107, 124–129].

As known from various examples [106, 130] the subtraction method is usually numerically more stable than the slicing method and needs less points for the MC integration, and

hence less computer time, to obtain a reliable result. Therefore this procedure is employed in this work. In addition the PS slicing method is used as an independent check in the $q\bar{q}$ channel, see Section 5.6 for more details.

In this work a special version of the subtraction formalism, called the *dipole subtraction formalism* [62,63], is adopted. It has recently been extended to the case of massive partons in the final state [61], which is needed for $Q\bar{Q}H$ production. In the rest of this section the general idea is explained before the explicit formulae needed are given in the following sections.

The NLO corrections to a process involving m particles in the final state consist of virtual and real corrections plus the collinear counter term stemming from the factorization (see Eq. (2.31)):

$$\Delta\sigma^{\mathrm{NLO}} = \int_m d\sigma^{\mathrm{virtual}} + \int_{m+1} d\sigma^{\mathrm{real}} + \int_m \int dx\, d\sigma^{\mathrm{coll}}(x). \tag{5.4}$$

The labels m and $(m+1)$ indicate the m and $(m+1)$ particle kinematics of the different final states, respectively. The auxiliary function, which is subtracted and readded, can symbolically be written as

$$\int_{m+1} d\sigma^{\mathrm{aux}} = \int_m \int_1 d\sigma^{\mathrm{aux}} = \int_m \int dx\, d\tilde{\sigma}^{\mathrm{aux}}(x). \tag{5.5}$$

The splitting of the $(m+1)$ particle PS into the m particle PS times the one-particle PS of the massless parton requires a convolution over a momentum fraction x if an initial-state parton is involved. The integral over x becomes divergent for $x \to 1$ and hence must be regulated. This is done by introducing "+" distributions, as defined in Eq. (2.53), and separating the endpoint contribution. The same splitting is applied to the counter term $d\sigma^{\mathrm{coll}}$,

$$\begin{aligned} \int_m \int dx\, d\tilde{\sigma}^{\mathrm{aux}}(x) &= \int_m \int dx\, d\tilde{\sigma}_+^{\mathrm{aux}}(x) + \int_m d\tilde{\sigma}_1^{\mathrm{aux}}, \\ \int_m \int dx\, d\sigma^{\mathrm{coll}}(x) &= \int_m \int dx\, d\sigma_+^{\mathrm{coll}}(x) + \int_m d\sigma_1^{\mathrm{coll}}, \end{aligned} \tag{5.6}$$

where the subscript + labels the part containing the "+" distributions and the subscript 1 labels the endpoint. The exact form of the endpoint depends on the way, how the limit $x \to 1$ is achieved. This subtlety will be discussed in Section 5.5. Collecting all parts, the NLO corrections can be written as

$$\begin{aligned} \Delta\sigma^{\mathrm{NLO}} = & \int_m \left[d\sigma^{\mathrm{virtual}} + d\tilde{\sigma}_1^{\mathrm{aux}} + d\sigma_1^{\mathrm{coll}} \right]_{D=4} + \int_{m+1} \left[(d\sigma^{\mathrm{real}})_{D=4} - (d\sigma^{\mathrm{aux}})_{D=4} \right] \\ & + \int_m \int dx \left[d\tilde{\sigma}_+^{\mathrm{aux}}(x) + d\sigma_+^{\mathrm{coll}}(x) \right]_{D=4}, \end{aligned} \tag{5.7}$$

where each bracket is finite. The endpoint contributions balance exactly the soft and collinear divergences of the virtual corrections and have already been presented in Section 4.4. A similar cancellation takes place for the divergences in the convolution.

The auxiliary cross section $d\sigma^{\text{aux}}$ is constructed from process-independent building blocks, namely from a sum over ordered parton pairs, called *dipoles*. These two partons are called *emitter* and *spectator*. The kinematics of the former causes the singularities, while the latter is needed for momentum and colour conservation. Symbolically the function $d\sigma^{\text{aux}}$ can be written as

$$d\sigma^{\text{aux}} = \sum_{\text{dipoles}} d\sigma^{\text{LO}} \otimes dV_{\text{dipole}}, \tag{5.8}$$

where the $\otimes$ sign denotes possible spin and colour correlations. The dipole terms dV_{dipole} are constructed such that $d\sigma^{\text{aux}}$ has the same behaviour as $d\sigma^{\text{real}}$ in the soft and collinear limits. In addition, $d\sigma^{\text{LO}}$ in Eq. (5.8) only depends on the m particle kinematics and the whole dependence on the one-particle PS of the massless parton is contained in dV_{dipole}. Hence the integration over the one-particle PS can be performed analytically, leading to

$$\begin{aligned} \int_1 d\sigma^{\text{LO}} \otimes dV_{\text{dipole}} &= \int dx\, d\sigma^{\text{LO}} \otimes \widetilde{V}_{\text{dipole},x} \\ &= d\sigma^{\text{LO}} \otimes \widetilde{V}_{\text{dipole},1} + \int dx\, d\sigma^{\text{LO}} \otimes \widetilde{V}_{\text{dipole},+}\,. \end{aligned} \tag{5.9}$$

Equation (5.9) provides an expression for the readded subtraction function, $d\tilde{\sigma}_i^{\text{aux}} = d\sigma^{\text{LO}} \otimes \widetilde{V}_{\text{dipole},i}$ with $i = 1, +$.

The functions dV_{dipole}, $\widetilde{V}_{\text{dipole},1}$, and $\widetilde{V}_{\text{dipole},+}$ have been worked out in Ref. [63] for massless partons and in Ref. [61] for the case of massive final-state partons. To employ this subtraction formalism these building blocks have to be combined accordingly. Thereby special care has to be taken with respect to the "+" distribution because the parton densities are also affected by them.

For a detailed explanation of the construction and integration of the dipole terms, the reader is referred to the original literature. In the next two sections, only the formulae to construct the auxiliary function for the special case of $Q\bar{Q}H$ production in hadron collisions are given.

5.4 The Subtraction Function

In this section the subtraction function $|\mathcal{M}_{\text{aux}}|^2$ will be formulated at the level of the squared matrix elements. The connection to $d\sigma^{\text{aux}}$ is rather simple,

$$d\sigma^{\text{aux}} = \frac{1}{2\hat{s}}\, d\text{PS}\ |\mathcal{M}_{\text{aux}}|^2\,. \tag{5.10}$$

The convolution with the parton densities is suppressed in the notation throughout this chapter.

The indices a and b label initial-state partons, while i, j, and k label final-state partons. These numbers are identical to the labeling of the momenta in Eq. (5.1). Furthermore, $i = 6$ denotes the massless particle (gluon or quark) in the final state where the kinematics causes singularities. The auxiliary function $|\mathcal{M}_{\text{aux}}|^2$ receives four types of contributions from the four different combinations of initial- and final-state partons for the emitter and spectator,

$$|\mathcal{M}_{\text{aux}}|^2 = \sum_{j=3,4} \sum_{\substack{k=3,4 \\ k\neq j}} \mathcal{D}_{j6,k} + \sum_{j=3,4} \sum_{a=1,2} \mathcal{D}^a_{j6} + \sum_{j=3,4} \sum_{a=1,2} \mathcal{D}^{a6}_{j} + \sum_{a=1,2} \sum_{\substack{b=1,2 \\ b\neq a}} \mathcal{D}^{a6,b}. \quad (5.11)$$

The functions $\mathcal{D}$ are proportional to the LO matrix element which first has to be reordered in colour space,

$$\mathcal{D}_{j6,k} = -\frac{1}{(p_j + p_6)^2 - m_Q^2} \mathbf{V}_{j6,k} \left\langle |\mathcal{M}_{\text{colour}}(j6,k)|^2 \right\rangle, \quad (5.12)$$

$$\mathcal{D}^a_{j6} = -\frac{1}{(p_j + p_6)^2 - m_Q^2} \frac{1}{x_{j6,a}} \mathbf{V}^a_{j6} \left\langle |\mathcal{M}_{\text{colour}}(j6,a)|^2 \right\rangle, \quad (5.13)$$

$$\mathcal{D}^{a6}_{j} = -\frac{1}{2p_a \cdot p_6} \frac{1}{x_{j6,a}} \mathbf{V}^{a6,\mu\nu}_{j} \left\langle |\mathcal{M}_{\text{colour}}(a6,j)|^2_{\mu\nu} \right\rangle, \quad (5.14)$$

$$\mathcal{D}^{a6,b} = -\frac{1}{2p_a \cdot p_6} \frac{1}{x_{6,ab}} \mathbf{V}^{a6,b,\mu\nu} \left\langle |\mathcal{M}_{\text{colour}}(a6,b)|^2_{\mu\nu} \right\rangle. \quad (5.15)$$

The definition of $|\mathcal{M}_{\text{colour}}(j6,k)|^2$ is given in Eq. (4.24). The bracket indicates that the averaging over the spin and colour degrees of the incoming partons has already been performed. The explicit form of the functions $\mathbf{V}$ and the definition of the variables $x_{j6,a}$ and $x_{6,ab}$ are not needed here and can be found in Appendix D. If the parton that stems from the splitting of an initial-state particle and that enters the hard process is a gluon, its spin correlation has to be considered. The object $|\mathcal{M}_{\text{colour}}(a6,b)|^2_{\mu\nu}$ is obtained from the colour-reordered LO matrix element by leaving out the contraction with the polarization sum of the incoming gluon. Hence, it is related to the contracted matrix element by

$$\left(-g^{\mu\nu} + \frac{p_1^\mu p_2^\nu + p_2^\mu p_1^\nu}{p_1 \cdot p_2}\right) |\mathcal{M}_{\text{colour}}(a6,b)|^2_{\mu\nu} = |\mathcal{M}_{\text{colour}}(a6,b)|^2. \quad (5.16)$$

This relation also holds when replacing b by j.

The matrix element $|\mathcal{M}_{\text{colour}}|^2$ is defined with a three-particle kinematics, while $|\mathcal{M}_{\text{aux}}|^2$ exhibits a four-particle kinematics. To get from the latter to the former the particle i responsible for the singularities is combined with the emitter j to a single parton $\widetilde{ji}$ with mass m_{ji}. If the emitter is an initial-state parton, the index j has to be replaced by the index a. This leads to a construction of an m particle PS whose momenta are denoted by $\tilde{p}_l$. The mapping of the momenta with $(m+1)$ particle kinematics onto the momenta

of the m particle PS, $p_l^\mu \to \tilde{p}_l^\mu$, is done in such a way that all on-shell conditions and momentum conservation are fulfilled. In addition, the $\tilde{p}_l^\mu$ are identical with the p_l^μ if $p_{i=6}^\mu$ goes to zero and $\tilde{p}_{ji}$ tends to $p_j + p_i$ in the collinear limit. The mapping differs whether the emitter and spectator are initial- or final-state particles. Their explicit forms are presented in Appendix D.

5.5 The Readded Subtraction Function

The readded subtraction function is given by

$$\int dx\, d\tilde{\sigma}^{\mathrm{aux}}(x) \;=\; \int dx\, \frac{1}{2\hat{s}}\, d\mathrm{PS}\, \left|\widetilde{\mathcal{M}}_{\mathrm{aux}}(x)\right|^2. \tag{5.17}$$

Again, the convolution with the parton densities is suppressed in the notation. The quantity $\left|\widetilde{\mathcal{M}}_{\mathrm{aux}}(x)\right|^2$ denotes the auxiliary cross section integrated over the PS of the single parton that causes the singularities,

$$\begin{aligned}\left|\widetilde{\mathcal{M}}_{\mathrm{aux}}(x)\right|^2 &= \int_1 [dp_i(p_e,p_s,x)]\; |\mathcal{M}_{\mathrm{aux}}|^2 \qquad (5.18)\\ &= \sum_{j=3,4}\sum_{\substack{k=3,4\\k\neq j}} \mathcal{I}_{j6,k} + \sum_{j=3,4}\sum_{a=1,2} \mathcal{I}^a_{j6}(x) + \sum_{j=3,4}\sum_{a=1,2} \mathcal{I}^{a6}_{j}(x) + \sum_{a=1,2}\sum_{\substack{b=1,2\\b\neq a}} \mathcal{I}^{a6,b}(x).\end{aligned}$$

The one-particle PS $[dp_i(p_e,p_s,x)]$ depends on the momenta p_e and p_s of the emitter and the spectator, respectively. In addition, it includes a convolution, indicated by the appearance of x, if an initial-state parton is involved.

The functions $\mathcal{I}$ in Eq. (5.18) are the four different contributions to $\mathcal{M}_{\mathrm{aux}}$ in Eq. (5.11) integrated over the one-particle PS. They are proportional to the colour-reordered LO matrix element,

$$\mathcal{I}(x) \;=\; \mathcal{V}(x)\, \left\langle |\mathcal{M}_{\mathrm{colour}}(x)|^2 \right\rangle. \tag{5.19}$$

For the case of a final-state emitter and a final-state spectator no convolution is involved. Hence the corresponding contribution to the readded function contains only the endpoint,

$$\mathcal{V}_{Q_j g_i,k}(x) \;=\; -\frac{\alpha_s}{2\pi}\, \delta(1-x)\, \mathcal{J}_{Q_j g_i,k}. \tag{5.20}$$

The quantity $\mathcal{J}_{Q_j g_i,k} \equiv \mathcal{J}_{jk}$ has already been given in Eq. (4.32).

The contribution of a final-state emitter and an initial-state spectator is given by

$$\begin{aligned}\mathcal{V}^a_{Q_j g_i}(x) \;=\; -\frac{\alpha_s}{2\pi} \Bigg\{ &\left(\frac{1-x}{2(1-x+\mu_Q^2)} - \frac{2}{1-x}\Big[1+\ln\left(1-x+\mu_Q^2\right)\Big] \right)_+ \\ &+ \left(\frac{2}{1-x}\right)_+ \ln\left(2-x+\mu_Q^2\right) + \delta(1-x)\, \mathcal{J}^a_{Q_j g_i} \Bigg\}, \end{aligned} \tag{5.21}$$

where $\mathcal{J}^a_{Q_j g_i}$ can be found in Eq. (D.19). The definition of μ_Q^2 is

$$\mu_Q^2 \;=\; \frac{m_Q^2}{2\tilde{p}_{ji}\cdot p_a}, \tag{5.22}$$

and the scalar product reads

$$2\tilde{p}_{ji}\cdot p_a = \frac{2\tilde{p}_{ji}\cdot \tilde{p}_a}{x} = \frac{m_Q^2 - \tilde{t}_{a,ji}(x)}{x}. \tag{5.23}$$

The momenta with a tilde are used for calculating $\left|\widetilde{\mathcal{M}}_{\text{aux}}(x)\right|^2$. They depend on x and their explicit form is given in Eq. (D.17) after replacing $x_{ji,a}$ by x. At the endpoint ($x = 1$) μ_Q coincides with $\bar{\mu}_Q$ defined in Eq. (4.34). As already mentioned in Section 5.3, the explicit form of the endpoint depends on how the limit $x \to 1$ is reached. In this special case it is done with the condition, that μ_Q is kept constant. For evaluating the "+" distributions, the LO matrix element times parton distributions is needed twice, first using x-dependent kinematics and secondly using the kinematics with $x = 1$. Hence the PS parameterization must be chosen in such a way, that $2\tilde{p}_{ji}\cdot p_a$ is independent of x. A simple way to ensure this, is to use the scalar product in Eq. (5.23) as an integration variable.

The "+" distributions are constructed in such a way that all terms behave smoothly in the quasi-collinear limit [61]. This behaviour leads to the property that in the massless limit $\mu_Q \to 0$ no large logarithms of the form $\alpha_s \ln(m_Q^2/\hat{s})$ are produced in the continuum part of the readded subtraction function because they have been shifted into the endpoint contribution. This improves the numerical stability when dealing with small but finite masses, which is very useful when dealing with bottom quarks.

As can be seen in Appendix D, the kinematical situation is the same for an initial-state emitter with a final-state spectator as in the previous case. For consistence the indices have to be changed to $ji \to j$ and $a \to ai$. The integrated dipole function reads

$$\begin{aligned}
\mathcal{V}_j^{ai}(x) \;=\; -\frac{\alpha_s}{2\pi}\,\frac{1}{\mathbf{T}_{ai}^2}\Bigg\{ & -\Delta_1(2\tilde{p}_j\cdot p_a)P^{a,ai}(x) + 2P^{a,ai}_{\text{reg}}(x)\ln\left[\frac{(1-x)^2}{1+\mu_Q^2-x}\right] + V^{a,ai}(x) \\
& + \delta^{a,ai}\,\mathbf{T}_a^2\left[4\left(\frac{\ln(1-x)}{1-x}\right)_+ - \left(\frac{2}{1-x}\right)_+ \ln\left(2-x+\mu_Q^2\right)\right] \\
& + \delta^{ai,g}\,\mathbf{T}_a^2\,\frac{2\mu_Q^2}{x}\ln\left(\frac{\mu_Q^2}{1-x+\mu_Q^2}\right) + \delta(1-x)\,\delta^{a,ai}\,\mathbf{T}_a^2\,\mathcal{J}_j^{ai}\Bigg\},
\end{aligned} \tag{5.24}$$

where μ_Q^2 is obtained from Eq. (5.22) after replacing $\tilde{p}_{ji} \to \tilde{p}_j$ and $\tilde{p}_a \to \tilde{p}_{ai}$. The quantity $\mathcal{J}_j^{ai}$ is given in Eq. (D.22). The functions $V^{a,ai}(x)$ are defined as follows:

$$V^{qq}(x) = V^{qg}(1-x) = C_F\,(1-x), \quad V^{gq}(x) = 2\,T_R\,x(1-x), \quad V^{gg}(x) = 0. \tag{5.25}$$

Finally, in the case of an initial-state emitter with an initial-state spectator the integrated dipole function is given by

$$\mathcal{V}^{ai,b}(x) = -\frac{\alpha_s}{2\pi}\frac{1}{\mathbf{T}_{ai}^2}\Big\{ -\Delta_1(2p_a\cdot p_b)P^{a,ai}(x) + 2P_{\rm reg}^{a,ai}(x)\ln(1-x) + V^{a,ai}(x) + \delta^{a,ai}\,\mathbf{T}_a^2\,4\left(\frac{\ln(1-x)}{1-x}\right)_+ + \delta(1-x)\,\delta^{a,ai}\,\mathbf{T}_a^2\,\mathcal{J}^{ai,b}\Big\}, \quad (5.26)$$

with the scalar product $2p_a\cdot p_b = 2\tilde{p}_{ai}\cdot\tilde{p}_b/x = \tilde{s}(x)/x$ and $\mathcal{J}^{ai,b}\equiv\mathcal{J}^{ab}$ already defined in Eq. (4.32). The comments after Eq. (5.23) apply here, too. But since $\hat{s} = 2\,p_a\cdot p_b$ only depends on the product x_1x_2 of the momentum fractions of the incoming partons and the fixed hadronic energy s, it is straight forward to fulfill the condition in the PS parameterization that $\hat{s}$ has to be independent of x.

As already mentioned, the collinear divergences proportional to the splitting functions are removed by the renormalization of the parton densities which leads to the contribution $d\sigma_+^{\rm coll}(x)$ in Eq. (5.7). After adding this collinear counter term, "renormalized" integrated dipole functions are obtained from the functions above by the replacement

$$\Delta_1(M^2)P^{a,ai}(x) \to \ln\left(\frac{\mu_F^2}{M^2}\right)P^{a,ai}(x). \quad (5.27)$$

Eq. (5.27) is only valid within the $\overline{MS}$ scheme. When adopting other factorization schemes additional finite terms have to be supplemented.

5.6 The Slicing Method

The slicing method is used for an independent check for the subprocess $q\bar{q}\to Q\bar{Q}H$. Therefore all formulae given in this section are restricted to this case.

In the slicing method the PS is divided into two parts: the IR region, $\mathrm{PS}_{\rm soft+col}$, and the remaining one, $\mathrm{PS}_{\rm rem}$. The former covers all parts of the PS where the matrix element becomes singular, while in the latter the integrand is finite everywhere. Therefore the integral over $\mathrm{PS}_{\rm rem}$ can be performed in four dimensions. In the IR region the factorization properties of the matrix element admits to integrate out the one-particle PS of the gluon within the D-dimensional PS.

In the two-cutoff variant of the slicing method, which is explained in the following, the IR region is subdivided into the soft and the collinear region, denoted by $\mathrm{PS}_{\rm soft}$ and $\mathrm{PS}_{\rm coll}$, respectively.

The soft region is defined by the condition that the energy p_6^0 of the gluon in the partonic CMS is smaller than a given cut ΔE which itself is much smaller than the masses involved in the process:

$$0 < p_6^0 < \Delta E \ll M_H, m_Q. \quad (5.28)$$

In this region the gluon radiation is described by an eikonal current (see e.g. Ref. [62,63]). Similar to the endpoint contribution of the subtraction formalism the soft part receives contributions which are structured by unordered pairs of partons. Each contribution is the D-dimensional integral over the soft region,

$$d\sigma_{\rm soft} = d\sigma_{\rm LO} \otimes \frac{\alpha_s}{\pi} \sum_{\substack{j,k=1 \\ j<k}}^{4} (\mathbf{T}_j \cdot \mathbf{T}_k)\; f_{jk}(p_j,p_k), \tag{5.29}$$

$$f_{jk}(p_j,p_k) = \frac{(2\pi\mu_{IR})^{2\varepsilon}}{2\pi} \int_{p_6^0<\Delta E} \frac{d^{D-1}\mathbf{p}_6}{p_6^0} \frac{(p_jp_k)}{(p_jp_6)(p_kp_6)}. \tag{5.30}$$

The integrals for the different combinations of partons read

$$f_{12}(p_1,p_2) = \Delta_2(4\Delta E^2) - \frac{\pi^2}{3}, \tag{5.31}$$

$$\begin{aligned} f_{aj}(p_a,p_j) = {} & \frac{1}{2}\,\Delta_2(4\Delta E^2) + \left[\frac{1}{2} - \ln\left(\frac{p_ap_j}{p_a^0 m_Q}\right)\right] \Delta_1(4\Delta E^2) \\ & - \frac{\pi^2}{6} - \frac{1}{4}\ln^2\left(\frac{1-\beta_j}{1+\beta_j}\right) - \frac{1}{2\beta_j}\ln\left(\frac{1-\beta_j}{1+\beta_j}\right) \\ & - \mathrm{Li}_2\left(1 - \frac{p_a^0p_j^0(1-\beta_j)}{p_ap_j}\right) - \mathrm{Li}_2\left(1 - \frac{p_a^0p_j^0(1+\beta_j)}{p_ap_j}\right), \end{aligned} \tag{5.32}$$

$$\begin{aligned} f_{34}(p_3,p_4) = {} & \frac{1}{\beta_{34}}\Bigg\{ - \Delta_1(4\Delta E^2)\ln(\alpha_{34}) \\ & + \left[\frac{1}{4}\ln^2\left(\frac{u^0-|\mathbf{u}|}{u^0+|\mathbf{u}|}\right) + \mathrm{Li}_2\left(1 - \frac{u^0+|\mathbf{u}|}{v_{34}}\right) + \mathrm{Li}_2\left(1 - \frac{u^0-|\mathbf{u}|}{v_{34}}\right)\right]_{u=p_4}^{u=\alpha_{34}p_3} \Bigg\} \\ & + \Delta_1(4\Delta E^2) - \frac{1}{2\beta_3}\ln\left(\frac{1-\beta_3}{1+\beta_3}\right) - \frac{1}{2\beta_4}\ln\left(\frac{1-\beta_4}{1+\beta_4}\right), \end{aligned} \tag{5.33}$$

with the abbreviations

$$\beta_j = \sqrt{1 - \frac{m_Q^2}{(p_j^0)^2}}, \quad \beta_{34} = \sqrt{1 - \frac{m_Q^4}{(p_3p_4)^2}}, \quad \alpha_{34} = \sqrt{\frac{1+\beta_{34}}{1-\beta_{34}}}, \quad v_{34} = \frac{m_Q(\alpha_{34}^2-1)}{2(\alpha_{34}p_3^0 - p_4^0)}. \tag{5.34}$$

The integral f_{34} can be obtained from Ref. [89]. The infinitesimal gluon mass m_g used there translates into DR via $\ln(m_g^2) \to (4\pi\mu_{IR}^2)^\varepsilon\Gamma(1+\varepsilon)/\varepsilon$. The integrals in Eq. (C20) and Eq. (25) of Ref. [131] can be used for deriving $f_{aj}(a=1,2;\, j=3,4)$. The remaining f_{12} is easily calculated.

The collinear region is determined by the condition that the angle between the three-momenta of the gluon and a massless parton is smaller than a given cut value. In addition it is required that no overlap between the collinear and the soft region occurs,

$$p_6^0 > \Delta E, \quad 0 < \theta(\mathbf{p}_a,\mathbf{p}_6) < \Delta\theta \ll 1 \quad \text{with} \quad a = 1,2. \tag{5.35}$$

The gluon is the only massless parton in the final state. Hence the collinear part contains only two contributions involving the initial-state partons,

$$\begin{aligned} d\sigma_{\mathrm{coll},a}(p_a) &= \frac{\alpha_s}{2\pi} C_F \int_0^{1-\Delta E/E} dx\, d\sigma_{\mathrm{LO}}(xp_a) \\ &\qquad \times \left\{ \frac{1+x^2}{1-x} \left[-\Delta_1(4E^2) + \ln\left(\frac{\Delta\theta^2}{4}\right) + 2\ln(1-x) \right] + 1 - x \right\} \\ &= \int_0^1 dx\, d\sigma_{\mathrm{LO}}(xp_a)\, V_{a,+}(x) + d\sigma_{\mathrm{LO}}(p_a)\, V_{a,1}, \qquad (5.36) \\ V_{a,+}(x) &= \frac{\alpha_s}{2\pi} \left\{ P^{qq}(x) \left[-\Delta_1(4E^2) + \ln\left(\frac{\Delta\theta^2}{4}\right) \right] \right. \\ &\qquad \left. + C_F \left[2\ln(1-x)\frac{1+x^2}{1-x} + 1 - x \right]_+ \right\}, \qquad (5.37) \\ V_{a,1} &= \frac{\alpha_s}{2\pi} C_F \left\{ \left[-\Delta_1(4E^2) + \ln\left(\frac{\Delta\theta^2}{4}\right) \right] \left[-2\ln\left(\frac{\Delta E}{E}\right) - \frac{3}{2} \right] \right. \\ &\qquad \left. + 4 - 2\ln^2\left(\frac{\Delta E}{E}\right) \right\}. \qquad (5.38) \end{aligned}$$

This result can be obtained by calculating the x and v integrals in Section 5.5 of Ref. [63] by using the ΔE and $\Delta\theta$ cuts.

The integral is split into a convolution containing "+" distributions and a second part with LO kinematics. The divergences of $d\sigma_{\mathrm{soft}}$ and $d\sigma_{\mathrm{coll},1} = d\sigma_{\mathrm{LO}}(V_{a,1} + V_{b,1})$ exactly cancel the IR divergences of the virtual corrections. In addition, the divergence of $V_{a,+}$ is removed by the renormalization of the parton densities. After factorization the term $\Delta_1(4E^2)$ is replaced by $\ln\left(\frac{\mu_F^2}{4E^2}\right)$, as in the case of the subtraction scheme.

5.7 Leading Threshold Logarithms from Soft and Collinear Radiation

The leading threshold logarithms are the terms containing $\ln\beta$ with β defined in Eq. (4.40). They are obtained in the simultaneous limit of reaching the threshold of $Q\bar{Q}H$ production, $(p_3 + p_4 + p_5)^2 \to (2m_Q + M_H)^2$, and of soft gluon radiation, $p_6^0 \to 0$. These leading contributions from the IR regime are connected to the IR divergences. The subtraction function is constructed in such a way that all IR singularities are subtracted from the real corrections. Hence the difference of the real corrections and the subtraction function cannot contribute to the leading threshold logarithms. The sum of virtual corrections and endpoint contribution neither contains any leading threshold logarithms, because all IR divergences are canceled. Therefore, the only source of $\ln\beta$ terms is the readded subtraction function.

The LO matrix elements for both partonic production channels, $gg, q\bar{q} \to Q\bar{Q}H$, tend to a constant at threshold, i.e. for $\beta \to 0$. The PS integration near threshold gives rise to a factor β^4. Hence the LO partonic cross section near threshold behaves as

$$\sigma^{\mathrm{LO}}_{\mathrm{threshold}} \;\sim\; \beta^4 \left|\mathcal{M}^{\mathrm{LO}}\right|^2 = \left(1 - \frac{4\mu_0^2}{\hat{s}}\right)^2 \times \text{const.} \tag{5.39}$$

To extract the leading logarithms, the following integral for the four different $\mathcal{V}$ functions in Eq. (5.20), (5.21), (5.24), and (5.26) is needed,

$$I \;=\; \int_0^1 dx\, \mathcal{V}(x) \otimes \left|\mathcal{M}^{\mathrm{LO}}\right|^2 \left(1 - \frac{4\mu_0^2}{x\hat{s}}\right)^2 \Theta\left(1 - \frac{4\mu_0^2}{x\hat{s}}\right). \tag{5.40}$$

The $\otimes$ sign denotes the colour correlation. The results of the integrals are given by

$$\begin{aligned}
I^{ai,b} &= -\frac{\alpha_s}{2\pi}\, 4\beta^4 \ln(\beta) \left[-\ln\left(\frac{\mu_F^2}{4\mu_0^2}\right) + 2\ln(\beta) - 3\right] (\mathbf{T}_{ai} \cdot \mathbf{T}_b) \otimes \left|\mathcal{M}^{\mathrm{LO}}\right|^2 + \mathcal{O}(\beta^4), \\
I^{ai}_{j} &= -\frac{\alpha_s}{2\pi}\, 4\beta^4 \ln(\beta) \left[-\ln\left(\frac{\mu_F^2}{4\mu_0^2}\right) + 2\ln(\beta) - 3 + \ln(\mu_0^2) - \ln(1+\mu_0^2)\right] \\
&\qquad \times (\mathbf{T}_{ai} \cdot \mathbf{T}_j) \otimes \left|\mathcal{M}^{\mathrm{LO}}\right|^2 + \mathcal{O}(\beta^4), \\
I^{a}_{ji} &= -\frac{\alpha_s}{2\pi}\, 4\beta^4 \ln(\beta) \left[-1 - \ln(\mu_0^2) + \ln(1+\mu_0^2)\right] (\mathbf{T}_a \cdot \mathbf{T}_{ji}) \otimes \left|\mathcal{M}^{\mathrm{LO}}\right|^2 + \mathcal{O}(\beta^4), \\
I_{ji,k} &= \mathcal{O}(\beta^4).
\end{aligned} \tag{5.41}$$

After performing the colour algebra, the sum of all contributions can be written as

$$\begin{aligned}
\sigma_{\log} &= \sigma_{\mathrm{LO}} \otimes \frac{2\alpha_s}{\pi} \Bigg\{ \left(\mathbf{T}_1^2 + \mathbf{T}_2^2\right) \left[2\ln^2\beta - 3\ln\beta - \ln\beta \ln\left(\frac{\mu_F^2}{4\mu_0^2}\right)\right] \\
&\qquad - (\mathbf{T}_3 + \mathbf{T}_4)^2 \ln\beta \Bigg\} \\
&= \sigma_{\mathrm{LO}} \frac{2\alpha_s}{\pi} \left\{ C_{\mathrm{ISR}} \left[2\ln^2\beta - 3\ln\beta - \ln\beta \ln\left(\frac{\mu_F^2}{4\mu_0^2}\right)\right] - C_{\mathrm{FSR}} \ln\beta \right\}.
\end{aligned} \tag{5.42}$$

The actual values for the colour factors depend on the initial state:

$$C_{\mathrm{ISR}}^{q\bar{q}} = +\frac{8}{3}, \quad C_{\mathrm{ISR}}^{gg} = +6. \tag{5.43}$$

The colour algebra in the final-state radiation is more involved. The appearance of two colour amplitudes for the gg channel in LO leads to a dependence of C_{FSR}^{gg} on the ratio m_Q/M_H, analogous to the corresponding colour factor of the Coloumb singularity,

$$C_{\mathrm{FSR}}^{q\bar{q}} = +3, \quad C_{\mathrm{FSR}}^{gg} = \frac{15}{7} \frac{(4m_Q^2 - M_H^2)^2 - \frac{9}{5}M_H^4}{(4m_Q^2 - M_H^2)^2 - \frac{9}{7}M_H^4}. \tag{5.44}$$

Chapter 6

Numerical Results for $t\bar{t}H$ Production

6.1 The NLO Cross Section at the TEVATRON

Figure 6.1 shows the LO and NLO results of the total cross section for $P\bar{P} \to t\bar{t}H + X$ at the TEVATRON as a function of the Higgs mass. Both the renormalization and the factorization scales are set to μ_0 defined in Eq. (3.20), i.e. half the threshold energy. The NLO cross section decreases from 8.5 fb for $M_H = 100\,\text{GeV}$ to 0.3 fb for $M_H = 250\,\text{GeV}$. Over the whole mass range the NLO prediction is smaller than the LO one.

In Fig. 6.2 the renormalization and factorization scale dependence of the cross section for a fixed Higgs mass of 120 GeV is presented. The NLO result is remarkably stable against variations of the scale μ between $\mu_0/3$ and $3\mu_0$, in contrast to the LO prediction. For very small values of μ the NLO cross section becomes negative because large corrections spoil the convergence of perturbation theory.

For the consistent calculation of the K factor,

$$K \;=\; \frac{\sigma_{NLO}}{\sigma_{LO}}, \tag{6.1}$$

the strong coupling constant and the parton densities have to be used at NLO for σ_{NLO} and at LO for σ_{LO}. As can be seen in Fig. 6.1, the K factor is almost constant over the considered Higgs-mass range. The large scale dependence of the LO cross section leads to a similarly large scale dependence for K. The K factor rises from ~ 0.8 at the central scale, $\mu = \mu_0$, to ~ 1 at threshold, $\mu = 2\mu_0$.

The small K factor can be understood qualitatively within the Effective Higgs–Approximation (EHA) [54]. The average partonic CM energy $\langle\sqrt{\hat{s}}\rangle$ for the dominant subprocess $q\bar{q} \to t\bar{t}H$ at the TEVATRON is around 650 GeV. Hence the assumption $M_H^2 \ll m_t^2 \ll$

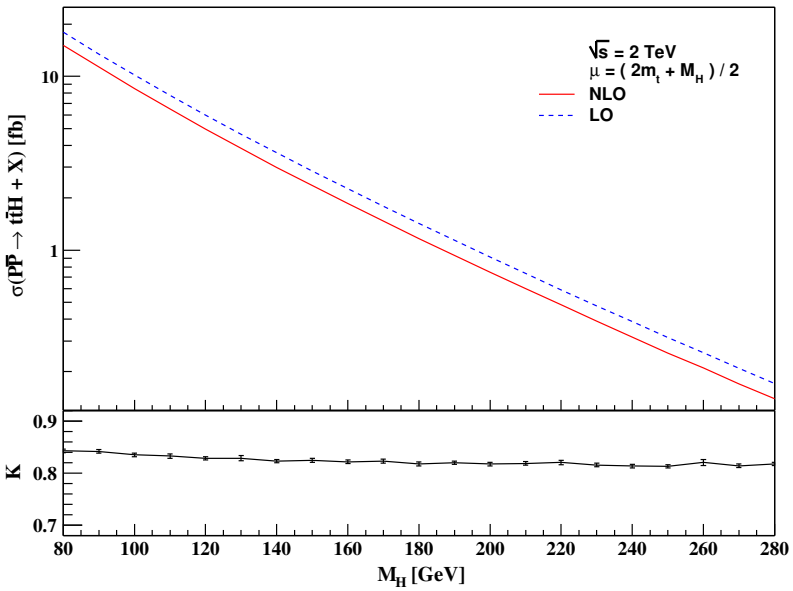

Figure 6.1: The total cross section for $P\bar{P} \to t\bar{t}H + X$ in LO and NLO at the TEVATRON.

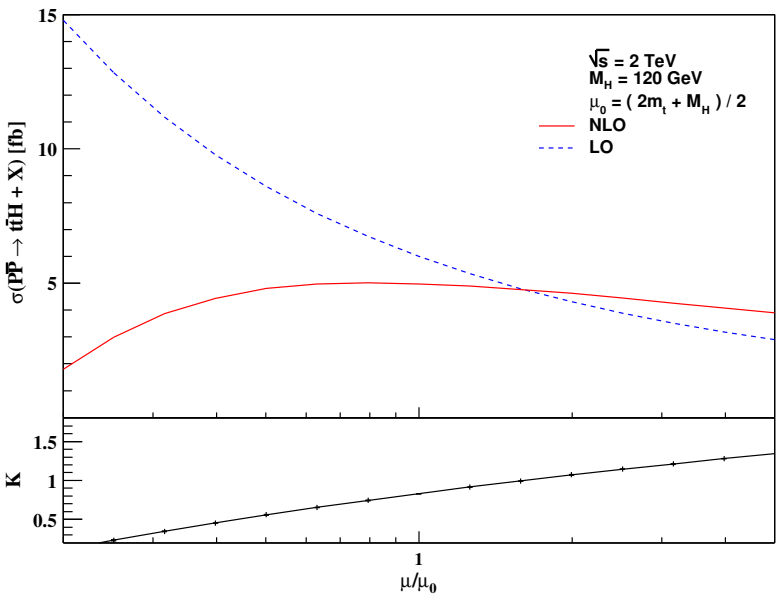

Figure 6.2: The scale dependence of the total cross section for $P\bar{P} \to t\bar{t}H + X$ in LO and NLO at the TEVATRON.

$\Delta\theta$	$\Delta E/E$	LO	Virt.	Coll.	Real	Total
0.1	0.1	4.58 ± 0.01	-3.59 ± 0.02	3.07 ± 0.01	1.41 ± 0.00	5.48 ± 0.03
	0.01	4.58 ± 0.01	-8.40 ± 0.05	3.07 ± 0.01	5.62 ± 0.01	4.88 ± 0.05
	0.001	4.58 ± 0.01	-13.21 ± 0.08	3.07 ± 0.01	10.35 ± 0.01	4.79 ± 0.08
0.01	0.1	4.58 ± 0.01	-6.43 ± 0.04	5.18 ± 0.01	2.68 ± 0.03	6.01 ± 0.05
	0.01	4.58 ± 0.01	-15.46 ± 0.09	5.18 ± 0.01	10.66 ± 0.12	4.96 ± 0.15
	0.001	4.58 ± 0.01	-24.49 ± 0.14	5.18 ± 0.01	19.58 ± 0.19	4.84 ± 0.24
0.001	0.1	4.58 ± 0.01	-9.28 ± 0.05	7.29 ± 0.02	3.22 ± 0.10	5.82 ± 0.11
	0.01	4.58 ± 0.01	-22.54 ± 0.13	7.29 ± 0.02	13.16 ± 0.57	2.49 ± 0.58
	0.001	4.58 ± 0.01	-35.79 ± 0.21	7.29 ± 0.02	24.38 ± 1.82	0.45 ± 1.83
subtraction		4.58 ± 0.01	-1.76 ± 0.01	1.97 ± 0.00	0.07 ± 0.00	4.86 ± 0.01

Table 6.1: The cross section in fb for the process $q\bar{q} \to t\bar{t}H$ at the TEVATRON as a function of the cut parameters used by the PS slicing method. The total NLO result is split into the LO contribution, the virtual corrections, the convolution stemming from the collinear region, and the hard real corrections. For comparison the result obtained by the subtraction method is also quoted. In the corresponding row the number in the column "coll." is the value for the readded subtraction function.

$\langle\sqrt{\hat{s}}\rangle^2$ needed for the approximation is fairly valid. Within the EHA the probability for the hadronic process can be split into the probabilities for $t\bar{t}$ production and subsequent fragmentation $t \to t + H$ or $\bar{t} \to \bar{t} + H$, respectively. Consequently the relative QCD corrections $\delta[P\bar{P} \to q\bar{q} \to t\bar{t}\ ] \sim -\alpha_s/(2\pi)$ [131–134] and $\delta[t \to t + H] = \delta[\bar{t} \to \bar{t} + H] \sim -4\,\alpha_s/\pi$ for small energies of the Higgs boson add to $\delta[P\bar{P} \to q\bar{q} \to t\bar{t} \to t\bar{t}H] \sim -9\,\alpha_s/(2\pi)$. Since $\delta[P\bar{P} \to q\bar{q} \to t\bar{t} \to t\bar{t}H]$ is negative, the K factor is expected to be below unity. The integration over the entire Higgs spectrum yields $K_{\mathrm{EHA}} \sim 0.7$ [55] which is qualitatively comparable with $K \sim 0.8$ resulting from the full NLO QCD calculation.

As mentioned in Chapter 5, the PS slicing method has been worked out as an independent check for the process $q\bar{q} \to Q\bar{Q}H$. The numerical results are shown in Table 6.1. For comparison, the cross section obtained by the subtraction method is also quoted. Within each column the same integration statistics has been used for all rows. The total result is split into the LO cross section, the virtual corrections, the convolution stemming from the collinear region, and the hard real corrections. The virtual corrections include the contributions from the soft region (see Eq. (5.29)) and the "endpoint" contribution of the collinear region as given in Eq. (5.38). The results in the column "coll." are obtained from Eq. (5.37). In the case of the subtraction method the virtual corrections include the complete endpoint contribution as given in Section 4.4. The result presented in the column "coll." is obtained from the convolution of the readded subtraction function as explained in Section 5.5. The quoted value in the column "real" is the difference of the real corrections and the subtraction function.

Both cut values for $\Delta\theta$ and $\Delta E/E$ have been varied from 10^{-1} to 10^{-3}. To obtain the cross

section within the PS slicing method one has to search for a plateau in the dependence on the cut values. Since in this work the slicing method only serves as a check this tedious study has not been performed, but would be necessary without the use of the subtraction method. In the region of $\Delta\theta$ and $\Delta E/E$ between 10^{-1} and 10^{-2} the results agree with each other within the statistical errors and particularly are compatible with the result from the subtraction method. Nevertheless, the latter has a considerable smaller error than the former, when the same number of points for the MC integration is used. As can be seen in Table 6.1, within the PS slicing method large cancellations take place between the virtual and the real corrections that are absent in the subtraction method. Hence, for obtaining a result by slicing, that is competitive with the one obtained by subtraction, large contributions have to be evaluated with smaller *relative* errors. This is only possible with a higher amount of integration statistics. Since the subtraction method turns out to provide a more reliable numerical result, no further attempts have been performed to adopt the PS slicing method for the process $gg \to Q\bar{Q}H$.

6.2 The NLO Cross Section at the LHC

The LO and NLO predictions for the process $PP \to t\bar{t}H + X$ at the LHC are plotted in Fig. 6.3 as a function of the Higgs mass. Again the central scales μ_0 is chosen for the renormalization and the factorization scales. The NLO cross section decreases from 1.1 pb for $M_H = 100\,\text{GeV}$ to 80fb for a Higgs mass of 250 GeV. Over the whole plotted range of the Higgs mass the NLO prediction is larger than the LO one. In analogy to the TEVATRON, the K factor is almost independent of the Higgs mass and amounts to ~ 1.2 at the central scale μ_0.

At the LHC the average partonic energy is $\langle\sqrt{\hat{s}}\rangle \sim 830$ GeV. Since the relative QCD corrections to the dominant $t\bar{t}$ production channel $gg \to t\bar{t}$ are positive, $\delta[gg \to t\bar{t}\,] \sim 11\,\alpha_s/\pi$, and overcompensate the negative corrections to the fragmentation, $\delta[t \to t + H] \sim -4\,\alpha_s/\pi$, the total relative QCD corrections, estimated in the EHA, are positive, $\delta[PP \to gg \to t\bar{t} \to t\bar{t}H] \sim 7\,\alpha_s/\pi$. The estimated K factor in Ref. [54] can be considered to be qualitatively comparable with the full NLO result, if the different renormalization and factorization scales are taken into account.

The variation of the LO and NLO cross section with the renormalization and the factorization scales for a fixed Higgs mass of 120 GeV is shown in Fig. 6.4. The improvement of the NLO calculation is as significant as for the TEVATRON. The scale dependence is drastically reduced in NLO. The K factor increases from ~ 1.2 at $\mu = \mu_0$ to ~ 1.4 at threshold, $\mu = 2\mu_0$.

The individual partonic contributions to the total cross section, depending on the scale, are shown in Fig. 6.5. The gg channel contributes much more than the $q\bar{q}$ channel over the whole considered μ range. While the former has a maximum slightly below the central scale, the latter rises with increasing μ. The $qg/\bar{q}g$ channel, which is absent at LO, is small

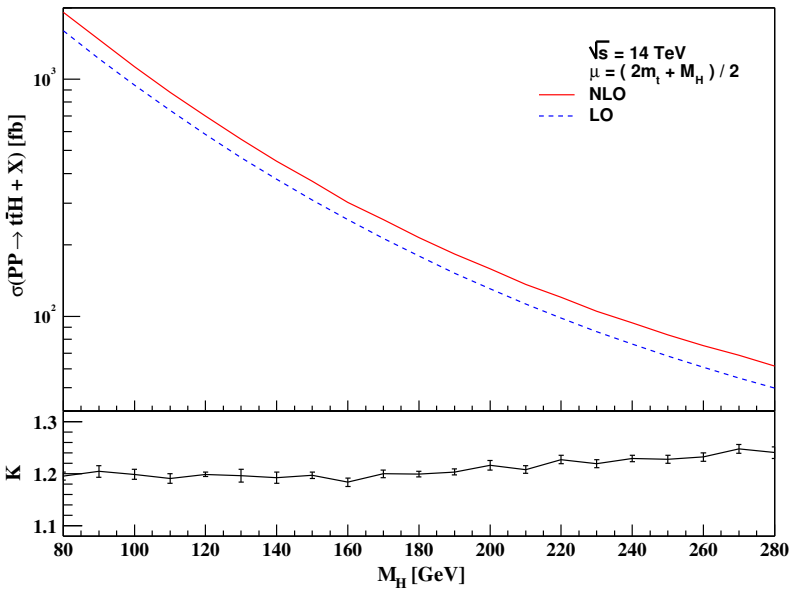

Figure 6.3: The total cross section for $PP \to t\bar{t}H + X$ in LO and NLO at the LHC.

and negative for μ above the central scale but increases strongly when going to smaller values of μ. Note that the parton densities do not have a strict probabilistic interpretation at NLO. Hence negative partonic contributions are not in contradiction with the parton model. They are caused by absorbing contributions into the parton densities. Although each contribution shows a relatively strong μ dependence, their total sum is remarkably stable. This indicates that for a proper study of the scale dependence all partonic processes have to be considered.

The shape of the curves in Fig. 6.5 can be understood better when separating the effects of varying the renormalization and factorization scales. When fixing the renormalization scale to half the threshold energy, the contribution of the gg and the $q\bar{q}$ channel increase with increasing factorization scale. In contrast, the contribution from $qg/\bar{q}g \to t\bar{t}H$ decrease and become negative slightly above μ_0. For a fixed factorization scale of $\mu_F = \mu_0$, the gg and the $q\bar{q}$ channel show the typical renormalization scale dependence in NLO. They peak at a scale roughly of the order of μ_0, become negative for very small values of μ_R and tend to zero for large values of μ_R. The $qg/\bar{q}g$ channels are LO processes and hence show the typical strong LO renormalization scale dependence, i.e. their cross section decreases strongly with increasing μ_R. When varying the renormalization and the factorization scale at the same time, both effects enhance each other and result in the behaviour shown in Fig. 6.5.

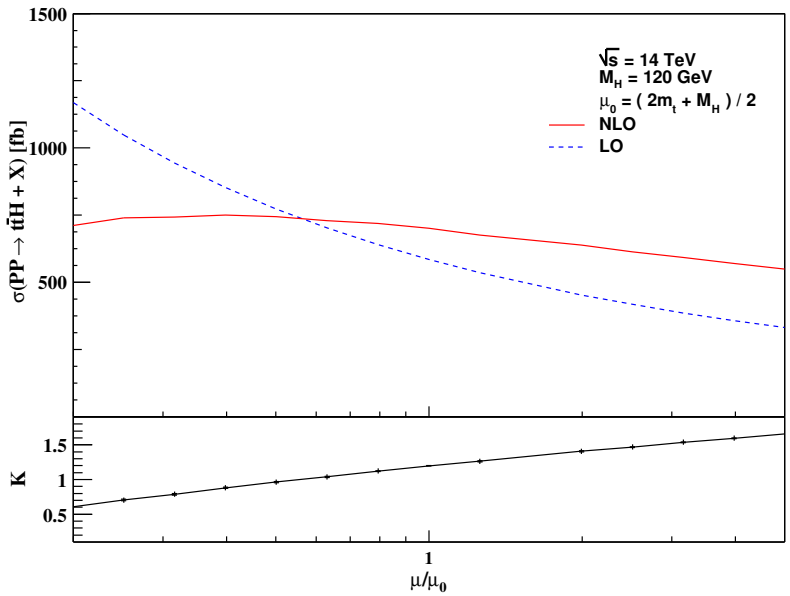

Figure 6.4: The scale dependence of the total cross section for $PP \to t\bar{t}H + X$ in LO and NLO at the LHC.

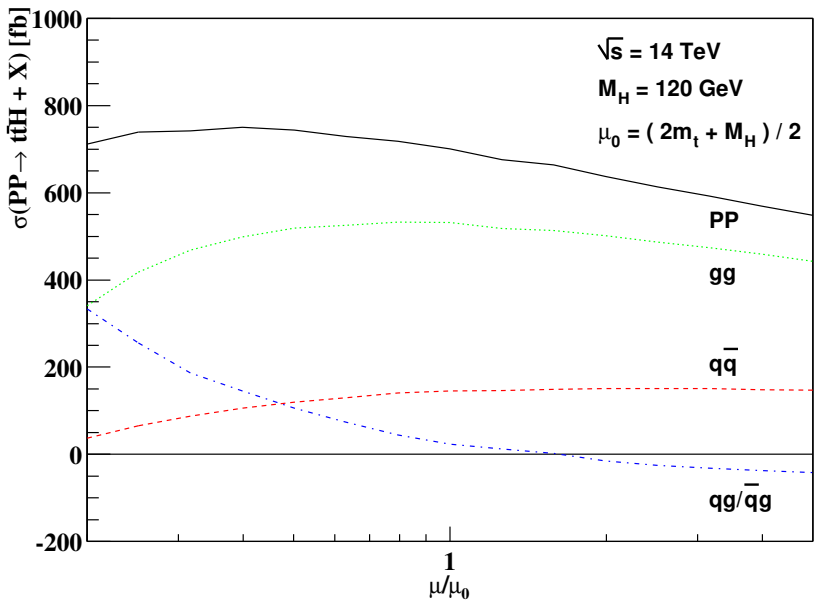

Figure 6.5: The scale dependence of the total cross section for $PP \to t\bar{t}H + X$ in NLO at the LHC for each channel separately.

6.3 Distributions

Distributions are frequently used in data analysis. They help to localize the dominant contribution to the background rates and to deduce the values of the cuts that are used in order to suppress the number of background events and to increase the signal-to-background ratio. Therefore they are of high interest. In hadron–hadron collisions the partonic Center-of-Mass System (CMS) is in general boosted along the beam pipe with respect to the hadronic CMS that coincides with the laboratory system. Hence boost-invariant quantities are strongly preferred. The transverse momentum p_T is a commonly used boost-invariant quantity. In this section various distributions in the transverse momentum of different particles for the processes $P\bar{P}/PP \to t\bar{t}H + X$ in LO as well as in NLO are presented. Throughout this section the Higgs mass is chosen to be 120 GeV and the renormalization and the factorization scales are set to μ_0.

Technically there are two different possibilities to generate distributions in predictions. First of all, one can reparametrize the PS in such a way that the variable of interest is one of the n involved integration variables. By leaving this variable fixed, an integration over $(n-1)$ dimensions is left. To obtain the differential cross section, one has to vary the variable of interest and perform an $(n-1)$ dimensional integration for each value. Another method when using MC integration is to stick to the full n dimensional integration and to fill a histogram. The numerical range of the variable of interest is divided into bins. For each MC point, the variable of interest is calculated and the result of the matrix element is added to the corresponding bin. The number of points used for the MC integration must be large enough so that a sufficient number of events contributes to each bin in order to get a reliable result. This procedure is more flexible and can be used even in cases in which the other procedure is not applicable, e.g., for distributions in the transverse momentum of jets defined by jet algorithms. Another advantage is that many distributions can be produced with one integration. Hence this latter method was implemented in the C++ program. The bin width for the transverse momentum is chosen to 1 GeV. The LO results are smooth enough to be represented by a line. In contrast, the NLO predictions have much larger statistical fluctuations and several bins had to be combined.

The left side of Fig. 6.6 shows the differential cross section with respect to the transverse momentum of the Higgs particle at the TEVATRON. The dashed line is the LO result and the NLO prediction is represented by the histogram. For small values of p_T the NLO result lies slightly below the LO one. The difference becomes more sizable for higher values of p_T. This can be seen better on the right side of Fig. 6.6 where the ratio of the NLO distribution over the LO one is plotted. The decrease of the ratio for higher values of p_T is visible.

A first approximation for NLO distributions is to rescale the LO distribution with the K factor obtained from the total cross section. The validity of this approximation can be read off from the right side of Fig. 6.6. The dashed horizontal line is drawn at the value of the K factor of 0.83. While for low p_T the approximation is in good shape, it

overestimates the differential cross section for $p_T > 200\,\text{GeV}$. Since for such values of the transverse momentum the cross section is rather small, the experimental analysis is supposed not to be affected.

The heavy quark and the heavy anti-quark in the final state can only be distinguished experimentally in special decay channels. Hence the differential cross section with respect to the transverse momentum of one of them is very hard to measure. Instead the two transverse momenta are combined somehow. The left side of Fig. 6.7 shows the distribution with respect to the smaller of the two p_T at the TEVATRON. Again, the LO prediction is represented by the dashed line and the NLO one by the histogram. The ratio of the two is plotted on the right side of Fig. 6.7. For $p_T \lesssim 150\,\text{GeV}$ the approximation of rescaling the LO distribution with the K factor is applicable. Above this value it overestimates the full NLO result. Consequences for the experimental analysis are not expected because the cross section for $p_T \gtrsim 150\,\text{GeV}$ is small.

Figure 6.8 shows the distribution when the larger of the two p_T is chosen. It peaks at a higher p_T value than the previous distribution. Nevertheless, the statements about the approximation apply here, too. The LO distribution times the K factor starts overestimating the full NLO result for $p_T > 200\,\text{GeV}$. Again, the cross section drops rapidly in this region and hence the rescaling approximation is considered to work for an experimental analysis.

The distribution in the transverse momentum of the Higgs particle at the LHC is shown on the left side of Fig. 6.9. The NLO results for the distribution are larger than the LO predictions, in agreement with the increase of the total cross section by the NLO corrections. Due to the higher beam energy at the LHC, higher values of p_T than at the TEVATRON are reached. The ratio of the NLO over the LO distribution is plotted on the right side of Fig. 6.9. At the LHC the K factor is 1.20 for $M_H = 120\,\text{GeV}$ and both scales set to the central scale μ_0. This is indicated by the dashed horizontal line. The ratio of the two distributions agrees with the K factor up to $p_T \approx 450\,\text{GeV}$. Above this value the full NLO result lies below the approximation. However, the cross section in this region is almost two orders of magnitude smaller than in the peak. Therefore, multiplying the LO distribution with the K factor should work as a good approximation for an experimental analysis.

The left side of Fig. 6.10 shows the distribution with respect to the smaller of the two p_T of the top quarks. The NLO predictions lie above the LO result for low values of p_T and below for $p_T \gtrsim 350\,\text{GeV}$. This is remarkable since the K factor is larger than one. As can be seen on the right side of Fig. 6.10, the approximation of rescaling the LO distribution with the K factor underestimates the full NLO result in the peak and overestimates it drastically in the tail. Hence, for exploiting this distribution in an experimental analysis the rescaling approximation is inappropriate and the full NLO prediction should be used.

The distribution with respect to the larger of the two p_T is plotted in Fig. 6.11. The ratio of the NLO over the LO distribution is larger than the K factor for very small values of p_T, agrees well with it up to 350 GeV, and is smaller than the K factor for $p_T \gtrsim 350\,\text{GeV}$.

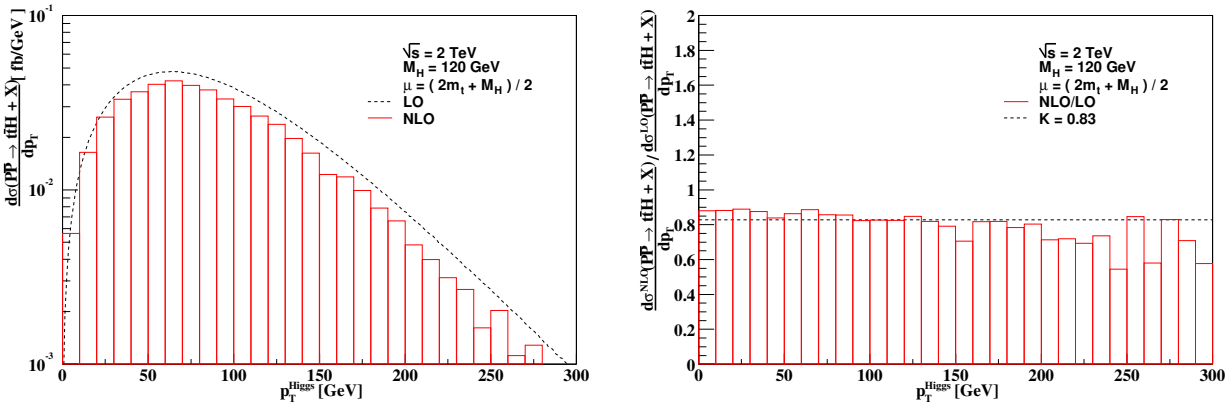

Figure 6.6: Left: The p_T distribution of the Higgs boson in the process $P\bar{P} \to t\bar{t}H + X$ at the TEVATRON. Right: The ratio of the NLO and the LO p_T distribution of the Higgs boson in the process $P\bar{P} \to t\bar{t}H + X$ at the TEVATRON. The dashed horizontal line is the K factor of 0.83 for $M_H = 120\,\text{GeV}$ and the renormalization and factorization scales set to μ_0.

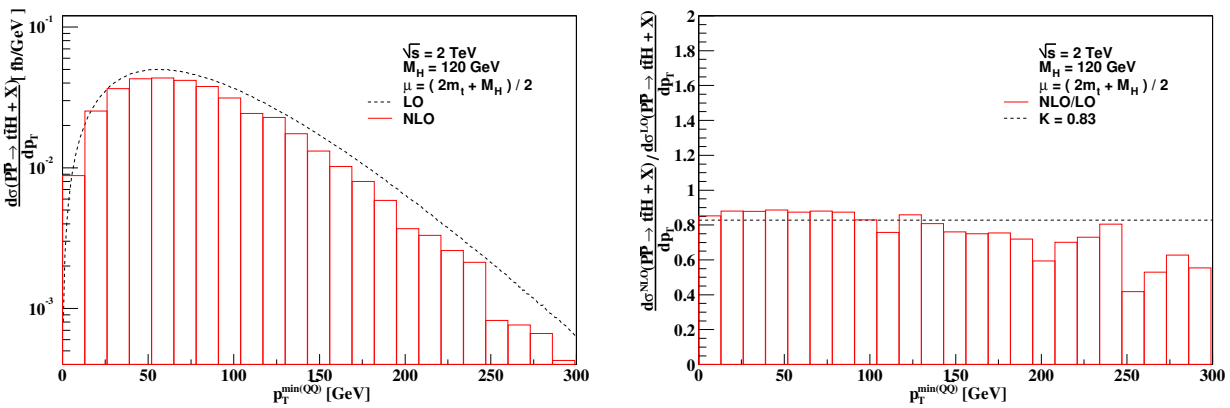

Figure 6.7: Left: The distribution with respect to the smaller p_T value of the two top quarks in the process $P\bar{P} \to t\bar{t}H + X$ at the TEVATRON. Right: The ratio of the NLO and the LO p_T distribution with respect to the smaller p_T value of the two top quarks in the process $P\bar{P} \to t\bar{t}H + X$ at the TEVATRON. The dashed horizontal line is the K factor of 0.83 for $M_H = 120\,\text{GeV}$ and the renormalization and factorization scales set to μ_0.

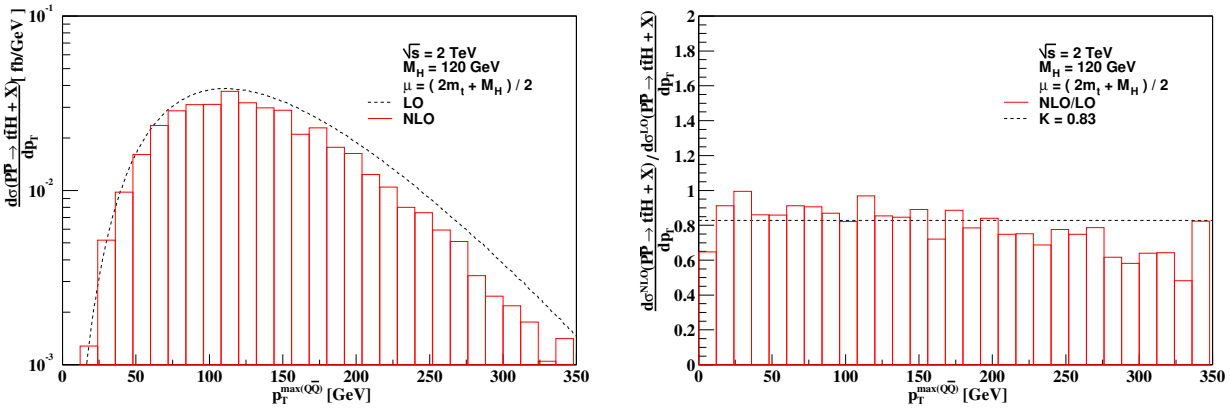

Figure 6.8: Left: The distribution with respect to the larger p_T value of the two top quarks in the process $P\bar{P} \to t\bar{t}H + X$ at the TEVATRON. Right: The ratio of the NLO and the LO p_T distribution with respect to the larger p_T value of the two top quarks in the process $P\bar{P} \to t\bar{t}H + X$ at the TEVATRON. The dashed horizontal line is the K factor of 0.83 for $M_H = 120\,\text{GeV}$ and the renormalization and factorization scales set to μ_0.

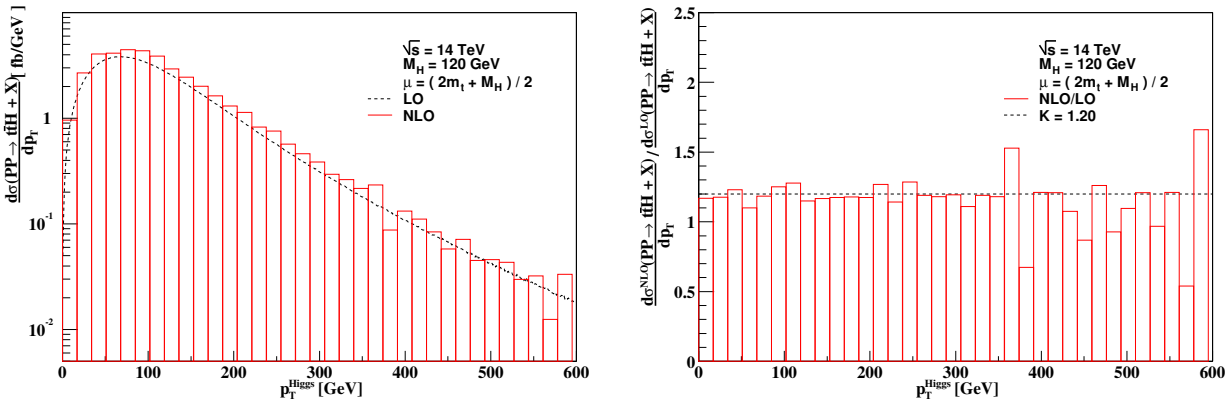

Figure 6.9: Left: The p_T distribution of the Higgs boson in the process $PP \to t\bar{t}H + X$ at the LHC. Right: The ratio of the NLO and the LO p_T distribution of the Higgs boson in the process $PP \to t\bar{t}H + X$ at the LHC. The dashed horizontal line is the K factor of 1.20 for $M_H = 120\,\text{GeV}$ and the renormalization and factorization scales set to μ_0.

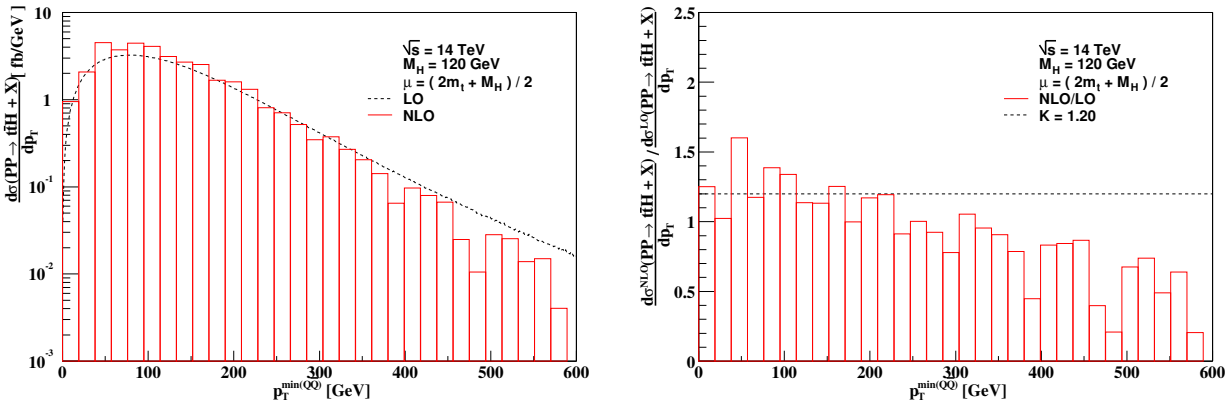

Figure 6.10: Left: The distribution with respect to the smaller p_T value of the two top quarks in the process $PP \to t\bar{t}H + X$ at the LHC. Right: The ratio of the NLO and the LO p_T distribution with respect to the smaller p_T value of the two top quarks in the process $PP \to t\bar{t}H + X$ at the LHC. The dashed horizontal line is the K factor of 1.20 for $M_H = 120\,\text{GeV}$ and the renormalization and factorization scales set to μ_0.

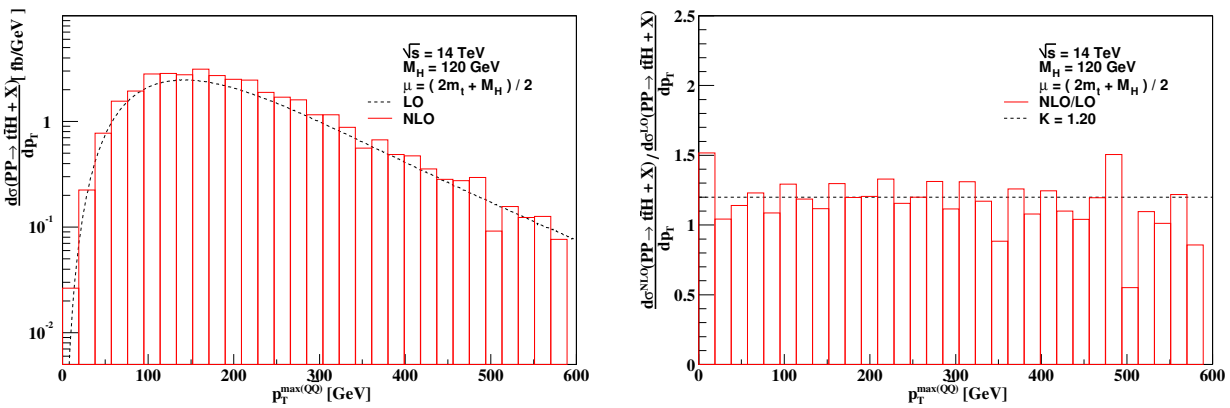

Figure 6.11: Left: The distribution with respect to the larger p_T value of the two top quarks in the process $PP \to t\bar{t}H + X$ at the LHC. Right: The ratio of the NLO and the LO p_T distribution with respect to the larger p_T value of the two top quarks in the process $PP \to t\bar{t}H + X$ at the LHC. The dashed horizontal line is the K factor of 1.20 for $M_H = 120\,\text{GeV}$ and the renormalization and factorization scales set to μ_0.

Since the cross section in the last region is still sizeable, it depends on the quality of the measurement whether the full NLO result must be used or the rescaling approximation is sufficient.

6.4 Leading Threshold Corrections

In Sections 4.6 and 5.7 the Coulomb singularity and the leading threshold logarithms have been extracted. In this section the numerical results for these leading threshold corrections are presented. The left side of Fig. 6.12 shows the relative deviation of the Leading Threshold Approximation (LTA) from the full NLO result at the TEVATRON as a function of the Higgs mass. The renormalization and factorization scales are chosen as the central scale μ_0. The channels $q\bar{q} \to t\bar{t}H$ (solid line) and $gg \to t\bar{t}H$ (dashed line) are plotted separately. The error bars indicate the statistical errors from the MC integration. In the $q\bar{q}$ channel the LTA overestimates the full NLO result by about 10% over the whole plotted Higgs-mass range. In contrast, the LTA underestimates the full NLO prediction in the gg channel. This difference is roughly 5% for low values of the Higgs mass and rises strongly with increasing M_H. The quality of the LTA is similarly low at the LHC, as can be seen on the right side of Fig. 6.12. The cross section for the $q\bar{q}$ channel is overestimated by $20\% - 30\%$. For the gg channel the prediction of the LTA lies slightly above the full NLO result for light Higgs masses and below for $M_H > 150\,\text{GeV}$. The discrepancy grows strongly with increasing Higgs mass.

The leading threshold corrections are, therefore, not a good approximation for the full NLO calculation. This is not due to a "wrong" choice of the renormalization and factorization scales. The scale dependence of the LTA for a fixed Higgs mass of 120 GeV at the TEVATRON and at the LHC is plotted in Fig. 6.13. One can observe that the LTA has a much stronger scale dependence than the full NLO result. This reflects the fact that within in LTA the dependence on the renormalization scale is not reduced at all with respect to the LO approximation. This can be seen from the formulae in Section 4.6 and 5.7. Only the factorization scale appears in Eq. (5.42). Hence the LTA is less dependent on the factorization scale than the LO cross section. Nevertheless, there is no preferred scale, at which the LTA works sufficiently well for both production channels.

The failure of the leading threshold corrections to describe the full NLO result is caused by the relatively high average partonic CM energy. For $M_H = 120\,\text{GeV}$ the average partonic CM energy $\langle\sqrt{\hat{s}}\rangle$ is $\sim 650\,\text{GeV}$ at the TEVATRON and $\sim 830\,\text{GeV}$ at the LHC and hence lies sufficiently above the threshold. Even for the largest considered Higgs mass of 280 GeV the partonic CM energy is not close enough to the threshold to see the leading threshold effects.

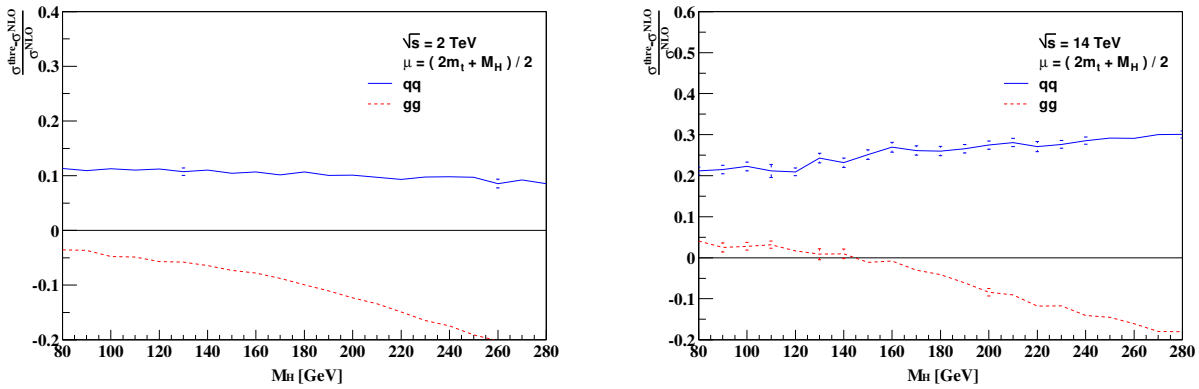

Figure 6.12: The relative deviation of the leading threshold corrections from the full NLO result for $P\bar{P}/PP \to t\bar{t}H + X$ at the TEVATRON (left) and the LHC (right) for the different partonic cross sections. The error bars are the statistical errors from the MC integration.

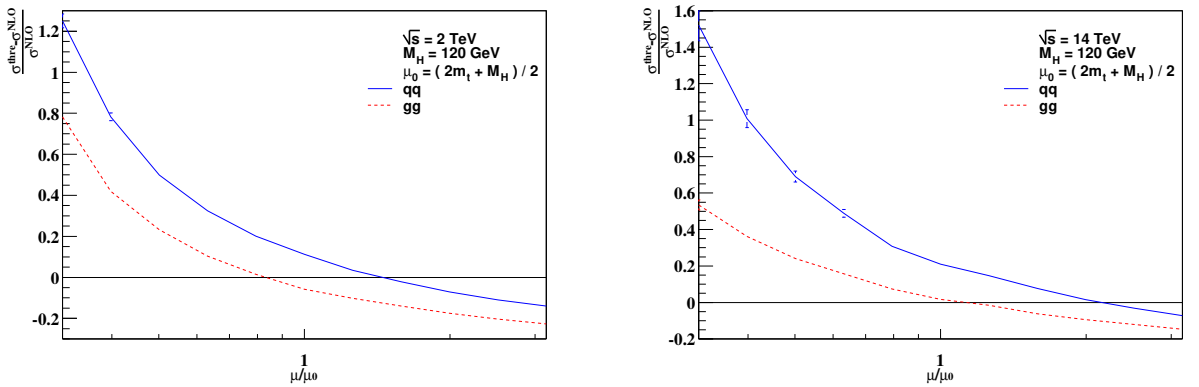

Figure 6.13: The renormalization and the factorization scale dependence of the relative deviation of the leading threshold corrections from the full NLO result for $P\bar{P}/PP \to t\bar{t}H + X$ for a Higgs mass of 120 GeV at the TEVATRON (left) and the LHC (right) for the different partonic cross sections. The error bars are the statistical errors from the MC integration.

Chapter 7

Outlook to $b\bar{b}H$ Production

7.1 Discussion of Large Logarithmic Corrections

The starting point [135, 136] is the process $gg \to Q\bar{Q}H$ for a heavy quark that is much lighter than the Higgs boson, as in the case of the bottom quark. In the diagrams with t-channel exchange (s. Fig. 3.1) at least one gluon splits into a pair of heavy quarks with one of them on-shell. When this pair is nearly collinear, the propagator of the internal heavy quark is nearly on-shell and enhances the amplitude. The integration over the PS of the external quarks yields a factor $\ln(q^2/m_Q^2)$ where the typical scale q^2 is of the order of the Higgs mass, $q^2 \sim M_H^2$. Hence for this process the splitting of a gluon into a heavy quark pair introduces a contribution of order $\alpha_s \ln(q^2/m_Q^2)$. Since the large logarithm enhances the expansion parameter of perturbation theory, the convergence of the expansion is degraded. It can be improved by summing these collinear logarithms to all orders in perturbation theory [137, 138]. This can be done by introducing a heavy-quark distribution function $Q(x, \mu_F)$ which is intrinsically of order $\alpha_s \ln(\mu_F^2/m_Q^2)$. The physical picture is that the hard process is affected by the splitting only through the reduced energy, but does not "feel" the second heavy quark stemming from the splitting. This leads to the factorization of the splitting from the rest of the process. Whether these logarithms dominate the cross section or not, depends on the energy of the collider. They do not at the TEVATRON [139], but it is yet not clear if the energy at the LHC is high enough for observing such a dominance.

The introduction of a heavy-quark distribution function changes the way perturbation theory is ordered. Due to the appearance of $Q(x, \mu_F)$ the leading order process is heavy-quark fusion into Higgs, $Q\bar{Q} \to H$ (s. Fig. 7.1(i)). The heavy-quark distribution function appears twice and hence this process is of order $\alpha_s^2 \ln^2(\mu_F^2/m_Q^2)$. Consider now the processes $gQ \to QH$ and $g\bar{Q} \to \bar{Q}H$ (s. Fig. 7.1(ii)), which belong to the real corrections to $Q\bar{Q} \to H$. Parts of the collinear logarithms obtained from these corrections have already been resummed in the heavy-quark distribution function. This leads to a potential double counting which can be avoided by applying the procedure proposed in Ref. [136]. After

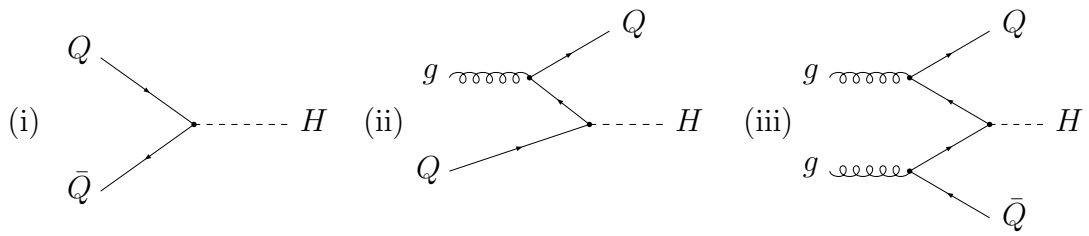

Figure 7.1: The LO processes for the different numbers of heavy quarks in the final state after introducing a heavy-quark distribution function. Note that for (ii) and (iii) additional diagrams not shown here exist.

the subtraction of the contributions resummed in the heavy-quark distribution function the processes of Fig. 7.1(ii) are of order $\alpha_s^2 \ln(\mu_F^2/m_Q^2)$ and hence a correction of order $1/\ln(\mu_F^2/m_Q^2)$ to heavy-quark fusion into Higgs. However, if a tagged heavy quark, besides the Higgs boson, is required heavy-quark fusion into Higgs cannot contribute to the corresponding cross section. The LO processes in this case are rather $gQ \to QH$ and $g\bar{Q} \to \bar{Q}H$.

Now consider the process $gg \to Q\bar{Q}H$ (s. Fig. 7.1(iii)). In analogy to the previous discussion it provides corrections of the order $1/\ln(\mu_F^2/m_Q^2)$ to the processes depicted in Fig. 7.1(ii) and corrections of order $1/\ln^2(\mu_F^2/m_Q^2)$ to heavy-quark fusion into Higgs. In the case of two tagged heavy quarks in the final state it is the LO process besides $q\bar{q} \to Q\bar{Q}H$.

Experimentally a tagged quark requires a finite transverse momentum larger than $p_{T,\min}$. If each heavy quark is requested to have a transverse momentum above this cut value, the complications caused by the large logarithms $\ln(q^2/p_{T,\min}^2)$ does not appear. The LO processes are $gg, q\bar{q} \to Q\bar{Q}H$. Hence the calculation of the cross section for these processes including NLO QCD corrections can directly be applied to $b\bar{b}H$ production after introducing a cut on the transverse momentum of the heavy quarks in the final state. This is done in the rest of this chapter. For each bottom quark a transverse momentum larger than 20 GeV is required. The mass of the bottom quark is set to 4.5 GeV. No running bottom mass is introduced and hence the running is described by the $\mathcal{O}(\alpha_s)$ radiative corrections.

7.2 $b\bar{b}H$ Production at the TEVATRON

Figure 7.2 shows the LO and the NLO prediction for the cross section as a function of the Higgs mass for $b\bar{b}H$ production at the TEVATRON with a required minimal p_T of 20 GeV for each b quark. The error bars are the statistical errors from the MC integration. The NLO cross section decreases from 0.4 fb for $M_H = 100$ GeV to 0.01 fb for $M_H = 250$ GeV. For low values of M_H the NLO corrections decrease the cross section, while they lead to an increase for higher Higgs masses.

As can be seen in Fig. 7.3, the reduction of the scale dependence due to the inclusion of the NLO corrections is similarly striking for $b\bar{b}H$ production as for $t\bar{t}H$ production. While the LO prediction varies at least within a factor of two, the fluctuation of the NLO prediction changes only within 25% for a scale variation between $\mu_0/2$ and $2\mu_0$. Since the central scale μ_0 is already quite low, the factorization and renormalization scale is only varied between $\mu_0/4$ and $4\mu_0$ in order to avoid unphysically small scales. Already at the lower end of the plotted μ range, perturbation theory is spoiled by large corrections, as can be seen by the negative cross section.

The cross section for the process $P\bar{P} \to b\bar{b}H + X$ is rather small in the SM. As mentioned in the introduction, this process is of more interest in supersymmetric models. For the MSSM an approximation of the cross sections for $b\bar{b}\phi$ production, where ϕ denotes one of the two CP-even Higgs particles h and H, can be obtained from the results presented here by a simple rescaling,

$$\sigma^{\mathrm{MSSM}} = \left[\frac{g^{\mathrm{MSSM}}_{b\bar{b}\phi}}{g^{\mathrm{SM}}_{b\bar{b}H}}\right]^2 \sigma^{\mathrm{SM}}, \tag{7.1}$$

where $g_{b\bar{b}\phi}$ is the coupling of the $b\bar{b}\phi$ vertex in the corresponding model. The strict validity of the relation is disturbed by the appearance of closed top-quark loops radiating a Higgs (s. Fig. 4.1(ii)), since the ratio of the $t\bar{t}\phi$ and the $b\bar{b}\phi$ coupling is different in the SM and the MSSM. These loops interfere destructively with the LO diagrams. The reduction is roughly one per cent at the TEVATRON and hence small enough to be neglected.

In the parameter region of the MSSM where $\tan\beta$ is large the tree-level relation between the Yukawa coupling of the bottom quark and its mass can receive large radiative corrections [47]. As a consequence, the corrections to $b\bar{b}H$ production are also large. This may cause problems for the reliability of the perturbative description of the process.

7.3 $b\bar{b}H$ Production at the LHC

The cross section for $PP \to b\bar{b}H + X$ at the LHC is plotted in Fig. 7.4. Again, for each b quark a p_T larger than 20 GeV is required. The cross section decreases from 60 fb for a Higgs mass of 100 GeV to 6 fb for $M_H = 250$ GeV. Over the whole plotted mass range the NLO prediction is smaller than the LO one.

To obtain the cross section within the MSSM, the SM prediction can be rescaled as done in Eq. (7.1). However, the impact of the closed top-quark loops radiating a Higgs boson is larger at the LHC than at the TEVATRON. For $M_H = 120$ GeV, both scales set to half the threshold energy, and $p_T > 20$ GeV required for each bottom quark, these loops reduce the cross section by ~ 5 fb to ~ 40 fb. When $\tan\beta$ is large, the $b\bar{b}H$ coupling is enhanced and the $t\bar{t}H$ coupling is reduced. Hence the impact of the closed top-quark loops radiating

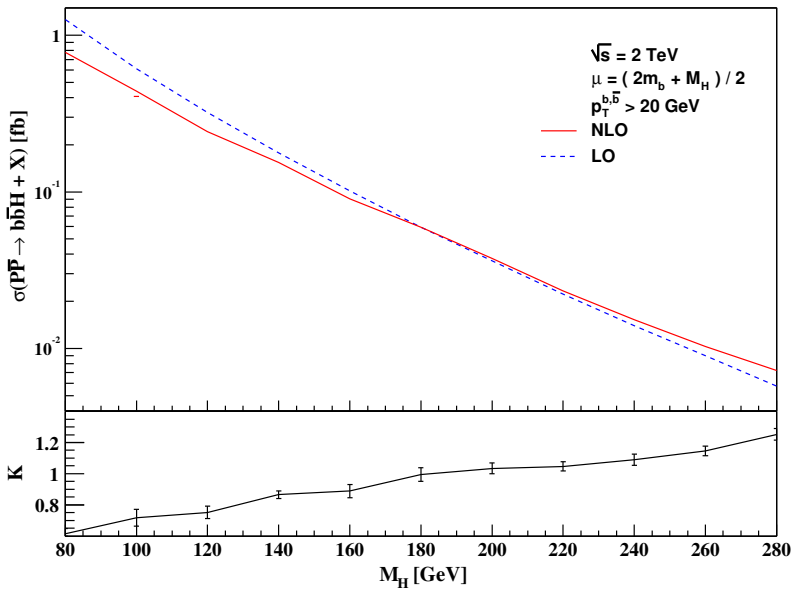

Figure 7.2: The total cross section for $P\bar{P} \to b\bar{b}H + X$ in LO and NLO at the TEVATRON requiring a $p_T > 20\,\mathrm{GeV}$ for each quark. The error bars are the statistical errors from the MC integration.

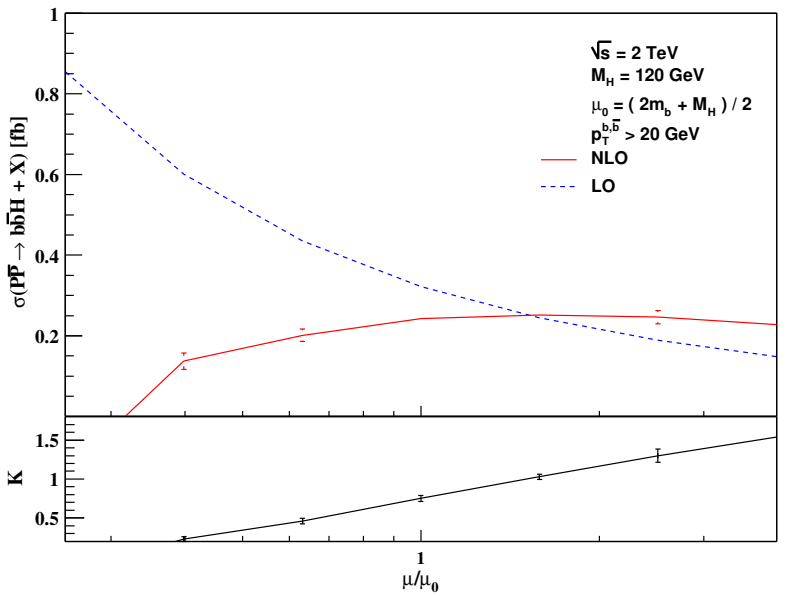

Figure 7.3: The scale dependence of the total cross section for $P\bar{P} \to b\bar{b}H + X$ in LO and NLO at the TEVATRON requiring a $p_T > 20\,\mathrm{GeV}$ for each quark. The error bars are the statistical errors from the MC integration.

a Higgs boson decreases in the MSSM. As a consequence, the approximation in Eq. (7.1) tends to underestimate the cross section for the MSSM.

The NLO QCD corrections stabilize the prediction with respect to the renormalization and factorization scales compared to the LO approximation (see Fig. 7.5). While the LO cross section drops from 80 fb to 45 fb for μ between $\mu_0/2$ and $2\mu_0$, the NLO prediction varies within 15% in the same μ range.

The presented predictions for the cross section of $b\bar{b}H$ production at the LHC are plagued by relatively large errors of order 10% coming from the MC integration. Although the integration statistics has been increased by a factor between 5 and 25 compared to $t\bar{t}H$ production, the relative errors are one order of magnitude larger. This is caused by the appearance of two widely separated scales, the b mass and the Higgs mass. The MC integration routine used in the C++ code is an implementation of the VEGAS [140] algorithm. It is an adaptive algorithm which tries to optimize the grid for generating random points with respect to the integrand. However, this optimization can only be performed in each dimension separately. Hence, if a sharp rise like a p_T cut is not parameterized by one integration variable, VEGAS is not able to cope with this case properly. Even when neglecting the limited computer time, a sole increase of the number of points does not necessarily reduce the errors as much as wanted. The adaptiveness of the algorithm can turn into a disadvantage, since the integrand is too complex for VEGAS and it optimizes the grid in an inappropriate way.

The highest statistics, used here for $b\bar{b}H$ production, requires a computer time of roughly two days on a 1 GHz processor for calculating the cross section for one parameter set-up. Hence, no further increase of the number of points is considered. One possible way to improve the efficiency of the implemented MC integration is to optimize the PS parameterization in such a way that the peaks of the integrand depend only on one of the integration dimensions. Since there are much more peaks than integration dimensions, this optimization procedure is limited. A considerable improvement can be obtained by implementing a multi-channel Monte Carlo method [141–144]. This method employs several PS parameterizations simultaneously. Hence it is able to smoothen more peaks than VEGAS. It can be further improved by using an adaptive optimization method concerning the contribution of the different channels.

If one wants to compare the result of the full $2 \to 3$ process with the result obtained by resuming the potentially large logarithms into a heavy-quark distribution function, it is not possible to require two tagged b quarks. Hence the p_T cut has to be dropped for at least one of the two heavy quarks. However, weakening the p_T cuts for the b quarks increases the requirements on the numerical stability of the MC integration strongly. Hence, before employing the NLO cross section for $P\bar{P}/PP \to Q\bar{Q}H$ for this special case, the numerical problems described above have to be solved.

Another improvement of the calculation is provided by the introduction of a running bottom mass $\overline{m}_b(\mu)$. As a consequence, the LO prediction is strongly reduced by the factor

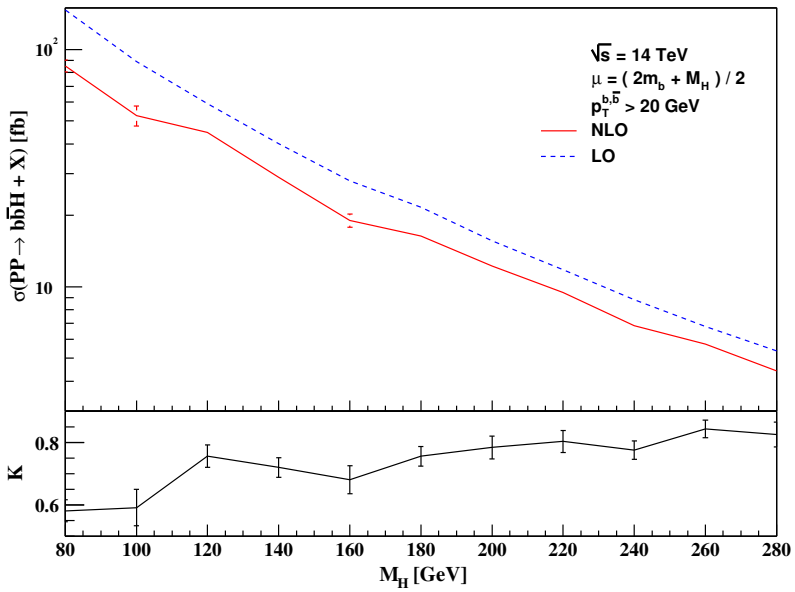

Figure 7.4: The total cross section for $PP \to b\bar{b}H + X$ in LO and NLO at the LHC requiring a $p_T > 20\,\text{GeV}$ for each quark. The error bars are the statistical errors from the MC integration.

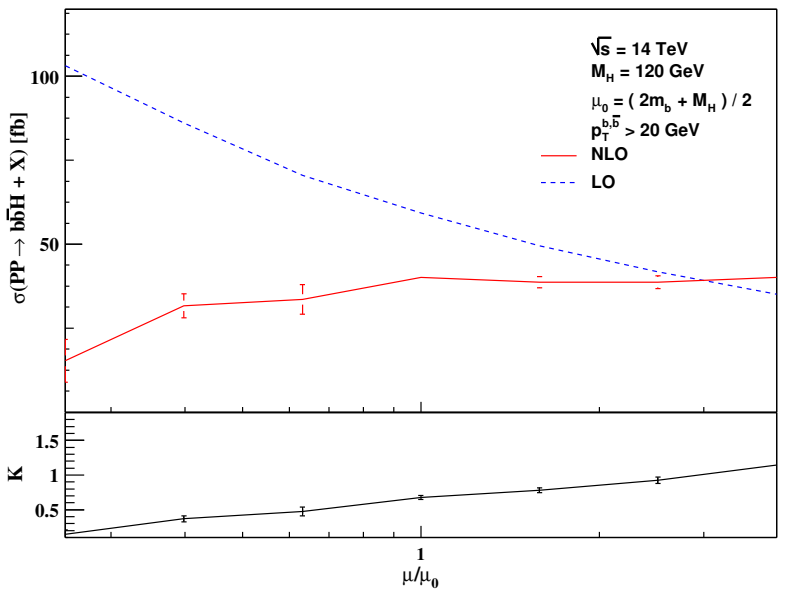

Figure 7.5: The scale dependence of the total cross section for $PP \to b\bar{b}H + X$ in LO and NLO at the LHC requiring a $p_T > 20\,\text{GeV}$ for each quark. The error bars are the statistical errors from the MC integration.

$(\overline{m}_b(\mu)/m_b)^2 \sim 1/2$. Large negative corrections are caused by the mass renormalization when using the pole mass. By employing the running mass these large corrections are absorbed into the LO cross section. Hence the K factor is expected to be closer to one.

Chapter 8

Summary and Conclusions

Higgs radiation off heavy quarks is a very important process for Higgs physics. First of all, for light Higgs masses it can probably increase the Higgs discovery potential at the TEVATRON and represents a substantial contribution of the Higgs signal at the LHC. All available data from experiments are hinting to a light Higgs. For $M_H \lesssim 120$ GeV $t\bar{t}H$ production provides a major contribution to the 5σ discovery contour at the LHC. Secondly, this process permits a first direct measurement of the top Yukawa coupling presumed that the branching ratio of the Higgs boson decay into $b\bar{b}$ is known. Through the Higgs–Kibble mechanism this coupling is related to the top-quark mass and the vacuum expectation value which are already known. Therefore the determination of the Yukawa coupling provides an experimental test of the Higgs sector of the SM and hence an access to the generation of fermion masses.

In supersymmetric theories $b\bar{b}H$ production is of high interest. The $b\bar{b}H$ coupling is strongly enhanced in scenarios with large $\tan\beta$ which leads to an enhancement of the cross section. In this parameter region this process is a promising discovery channel at the TEVATRON and the LHC. It may also allow a second independent determination of the bottom Yukawa coupling, in addition to the measurement of the branching ratio of the decay channel $H \to b\bar{b}$.

However, despite its experimental importance the status of the theoretical prediction was not satisfactory for a long time. The LO approximation of the cross section for $P\bar{P}/PP \to t\bar{t}H + X$ has a very large scale dependence. Hence the cross section was only known within a factor of two. This thesis contributes to fill the gap in the solid prediction of the cross section which is necessary for the experimental analysis. It presents the full NLO QCD corrections to Higgs radiation off heavy quarks in hadron–hadron collisions.

The calculation of the radiative QCD corrections for this process is quite involved. The appearance of IR-divergent five-point functions and the complex structure of the soft and collinear divergences in the virtual and the real corrections are the main challenges. For extracting the IR divergences of the real corrections and matching them with the ones

coming from the virtual corrections, a new version of the dipole subtraction formalism has been employed.

The most important result is the enormous reduction of the scale dependence of the cross section after including the NLO QCD corrections. At the TEVATRON, the uncertainty due to the scale dependence is reduced from a factor of three to 30%. The reduction is similarly striking for the LHC, namely from a factor 2.5 to 25%. Therefore the remaining theoretical uncertainty is roughly of order 10% to 15% as indicated by the scale uncertainty.

The NLO QCD corrections reduce the cross section slightly at the TEVATRON with a K factor of ~ 0.8 for the renormalization and factorization scales set to half the threshold energy. In contrast, at the LHC they slightly increase the cross section with a K factor of ~ 1.2 for the same renormalization and factorization scales. The K factors at the TEVATRON and the LHC are almost independent of the Higgs mass.

For an experimental analysis distributions in boost-invariant variables are very important. Several differential cross sections with respect to the transverse momentum of different particles have been presented in this thesis. The approximation of rescaling the LO distribution with the corresponding K factor obtained from the total cross section sufficiently describes the NLO distribution in most cases. Nevertheless, for some differential cross sections at the LHC the full NLO prediction is inevitable.

The leading threshold corrections from the Coulomb singularity and the soft and collinear radiation have been worked out. It turned out that they are not able to describe the full NLO prediction of the total cross section properly. Hence they cannot be used as an approximation for a faster numerical evaluation.

The calculation of the cross section for $P\bar{P}/PP \to b\bar{b}H + X$ is more involved than for top quarks due to the large mass difference between the Higgs and the bottom quark. Large logarithms may spoil the convergence of perturbation theory. This difficulty is absent when requiring a transverse momentum larger than a given cut value for each b quark. A first outlook on the results has been given in this thesis.

As in the case of $t\bar{t}H$ production the scale dependence is strongly reduced by including the NLO QCD corrections. At the TEVATRON the NLO prediction lies roughly 30% below the LO for $M_H = 100\,\text{GeV}$ and roughly 10% above for $M_H = 250\,\text{GeV}$. At the LHC the NLO QCD corrections reduce the cross section by roughly 40% for $M_H = 100\,\text{GeV}$ and by roughly 20% for $M_H = 250\,\text{GeV}$.

Although the Monte Carlo integration in the case of $b\bar{b}H$ production is faced with numerical problems the results presented here are already very promising. For the stabilization of the Monte Carlo integration a full NLO Monte Carlo generator is needed but this is beyond the scope of this thesis. For the extension to the MSSM the inclusion of the supersymmetric modifications in the $Q\bar{Q}H$ vertex is necessary. Nevertheless, a first approximation of the cross section in the MSSM can be obtained by rescaling the SM prediction by the ratio of the couplings in both theories.

Appendix A

The Standard Matrix Elements

A.1 The $q\bar{q}$ Channel

For the SME the following chains of Dirac matrices are needed:

$$\begin{aligned}
\Gamma^{q\bar{q},\mu_1\mu_2\cdots} &= \bar{v}(p_2)\,\gamma^{\mu_1}\gamma^{\mu_2}\cdots u(p_1), \\
\Gamma^{Q\bar{Q}}_{\mu_1\mu_2\cdots} &= \bar{u}(p_3)\,\gamma_{\mu_1}\gamma_{\mu_2}\cdots v(p_4), \\
\Gamma^{Q\bar{Q}}_{1} &= \bar{u}(p_3)\,v(p_4).
\end{aligned} \tag{A.1}$$

In addition, the short-handed notation $\Gamma_p = \Gamma_\mu\, p^\mu$ for contractions with a vector is used. Below all needed SMEs for the $q\bar{q}$ channel are listed. The four SMEs sufficient for describing the tree-level amplitude are already given in Section 3.2. The labeling is taken from the FORM programs for calculating the formfactors, and is the same used in the C++ code for the numerical evaluation.

$$\begin{aligned}
\mathcal{M}^{q\bar{q}}_{1,2,3,4} &= \Gamma^{q\bar{q},p_3}\left\{\Gamma^{Q\bar{Q}}_{1},\Gamma^{Q\bar{Q}}_{p_1},\Gamma^{Q\bar{Q}}_{p_2},\Gamma^{Q\bar{Q}}_{p_1p_2}\right\}, \\
\mathcal{M}^{q\bar{q}}_{5,6,7,8} &= \Gamma^{q\bar{q},p_4}\left\{\Gamma^{Q\bar{Q}}_{1},\Gamma^{Q\bar{Q}}_{p_1},\Gamma^{Q\bar{Q}}_{p_2},\Gamma^{Q\bar{Q}}_{p_1p_2}\right\}, \\
\mathcal{M}^{q\bar{q}}_{9,10,11,12} &= \Gamma^{q\bar{q},\mu}\left\{\Gamma^{Q\bar{Q}}_{\mu},\Gamma^{Q\bar{Q}}_{\mu p_1},\Gamma^{Q\bar{Q}}_{\mu p_2},\Gamma^{Q\bar{Q}}_{\mu p_1p_2}\right\}, \\
\mathcal{M}^{q\bar{q}}_{13,14,15} &= \Gamma^{q\bar{q},\mu p_3p_4}\left\{\Gamma^{Q\bar{Q}}_{\mu},\Gamma^{Q\bar{Q}}_{\mu p_1},\Gamma^{Q\bar{Q}}_{\mu p_2}\right\}, \\
\mathcal{M}^{q\bar{q}}_{16,17,18,19} &= \Gamma^{q\bar{q},\mu\nu p_3}\left\{\Gamma^{Q\bar{Q}}_{\mu\nu},\Gamma^{Q\bar{Q}}_{\mu\nu p_1},\Gamma^{Q\bar{Q}}_{\mu\nu p_2},\Gamma^{Q\bar{Q}}_{\mu\nu p_1p_2}\right\}, \\
\mathcal{M}^{q\bar{q}}_{20,21,22,23} &= \Gamma^{q\bar{q},\mu\nu p_4}\left\{\Gamma^{Q\bar{Q}}_{\mu\nu},\Gamma^{Q\bar{Q}}_{\mu\nu p_1},\Gamma^{Q\bar{Q}}_{\mu\nu p_2},\Gamma^{Q\bar{Q}}_{\mu\nu p_1p_2}\right\}, \\
\mathcal{M}^{q\bar{q}}_{24,25} &= \Gamma^{q\bar{q},\mu\nu\rho}\left\{\Gamma^{Q\bar{Q}}_{\mu\nu\rho p_1},\Gamma^{Q\bar{Q}}_{\mu\nu\rho p_2}\right\}.
\end{aligned} \tag{A.2}$$

The LO formfactors are given in Section 3.2. At NLO two colour structures occur for the $q\bar{q}$ channel while at LO only $\mathcal{C}_1^{q\bar{q}}$ contributes. Note that they are chosen to be orthogonal.

Therefore even at NLO all $F_{i,2}$ drop out in the final result.

$$\begin{aligned} \mathcal{C}_1^{q\bar{q}} &= i\, t^c_{c_4 c_3}\, t^c_{c_2 c_1}, \\ \mathcal{C}_2^{q\bar{q}} &= i\, \delta_{c_4 c_3}\, \delta_{c_2 c_1}. \end{aligned} \tag{A.3}$$

A.2 The gg Channel

Despite the definitions in Eq. (A.1), the following abbreviations for scalar products will be used:

$$\begin{aligned} \mathcal{G}_{ij} &= \epsilon_i \cdot \epsilon_j, \\ \mathcal{G}_{ik} &= \epsilon_i \cdot p_k, \\ \mathcal{G}_{ik,jl} &= \mathcal{G}_{ik}\, \mathcal{G}_{jl}, \end{aligned} \tag{A.4}$$

with $i, j = 1, 2$ and $k, l = 3, 4$.

The number of SMEs needed for the gg channel is much larger than for the $q\bar{q}$ channel. At tree level the twelve SMEs $\mathcal{M}_1^{gg}$, $\mathcal{M}_2^{gg}$, $\mathcal{M}_3^{gg}$, $\mathcal{M}_4^{gg}$, $\mathcal{M}_5^{gg}$, $\mathcal{M}_{20}^{gg}$, $\mathcal{M}_{25}^{gg}$, $\mathcal{M}_{26}^{gg}$, $\mathcal{M}_{33}^{gg}$, $\mathcal{M}_{34}^{gg}$, $\mathcal{M}_{37}^{gg}$, and $\mathcal{M}_{40}^{gg}$ contribute.

$$\begin{aligned} \mathcal{M}^{gg}_{1,2,3,4,5} &= \Gamma^{Q\bar{Q}}_{1}\ \{\mathcal{G}_{13,23}, \mathcal{G}_{13,24}, \mathcal{G}_{14,23}, \mathcal{G}_{14,24}, \mathcal{G}_{12}\}, \\ \mathcal{M}^{gg}_{6,7,8,9,10} &= \Gamma^{Q\bar{Q}}_{p_1}\ \{\mathcal{G}_{13,23}, \mathcal{G}_{13,24}, \mathcal{G}_{14,23}, \mathcal{G}_{14,24}, \mathcal{G}_{12}\}, \\ \mathcal{M}^{gg}_{11,12,13,14,15} &= \Gamma^{Q\bar{Q}}_{p_2}\ \{\mathcal{G}_{13,23}, \mathcal{G}_{13,24}, \mathcal{G}_{14,23}, \mathcal{G}_{14,24}, \mathcal{G}_{12}\}, \\ \mathcal{M}^{gg}_{16,17,18,19,20} &= \Gamma^{Q\bar{Q}}_{p_1 p_2}\ \{\mathcal{G}_{13,23}, \mathcal{G}_{13,24}, \mathcal{G}_{14,23}, \mathcal{G}_{14,24}, \mathcal{G}_{12}\}, \\ \mathcal{M}^{gg}_{21,22} &= \Gamma^{Q\bar{Q}}_{\epsilon_1}\ \{\mathcal{G}_{23}, \mathcal{G}_{24}\}, \\ \mathcal{M}^{gg}_{23,24} &= \Gamma^{Q\bar{Q}}_{\epsilon_2}\ \{\mathcal{G}_{13}, \mathcal{G}_{14}\}, \\ \mathcal{M}^{gg}_{25,26} &= \Gamma^{Q\bar{Q}}_{\epsilon_1 p_1}\ \{\mathcal{G}_{23}, \mathcal{G}_{24}\}, \\ \mathcal{M}^{gg}_{27,28} &= \Gamma^{Q\bar{Q}}_{\epsilon_1 p_2}\ \{\mathcal{G}_{23}, \mathcal{G}_{24}\}, \\ \mathcal{M}^{gg}_{29,30} &= \Gamma^{Q\bar{Q}}_{\epsilon_1 p_1 p_2}\ \{\mathcal{G}_{23}, \mathcal{G}_{24}\}, \\ \mathcal{M}^{gg}_{31,32} &= \Gamma^{Q\bar{Q}}_{\epsilon_2 p_1}\ \{\mathcal{G}_{13}, \mathcal{G}_{14}\}, \\ \mathcal{M}^{gg}_{33,34} &= \Gamma^{Q\bar{Q}}_{\epsilon_2 p_2}\ \{\mathcal{G}_{13}, \mathcal{G}_{14}\}, \\ \mathcal{M}^{gg}_{35,36} &= \Gamma^{Q\bar{Q}}_{\epsilon_2 p_1 p_2}\ \{\mathcal{G}_{13}, \mathcal{G}_{14}\}, \\ \mathcal{M}^{gg}_{37,38,39,40} &= \left\{\Gamma^{Q\bar{Q}}_{\epsilon_1\epsilon_2}, \Gamma^{Q\bar{Q}}_{\epsilon_1\epsilon_2 p_1}, \Gamma^{Q\bar{Q}}_{\epsilon_1\epsilon_2 p_2}, \Gamma^{Q\bar{Q}}_{\epsilon_1\epsilon_2 p_1 p_2}\right\}. \end{aligned} \tag{A.5}$$

The colour structures are discussed in Section 3.2. The LO formfactors are listed below, ordered by the colour structures which are related to the t, u, and s channel exchange in the diagrams.

$$
\begin{aligned}
F^{gg}_{1,1} &= -\frac{16}{(s_{45}-m_Q^2)(t_{13}-m_Q^2)}, & F^{gg}_{33,1} &= -\frac{1}{2}\left(F^{gg}_{1,1}-F^{gg}_{2,1}\right),\\
F^{gg}_{2,1} &= +\frac{16}{(t_{13}-m_Q^2)(t_{24}-m_Q^2)}, & F^{gg}_{34,1} &= +\frac{1}{2}F^{gg}_{4,1},\\
F^{gg}_{4,1} &= -\frac{16}{(s_{35}-m_Q^2)(t_{24}-m_Q^2)}, & F^{gg}_{37,1} &= +\frac{4}{s_{35}-m_Q^2}+\frac{4}{s_{45}-m_Q^2},\\
F^{gg}_{25,1} &= -\frac{1}{2}F^{gg}_{1,1}, & F^{gg}_{40,1} &= -\frac{1}{4}\left(F^{gg}_{1,1}-F^{gg}_{2,1}+F^{gg}_{4,1}\right),\\
F^{gg}_{26,1} &= -\frac{1}{2}\left(F^{gg}_{2,1}-F^{gg}_{4,1}\right),
\end{aligned}
$$

$$
\begin{aligned}
F^{gg}_{1,2} &= -\frac{16}{(s_{45}-m_Q^2)(t_{23}-m_Q^2)}, & F^{gg}_{26,2} &= +\frac{1}{2}F^{gg}_{4,2},\\
F^{gg}_{3,2} &= +\frac{16}{(t_{14}-m_Q^2)(t_{23}-m_Q^2)}, & F^{gg}_{33,2} &= -\frac{1}{2}F^{gg}_{1,2},\\
F^{gg}_{4,2} &= -\frac{16}{(s_{35}-m_Q^2)(t_{14}-m_Q^2)}, & F^{gg}_{34,2} &= -\frac{1}{2}\left(F^{gg}_{3,2}-F^{gg}_{4,2}\right),\\
F^{gg}_{5,2} &= -\frac{\hat{s}}{2}\left(F^{gg}_{1,2}-F^{gg}_{3,2}+F^{gg}_{4,2}\right)+2F^{gg}_{37,1}, & F^{gg}_{37,2} &= -\frac{1}{2}F^{gg}_{5,2},\\
F^{gg}_{20,2} &= +\frac{1}{2}\left(F^{gg}_{1,2}-F^{gg}_{3,2}+F^{gg}_{4,2}\right), & F^{gg}_{40,2} &= -\frac{1}{2}F^{gg}_{20,2},\\
F^{gg}_{25,2} &= -\frac{1}{2}\left(F^{gg}_{1,2}-F^{gg}_{3,2}\right),
\end{aligned}
$$

$$
\begin{aligned}
F^{gg}_{5,3} &= +\frac{4}{\hat{s}}\left(\frac{t_{14}-m_Q^2}{s_{35}-m_Q^2}-\frac{t_{24}-m_Q^2}{s_{35}-m_Q^2}-\frac{t_{13}-m_Q^2}{s_{45}-m_Q^2}+\frac{t_{23}-m_Q^2}{s_{45}-m_Q^2}\right)+F^{gg}_{37,1},\\
F^{gg}_{20,3} &= -\frac{2}{\hat{s}}\,F^{gg}_{37,1}.
\end{aligned}
\tag{A.6}
$$

Appendix B

The LSZ Factors

The LSZ formula describes the relation between the S-matrix elements and the truncated $(n+m)$-point Greens function $\tilde{G}^{(n+m)}_{0,tr}$ in momentum space:

$$\langle k'_1,\ldots,k'_m|\,S\,|k_1,\ldots,k_n\rangle = \lim_{k'_i,k_i\to m^2_{\text{on}}} R^{\frac{n+m}{2}}\tilde{G}^{(n+m)}_{0,tr}(k'_1,\ldots,k'_m,k_1,\ldots,k_n). \tag{B.1}$$

The untruncated Greens function in coordinate space are given by

$$G^{(n)}_0(x_1,\ldots,x_n) \;=\; \langle 0|\mathrm{T}\left[\Phi_0(x_1)\cdots\Phi_0(x_n)\right]|0\rangle\,, \tag{B.2}$$

and the factor R by the residue of the two-point Greens function,

$$iR \;=\; \mathrm{Res}_{k^2\to m^2_{\text{on}}}\tilde{G}^{(2)}_0(k^2). \tag{B.3}$$

Renormalizing the fields via $\Phi_0 = \sqrt{Z_\Phi}\,\Phi_R$ yields the renormalized Greens function

$$G^{(n)}_R(x_1,\ldots,x_n) \;=\; (Z_\Phi)^{-\frac{n}{2}}\,\langle 0|\mathrm{T}\left[\Phi_0(x_1)\cdots\Phi_0(x_n)\right]|0\rangle\,. \tag{B.4}$$

Inserting this into the LSZ formula leads to

$$\langle k'_1,\ldots,k'_m|\,S\,|k_1,\ldots,k_n\rangle = \lim_{k'_i,k_i\to m^2_{\text{on}}} \mathcal{Z}_\Phi^{\frac{n+m}{2}}\tilde{G}^{(n+m)}_{R,tr}(k'_1,\ldots,k'_m,k_1,\ldots,k_n) \tag{B.5}$$

with

$$i\mathcal{Z}_\Phi = i\frac{R}{Z_\Phi} = \frac{1}{Z_\Phi}\mathrm{Res}_{k^2\to m^2_{\text{on}}}\tilde{G}^{(2)}_0(k^2) = \mathrm{Res}_{k^2\to m^2_{\text{on}}}\tilde{G}^{(2)}_R(k^2). \tag{B.6}$$

The renormalized untruncated two-point Greens function for a quark at the one-loop level is given by

$$\tilde{G}^{(2)}_R \;=\; \frac{i}{(\not{p}-m_Q)\left[1+\Sigma^P_Q(p^2)+\delta Z_Q\right]+m_Q\left[\Sigma^P_Q(p^2)+\Sigma^S_Q(p^2)-\frac{\delta m_Q}{m_Q}\right]}. \tag{B.7}$$

In this work only stable particles are considered. In this case the pole of $\tilde{G}_R^{(2)}$ is the on-shell mass:

$$m_{Q,\mathrm{on}} = m_Q - m_Q \left(\Sigma^P(m^2_{Q,\mathrm{on}}) + \Sigma^S(m^2_{Q,\mathrm{on}}) - \frac{\delta m_Q}{m_Q} \right). \tag{B.8}$$

Using this relation the calculation of the residue yields

$$\begin{aligned} \mathcal{Z}_Q &= 1 - \Sigma_Q^P(m^2_{Q,\mathrm{on}}) - \delta Z_Q - 2m^2_{Q,\mathrm{on}} \frac{\partial}{\partial p^2} \left(\Sigma_Q^P(p^2) + \Sigma_Q^S(p^2) \right)_{p^2=m_{Q,\mathrm{on}}} \\ &\quad + \text{ higher terms.} \end{aligned} \tag{B.9}$$

In the on-shell scheme this simplifies to

$$\mathcal{Z}_Q^{\mathrm{on-shell}} = 1, \tag{B.10}$$

while in the $\overline{MS}$ scheme for a massless quark it results in

$$\begin{aligned} \mathcal{Z}_q^{\overline{MS}} &= 1 - \Sigma_Q^P(0) - \delta Z_q \\ &= 1 - \frac{\alpha_s}{4\pi} C_F B_0(0;0,0) - \delta Z_q. \end{aligned} \tag{B.11}$$

The renormalized untruncated two-point Greens function for the gluon at the one-loop level is given by

$$\tilde{G}^{(2),ab}_{R,\mu\nu} = -i\,\delta_{ab} \frac{1}{k^2} \left(g_{\mu\nu} - \frac{k_\mu k_\nu}{k^2} \right) \frac{1}{1 + \hat{\Pi}_T(k^2)} - i\,\delta_{ab} \frac{k_\mu k_\nu}{k^4} \tag{B.12}$$

with the renormalized gluon self-energy $\hat{\Pi}_T = \Pi_T + \delta Z_G$. The residue is given by

$$\mathrm{Res}_{p^2 \to m_{g,\mathrm{on}}=0} \tilde{G}^{(2),ab}_{R,\mu\nu} = -i\,\delta_{ab}\, g_{\mu\nu} \frac{1}{1 + \hat{\Pi}_T(0)} \tag{B.13}$$

from which the factor $\mathcal{Z}_T$ can be derived:

$$\mathcal{Z}_G = \frac{1}{1 + \hat{\Pi}_T(0)} = 1 - \hat{\Pi}_T(0) + \mathcal{O}(\alpha_s^2) = 1 - \Pi_T(0) - \delta Z_G + \mathcal{O}(\alpha_s^2). \tag{B.14}$$

In the used version of the $\overline{MS}$ scheme $\delta\mathcal{Z}_G$ receives contributions from gluon/ghosts and from the N_f light quarks:

$$\delta\mathcal{Z}_G = +\frac{\alpha_s}{4\pi} \left(5 - \frac{2}{3} N_f \right) \Big[B_0(0;0,0) - \Delta_{UV} \Big]. \tag{B.15}$$

Appendix C

The One-Loop Integrals

C.1 Notations

The standard integrals are defined as

$$\begin{aligned}
B_0(p_1^2; m_0, m_1) &= \frac{(2\pi\mu)^{4-D}}{i\pi^2} \int d^D k \, \frac{1}{d_0 d_1}, \\
C_0(p_1^2, p_2^2, s; m_0, m_1, m_2) &= \frac{(2\pi\mu)^{4-D}}{i\pi^2} \int d^D k \, \frac{1}{d_0 d_1 d_2}, \\
D_0(p_1^2, p_2^2, p_3^2, p_4^2, s, t_1; m_0, m_1, m_2, m_3) &= \frac{(2\pi\mu)^{4-D}}{i\pi^2} \int d^D k \, \frac{1}{d_0 d_1 d_2 d_3}, \\
E_0(p_1^2, p_2^2, p_3^2, p_4^2, p_5^2, s, t_1, s_1, s_2, t_2; m_0, m_1, m_2, m_3, m_4) &= \frac{(2\pi\mu)^{4-D}}{i\pi^2} \int d^D k \, \frac{1}{d_0 d_1 d_2 d_3 d_4}
\end{aligned} \tag{C.1}$$

with the abbreviations $s = (p_1 + p_2)^2$, $t_1 = (p_2 + p_3)^2$, $s_1 = (p_3 + p_4)^2$, $s_2 = (p_4 + p_5)^2$, and $t_2 = (p_5 + p_1)^2$. The p_i denote the external momenta (see Fig. C.1). The denominators of the n-point functions are given by

$$d_i = (k + k_i)^2 - m_i^2 + 0i, \quad i = 1, \ldots, n-1, \tag{C.2}$$

where $0i$ indicates an infinitesimal positive imaginary part, and the momenta k_i are related to the external momenta by

$$k_i = \sum_{l=1}^{i} p_l, \tag{C.3}$$

$$k_0 = k_n = \sum_{l=1}^{n} p_l = 0. \tag{C.4}$$

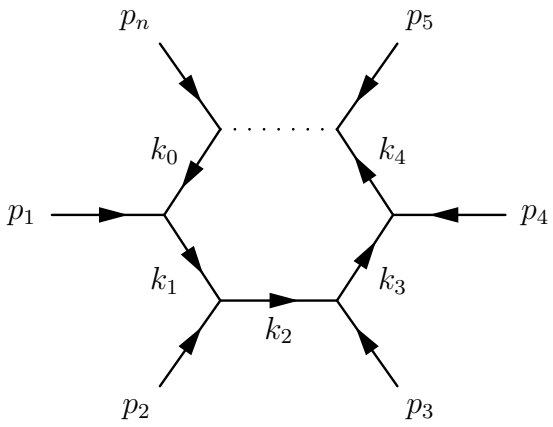

Figure C.1: The assignments of internal and external momenta of the integrals.

The following notations will be used below:

$$\begin{aligned} C_\varepsilon(m^2) &= \Gamma(1+\varepsilon)\left(\frac{4\pi\mu_{IR}^2}{m^2}\right)^\varepsilon, \\ \bar{q}^{\,2} &= q^2 + i\,0, \qquad \bar{q}_Q^2 = \bar{q}^{\,2} - m_Q^2, \\ \beta_{q^2} &= \sqrt{1-4m_Q^2/\bar{q}^{\,2}} \qquad \text{and} \qquad x_{q^2} = \frac{\beta_{q^2}-1}{\beta_{q^2}+1}, \end{aligned} \tag{C.5}$$

with $q^2 = s, s_1, s_2, t_1, t_2$ and $D = 4 - 2\varepsilon$. The only scalar integral containing both UV and IR divergences is $B_0(0;0,0)$:

$$B_0(0;0,0) = (4\pi)^\varepsilon\,\Gamma(1+\varepsilon)\left[\frac{1}{\varepsilon_{UV}} + \log\left(\frac{\mu_{UV}^2}{\mu_{IR}^2}\right) - \frac{1}{\varepsilon_{IR}}\right] = \Delta_{UV} - \frac{C_\varepsilon(\mu_{UV}^2)}{\varepsilon_{IR}}. \tag{C.6}$$

Since all integrals listed below are only IR divergent the subscript *IR* of ε_{IR} is dropped from now on. For the renormalization constant of the heavy quark field the IR-divergent derivative of the two-point function is needed,

$$B_0'(m^2;m,0) = -\frac{C_\epsilon(m^2)}{2m^2}\left[\frac{1}{\varepsilon}+2\right]. \tag{C.7}$$

The dilogarithm $\mathrm{Li}_2(z)$ is defined in the usual way. For the analytical continuation the following specific combinations of logarithms and dilogarithms will be needed:

$$\begin{aligned} \mathcal{L}\mathrm{i}_2(x,y) &= \mathrm{Li}_2(1-xy) + \log(1-xy)\Big[\log(xy) - \log(x) - \log(y)\Big], \\ \mathcal{L}\mathrm{i}_2(x,y,z) &= \mathrm{Li}_2(1-xyz) + \log(1-xyz)\Big[\log(xyz) - \log(x) - \log(y) - \log(z)\Big]. \end{aligned} \tag{C.8}$$

C.2 The Divergent Scalar Three- and Four-Point Integrals

Below all needed IR-divergent three- and four-point integrals are listed [56]. They have been calculated in two independent ways using the Feynman-parameter method as well as cutting techniques and dispersion integrals. The integrals $C_0(m_Q^2, m_Q^2, s; m_Q, 0, m_Q)$ and $D_0(0, m_Q^2, s_1, s_2, s, t_1; 0, 0, m_Q, m_Q)$ can be taken from Ref. [145]. The results there were obtained by employing a mass regulator λ and can be translated into the results given here by the substitution $\ln(\lambda^2/q^2) \to C_\varepsilon(q^2)/\varepsilon$. The convergent integrals can be found in Ref. [146, 147].

$$C_0(0,0,s;0,0,0) = \frac{C_\varepsilon(-\bar{s})}{s}\left[\frac{1}{\varepsilon^2} - \zeta(2)\right], \tag{C.9}$$

$$C_0(0,m_Q^2,s;0,0,m_Q) = \frac{C_\varepsilon(m_Q^2)}{s_Q}\left[\frac{1}{2\varepsilon^2} - \frac{1}{\varepsilon}\log\left(\frac{-\bar{s}_Q}{m_Q^2}\right) + \mathrm{Li}_2\left(1+\frac{\bar{s}_Q}{m_Q^2}\right) + \log^2\left(\frac{-\bar{s}_Q}{m_Q^2}\right)\right], \tag{C.10}$$

$$C_0(0,s_1,s;0,0,m_Q) = \frac{C_\varepsilon(m_Q^2)}{s-s_1}\left[-\frac{1}{\varepsilon}\log\left(\frac{\bar{s}_Q}{\bar{s}_{1Q}}\right) + \mathrm{Li}_2\left(1+\frac{\bar{s}_Q}{m_Q^2}\right) - \mathrm{Li}_2\left(1+\frac{\bar{s}_{1Q}}{m_Q^2}\right) + \log^2\left(\frac{-\bar{s}_Q}{m_Q^2}\right) - \log^2\left(\frac{-\bar{s}_{1Q}}{m_Q^2}\right)\right], \tag{C.11}$$

$$C_0(m_Q^2,m_Q^2,s;m_Q,0,m_Q) = \frac{C_\varepsilon(m_Q^2)}{s\beta_s}\left[\frac{1}{\varepsilon}\log(x_s) - 2\,\mathrm{Li}_2(-x_s) - 2\log(x_s)\,\log(1+x_s) + \frac{1}{2}\log^2(x_s) - \zeta(2)\right]. \tag{C.12}$$

$$D_0(0,0,s_1,m_Q^2,s,t_1;0,0,0,m_Q) = \frac{C_\varepsilon(m_Q^2)}{s\,t_{1Q}}\left[\frac{3}{2\varepsilon^2} - \frac{1}{\varepsilon}\left\{2\log\left(\frac{-\bar{t}_{1Q}}{m_Q^2}\right) + \log\left(\frac{-\bar{s}}{m_Q^2}\right) - \log\left(\frac{-\bar{s}_{1Q}}{m_Q^2}\right)\right\} - 2\,\mathrm{Li}_2\left(1-\frac{\bar{s}_{1Q}}{\bar{t}_{1Q}}\right) + 2\log\left(\frac{-\bar{s}}{m_Q^2}\right)\log\left(\frac{-\bar{t}_{1Q}}{m_Q^2}\right) - \log^2\left(\frac{-\bar{s}_{1Q}}{m_Q^2}\right) - 4\,\zeta(2)\right], \tag{C.13}$$

$$
\begin{aligned}
&D_0(0, m_Q^2, s_1, m_Q^2, s, t_1; 0, 0, m_Q, m_Q) \;=\\
&\quad \frac{C_\varepsilon(m_Q^2)}{s_Q\, t_{1Q}} \Bigg[\frac{1}{\varepsilon^2} - \frac{1}{\varepsilon} \left\{ \log\!\left(\frac{-\bar{t}_{1Q}}{m_Q^2}\right) + \log\!\left(\frac{-\bar{s}_Q}{m_Q^2}\right) \right\} \\
&\qquad\qquad - \log^2(x_{s_1}) + 2\log\!\left(\frac{-\bar{s}_Q}{m_Q^2}\right) \log\!\left(\frac{-\bar{t}_{1Q}}{m_Q^2}\right) - 4\,\zeta(2) \Bigg], \qquad \text{(C.14)}
\end{aligned}
$$

$$
\begin{aligned}
&D_0(0, m_Q^2, s_1, s_2, s, t_1; 0, 0, m_Q, m_Q) \;=\\
&\quad \frac{C_\varepsilon(m_Q^2)}{s_Q\, t_{1Q}} \Bigg[\frac{1}{2\varepsilon^2} - \frac{1}{\varepsilon} \left\{ \log\!\left(\frac{-\bar{s}_Q}{m_Q^2}\right) + \log\!\left(\frac{\bar{t}_{1Q}}{\bar{s}_{2Q}}\right) \right\} - \sum_{\rho=\pm 1} \mathcal{L}\mathrm{i}_2\!\left(\frac{\bar{s}_{2Q}}{\bar{s}_Q}, x_{s_1}^\rho\right) \\
&\qquad\qquad - 2\,\mathrm{Li}_2\!\left(1 - \frac{\bar{s}_{2Q}}{\bar{t}_{1Q}}\right) + 2\log\!\left(\frac{-\bar{s}_Q}{m_Q^2}\right) \log\!\left(\frac{-\bar{t}_{1Q}}{m_Q^2}\right) \\
&\qquad\qquad - \log^2\!\left(\frac{-\bar{s}_{2Q}}{m_Q^2}\right) - \log^2(x_{s_1}) - \zeta(2) \Bigg], \qquad \text{(C.15)}
\end{aligned}
$$

$$
\begin{aligned}
&D_0(m_Q^2, m_Q^2, s_1, s_2, s, t_1; m_Q, 0, m_Q, m_Q) \;=\\
&\quad \frac{C_\varepsilon(m_Q^2)}{t_{1Q}\, s\beta_s} \Bigg[\frac{1}{\varepsilon}\, \log(x_s) - \sum_{\rho,\,\sigma=\pm 1} \mathcal{L}\mathrm{i}_2(x_s, x_{s_1}^\rho, x_{s_2}^\sigma) - \mathrm{Li}_2(x_s^2) \\
&\qquad\qquad - 2\log(x_s)\log(1 - x_s^2) - 2\log(x_s)\log\!\left(\frac{-\bar{t}_{1Q}}{m_Q^2}\right) \\
&\qquad\qquad - \log^2(x_{s_1}) - \log^2(x_{s_2}) + \zeta(2) \Bigg]. \qquad \text{(C.16)}
\end{aligned}
$$

C.3 The Singularity Structure

As mentioned in Section 4.3, the soft and collinear divergence structure of the four-point integrals given above can be represented in terms of three-point integrals:

$$
\begin{aligned}
D_{0,\mathrm{sing}}^{(D,\mathrm{mass})}(0, 0, s_1, m_Q^2, s, t_1; 0, 0, 0, m_Q) \;=\; & \frac{1}{t_{1Q}}\, C_0^{(D,\mathrm{mass})}(0, 0, s; 0, 0, 0) \\
& + \frac{t_1 - s_1}{s\, t_{1Q}}\, C_0^{(D,\mathrm{mass})}(0, s_1, t_1; 0, 0, m_Q) \\
& + \frac{1}{s}\, C_0^{(D,\mathrm{mass})}(0, m_Q^2, t_1; 0, 0, m_Q),
\end{aligned}
$$

$$
\begin{aligned}
D^{(D,\mathrm{mass})}_{0,\mathrm{sing}}(0,m_Q^2,s_1,m_Q^2,s,t_1;0,0,m_Q,m_Q) &= \frac{1}{t_{1Q}}\,C_0^{(D,\mathrm{mass})}(0,m_Q^2,s;0,0,m_Q) \\
&\quad + \frac{1}{s_Q}\,C_0^{(D,\mathrm{mass})}(0,m_Q^2,t_1;0,0,m_Q), \\
D^{(D,\mathrm{mass})}_{0,\mathrm{sing}}(0,m_Q^2,s_1,s_2,s,t_1;0,0,m_Q,m_Q) &= \frac{1}{t_{1Q}}\,C_0^{(D,\mathrm{mass})}(0,m_Q^2,s;0,0,m_Q) \\
&\quad + \frac{t_1-s_2}{s_Q\,t_{1Q}}\,C_0^{(D,\mathrm{mass})}(0,t_1,s_2;0,0,m_Q), \\
D^{(D,\mathrm{mass})}_{0,\mathrm{sing}}(m_Q^2,m_Q^2,s_1,s_2,s,t_1;m_Q,0,m_Q,m_Q) &= \frac{1}{t_{1Q}}\,C_0^{(D,\mathrm{mass})}(m_Q^2,m_Q^2,s;m_Q,0,m_Q).
\end{aligned}
\tag{C.17}
$$

To obtain the coefficients in front of the soft and collinear divergent three-point functions one has to consider the appropriate soft and collinear limit, respectively. For instance, the collinear limit for $D_0^{(D,\mathrm{mass})}(0,m_Q^2,s_1,s_2,s,t_1;0,0,m_Q,m_Q)$ is reached when the loop momentum k becomes collinear with p_1, $k \sim xp_1$. The four denominator simplify to

$$
\begin{aligned}
d_0 &= k^2-\lambda^2 \sim 0, \\
d_1 &= (k+p_1)^2-\lambda^2 \sim 0, \\
d_2 &= (k+p_1+p_2)^2-m_Q^2 \;\sim\; 2(1+x)(p_1\cdot p_2) \;=\; (1+x)(s-m_Q^2), \\
d_3 &= (k-p_4)^2-m_Q^2 \;\sim\; s_2-m_Q^2-2x(p_1\cdot p_4) \;=\; s_2-m_Q^2-x(t_1-m_Q^2).
\end{aligned}
$$

Using a partial fractioning in x for the last two denominators,

$$
\frac{1}{d_2 d_3} \;\sim\; \frac{1}{t_1-m_Q^2}\left[\frac{1}{d_2}+\frac{t_1-s_2}{s-m_Q^2}\,\frac{1}{d_3}\right],
$$

leads to the final decomposition given in Eq. (C.17).

In the presence of more than one collinear limit, all limits have to be considered separately, and care has to be taken that the soft divergences are not double-counted [see e.g. the divergence structure of $D_0^{(D,\mathrm{mass})}(0,0,s_1,m_Q^2,s,t_1;0,0,0,m_Q)$]. With the same techniques the decomposition of the singular structure of the five-point functions can be obtained. For this purpose in most cases a product of three denominators has to be split by partial fractioning. Again one has to avoid double-counting of soft divergences. For a more detailed description see Ref. [56].

$$
\begin{aligned}
&E_{0,\mathrm{sing}}^{(D,\mathrm{mass})}(0,0,m_Q^2,M_H^2,m_Q^2,s,t_1,s_1,s_2,t_2;0,0,0,m_Q,m_Q) \;=\\
&\qquad \frac{1}{t_{1Q}\,t_{2Q}}\,C_0^{(D,\mathrm{mass})}(0,0,s;0,0,0)+\frac{1}{s\,s_{1Q}}\,C_0^{(D,\mathrm{mass})}(0,m_Q^2,t_1;0,0,m_Q)\\
&\quad +\frac{1}{s\,s_{2Q}}\,C_0^{(D,\mathrm{mass})}(0,m_Q^2,t_2;0,0,m_Q)-\frac{(t_2-s_1)^2}{s\,s_{1Q}\,t_{1Q}\,t_{2Q}}\,C_0^{(D,\mathrm{mass})}(0,s_1,t_2;0,0,m_Q)\\
&\quad -\frac{(t_1-s_2)^2}{s\,s_{2Q}\,t_{1Q}\,t_{2Q}}\,C_0^{(D,\mathrm{mass})}(0,s_2,t_1;0,0,m_Q),\\
&E_{0,\mathrm{sing}}^{(D,\mathrm{mass})}(0,m_Q^2,0,M_H^2,m_Q^2,s,t_1,s_1,s_2,t_2;0,0,m_Q,m_Q,m_Q) \;=\\
&\qquad \frac{1}{t_{1Q}\,t_{2Q}}\,C_0^{(D,\mathrm{mass})}(0,m_Q^2,s;0,0,m_Q)+\frac{1}{s_Q\,s_{2Q}}\,C_0^{(D,\mathrm{mass})}(0,m_Q^2,t_2;0,0,m_Q)\\
&\quad -\frac{(t_1-s_2)^2}{s_Q\,s_{2Q}\,t_{1Q}\,t_{2Q}}\,C_0^{(D,\mathrm{mass})}(0,s_2,t_1;0,0,m_Q),\\
&E_{0,\mathrm{sing}}^{(D,\mathrm{mass})}(m_Q^2,0,M_H^2,0,m_Q^2,s,t_1,s_1,s_2,t_2;0,m_Q,m_Q,m_Q,m_Q) \;=\\
&\qquad \frac{1}{s_Q\,s_{2Q}}\,C_0^{(D,\mathrm{mass})}(m_Q^2,m_Q^2,t_2;m_Q,0,m_Q),\\
&E_{0,\mathrm{sing}}^{(D,\mathrm{mass})}(m_Q^2,0,0,M_H^2,m_Q^2,s,t_1,s_1,s_2,t_2;0,m_Q,m_Q,m_Q,m_Q) \;=\\
&\qquad \frac{1}{s_Q\,s_{2Q}}\,C_0^{(D,\mathrm{mass})}(m_Q^2,m_Q^2,t_2;m_Q,0,m_Q). \qquad \text{(C.18)}
\end{aligned}
$$

Appendix D

Details of the Subtraction Formalism

D.1 The Colour Operators

The definition of the colour operators is adopted from Ref. [61, 63]. The colour operator $\mathbf{T}_i = \{T_i^n\}$ is a vector with respect to the colour index n of the emitted gluon and an $SU(N_c)$ matrix with respect to the colour indices of the parton i. For final-state partons the following relations hold: $T_{cb}^n = \mathrm{i}f_{cnb}$ if i is a gluon, $T_{\alpha\beta}^n = t_{\alpha\beta}^a$ if i is a quark, and $T_{\alpha\beta}^n = -t_{\beta\alpha}^a$ if i is an antiquark. The case of initial-state partons is obtained by crossing: $T_{\alpha\beta}^n = -t_{\beta\alpha}^a$ if i is a quark, and $T_{\alpha\beta}^n = t_{\alpha\beta}^a$ if i is an antiquark. The square of the colour operators are the Casimir operators, $\mathbf{T}_q^2 = C_F$ for a quark and $\mathbf{T}_g^2 = C_A$ for a gluon.

D.2 Final-State Emitter and Final-State Spectator

The formulae in this and the next two sections are taken from Ref. [61] and have been adapted to the case of $Q\bar{Q}H$ production.

In this section the case of the splitting $\widetilde{ji} \to j + i$ with finial-state emitter j together with a final-state spectator k is considered. Since there is only one massless particle in the final state, the index i labeling this massless parton is fixed to $i = 6$ everywhere.

The following auxiliary quantities are defined:

$$Q^\mu = p_i^\mu + p_j^\mu + p_k^\mu, \tag{D.1}$$

$$\mu_Q = \frac{m_Q}{\sqrt{Q^2}}, \tag{D.2}$$

$$\tilde{z}_i = \frac{p_i p_k}{p_i p_k + p_j p_k}, \tag{D.3}$$

$$\tilde{z}_j = \frac{p_j p_k}{p_i p_k + p_j p_k}, \tag{D.4}$$

$$y_{ji,k} = \frac{p_i p_j}{p_i p_j + p_i p_k + p_j p_k}. \tag{D.5}$$

The mapping of the $(m+1)$-particle kinematics onto the m-particle one is given by

$$\begin{aligned}
\tilde{p}^\mu_{ji} &= Q^\mu - \tilde{p}^\mu_k, \\
\tilde{p}^\mu_k &= \frac{\kappa(Q^2, m_Q^2, m_Q^2)}{\kappa(Q^2, (p_i+p_j)^2, m_Q^2)} \left(p^\mu_k - \frac{Q \cdot p_k}{Q^2} Q^\mu \right) + \frac{1}{2} Q^\mu, \\
\tilde{p}^\mu_l &= p^\mu_l,
\end{aligned} \tag{D.6}$$

where l denotes all other particles than i, j, and k, coloured or non-coloured. The momenta fulfill the on-shell conditions $\tilde{p}^2_{ji} = p^2_j = m^2_j = m^2_Q$ and $\tilde{p}^2_k = p^2_k = m^2_k = m^2_Q$.

The following relative velocities $v_{k,q} = \sqrt{1 - k^2 q^2/(k \cdot q)}$ are needed:

$$\tilde{v}_{ji,k} = \frac{\sqrt{1-4\mu_Q^2}}{1-2\mu_Q^2}, \qquad v_{ji,k} = \frac{\kappa(Q^2, (p_i+p_j)^2, m_Q^2)}{Q^2 - 2\mu_Q^2}. \tag{D.7}$$

The only needed case of $\mathbf{V}_{ji,k}$ for $Q\bar{Q}H$ production is the splitting $Q_{ji} \to Q_j + g_i$ and $\bar{Q}_{ji} \to \bar{Q}_j + g_i$:

$$\mathbf{V}_{Q_j g_i, k} = \mathbf{V}_{\bar{Q}_j g_i, k} = 8\pi\alpha_s \left\{ \frac{2}{1 - \tilde{z}_j(1 - y_{ji,k})} - \frac{\tilde{v}_{ji,k}}{v_{ji,k}} \left[1 + \tilde{z}_j + \frac{m_Q^2}{p_i p_j} \right] \right\}. \tag{D.8}$$

The integral for the endpoint in Eq. (4.32) is split into a general part I_{eik} and a splitting specific part $I^{\text{rem}}_{Q_j g_i, k}$:

$$\begin{aligned}
I_{\text{eik}}(\mu_Q) &= \frac{1}{\tilde{v}_{ji,k}} \Bigg[\Delta_1(s_{jk}) \ln(\mu_Q \hat{x}) + \ln\left(\frac{(1-2\mu_Q^2)^2 \tilde{v}^2_{ji,k} \hat{x}^3}{\mu_Q} \right) \ln(\mu_Q \hat{x}) \\
&\quad - \frac{1}{2} \ln^2\left[(1-2\mu_Q^2)\hat{x}^2 y_+ \right] + \mathrm{Li}_2\left(\mu_Q^2 \hat{x}^2 \right) - \mathrm{Li}_2\left(-\frac{\mu_Q^2}{(1-2\mu_Q^2) y_+} \right) \\
&\quad - \frac{\pi^2}{3} + J(\mu_Q) \Bigg], \\
J(\mu_Q) &= \mathrm{Li}_2\left(1 - \frac{\mu_Q^2}{(1-\mu_Q^2\hat{x})^2} \right) - 2\,\mathrm{Li}_2\left(1 - \hat{x} + \mu_Q \hat{x} \right) + 2\,\mathrm{Li}_2\left(-\frac{\mu_Q^3 \hat{x}^2}{1-\mu_Q^2\hat{x}} \right) \\
&\quad - 2\,\mathrm{Li}_2\left(\hat{x} - \frac{\mu_Q \hat{x}}{1-\mu_Q^2\hat{x}} \right) + 2 \ln\left(\frac{\mu_Q}{1-\mu_Q^2\hat{x}} \right) \ln\left(1 + \frac{\mu_Q}{1-\mu_Q^2\hat{x}} \right) + \frac{\pi^2}{6}, \\
I^{\text{rem}}_{Q_j g_i, k}(\mu_Q) &= \Delta_1(s_{jk}) - 2 \ln\left(\frac{1-2\mu_Q}{1-\mu_Q} \right) + \frac{1-4\mu_Q^2}{1-2\mu_Q^2} \ln\left(\frac{\mu_Q}{1-\mu_Q} \right) + 3 \\
&\quad - \frac{\mu_Q}{1-\mu_Q} - \frac{2\mu_Q(1-2\mu_Q)}{1-2\mu_Q^2}.
\end{aligned} \tag{D.9}$$

The abbreviations $\hat{x}$ and y_+ are defined as follows:

$$\hat{x} = \frac{2}{1+\sqrt{1-4\mu_Q^2}}, \qquad y_+ = 1-2\mu_Q\frac{1-\mu_Q}{1-2\mu_Q^2}. \tag{D.10}$$

Since the mapping $p_l \to \tilde{p}_l$ simplifies for the endpoint contribution to $p_i = 0$ and $\tilde{p}_l = p_l$ for $l \neq i$, the quantity μ_Q in Eq. (D.9) can be written as

$$\mu_Q^2 = \frac{m_Q^2}{(p_j+p_k)^2} = \frac{m_Q^2}{s_{jk}}, \tag{D.11}$$

as already stated in Eq. (4.35).

D.3 Final-State Emitter and Initial-State Spectator

In this section the same splitting as in the previous one is considered but together with an initial-state spectator a. The following auxiliary quantities are defined:

$$Q^\mu = p_i^\mu + p_j^\mu - p_a^\mu, \tag{D.12}$$

$$\mu_Q = \frac{m_Q}{\sqrt{2\tilde{p}_{ji}p_a}}, \tag{D.13}$$

$$x_{ji,a} = \frac{p_a p_i + p_a p_j - p_i p_j}{p_a p_i + p_a p_j}, \tag{D.14}$$

$$\tilde{z}_i = \frac{p_a p_i}{p_a p_i + p_a p_j}, \tag{D.15}$$

$$\tilde{z}_j = \frac{p_a p_j}{p_a p_i + p_a p_j}. \tag{D.16}$$

The mapping $p_l \to \tilde{p}_l$ is given by:

$$\begin{aligned} \tilde{p}_a^\mu &= x_{ji,a}\, p_a^\mu, \\ \tilde{p}_{ji}^\mu &= p_i^\mu + p_j^\mu - (1-x_{ji,a})\, p_a^\mu, \\ \tilde{p}_l^\mu &= p_l^\mu, \end{aligned} \tag{D.17}$$

where l denotes all other particles than a, i, and j, coloured or non-coloured. The momenta fulfill the on-shell conditions $\tilde{p}_{ji}^2 = p_j^2 = m_j^2 = m_Q^2$ and $\tilde{p}_a^2 = p_a^2 = 0$.

As in the case of final-state emitter and final-state spectator, the only case needed is the splitting $Q_{ji} \to Q_j + g_i$ and $\bar{Q}_{ji} \to \bar{Q}_j + g_i$. Whether the spectator is a gluon or a massless quark does not affect $\mathbf{V}_{ji}^a$:

$$\mathbf{V}_{Q_j g_i}^a = \mathbf{V}_{\bar{Q}_j g_i}^a = 8\pi\alpha_s \left\{ \frac{2}{2-x_{ji,a}-\tilde{z}_j} - 1 - \tilde{z}_j - \frac{m_Q^2}{p_i p_j} \right\}. \tag{D.18}$$

The endpoint contribution is given by:

$$\begin{aligned}\mathcal{J}^{a}_{Q_j g_i} &= \left[1+\ln\left(\mu_Q^2\right)-\ln\left(1+\mu_Q^2\right)\right]\Delta_1(m_Q^2-t_{aj})-\frac{1}{2}\ln^2\left(\mu_Q^2\right)-\frac{1}{2}\ln\left(\mu_Q^2\right)\\ &\quad-\frac{1}{2}\ln^2\left(1+\mu_Q^2\right)+\frac{1}{2}\ln\left(1+\mu_Q^2\right)-2\,\mathrm{Li}_2\left(\frac{1}{1+\mu_Q^2}\right)-2\,\mathrm{Li}_2\left(-\mu_Q^2\right)\\ &\quad+\frac{3}{2}-\frac{1}{3}\pi^2+\frac{\mu_Q^2}{2\left(1+\mu_Q^2\right)}. \end{aligned} \tag{D.19}$$

For the endpoint with $x=1$ the definition for μ_Q simplifies to

$$\mu_Q^2 = \frac{m_Q^2}{2p_a\cdot p_j}=\frac{m_Q^2}{m_Q^2-t_{aj}}, \tag{D.20}$$

as already stated in Eq. (4.34).

D.4 Initial-State Emitter and Final-State Spectator

The kinematical situation is governed by the previous section after replacing $\tilde{p}_a \to \tilde{p}_{ai}$ and $\tilde{p}_{ji} \to \tilde{p}_j$.

The needed dipole functions for the splitting $a \to i + \widetilde{ai}$ contains spin correlations if the parton $\widetilde{ai}$ is a gluon,

$$\begin{aligned}\mathbf{V}_j^{q_a g_i} &= 8\pi\alpha_s\left\{\frac{2}{2-x_{ji,a}-\tilde{z}_j}-1-x_{ji,a}\right\},\\ \mathbf{V}_j^{g_a q_i} &= 8\pi\alpha_s\frac{T_R}{C_F}\left\{1-2x_{ji,a}(1-x_{ji,a})\right\},\\ \mathbf{V}_j^{q_a q_i,\mu\nu} &= 8\pi\alpha_s\frac{C_F}{C_A}\left\{-g^{\mu\nu}x_{ji,a}+\frac{1-x_{ji,a}}{x_{ji,a}}\frac{2\tilde{z}_i\tilde{z}_j}{p_ip_j}\left(\frac{p_i^\mu}{\tilde{z}_i}-\frac{p_j^\mu}{\tilde{z}_j}\right)\left(\frac{p_i^\nu}{\tilde{z}_i}-\frac{p_j^\nu}{\tilde{z}_j}\right)\right\},\\ \mathbf{V}_j^{g_a g_i,\mu\nu} &= 8\pi\alpha_s\left\{-2g^{\mu\nu}\left[\frac{1}{2-x_{ji,a}-\tilde{z}_j}-1+x_{ji,a}(1-x_{ji,a})\right]\right.\\ &\qquad\left.+\frac{1-x_{ji,a}}{x_{ji,a}}\frac{2\tilde{z}_i\tilde{z}_j}{p_ip_j}\left(\frac{p_i^\mu}{\tilde{z}_i}-\frac{p_j^\mu}{\tilde{z}_j}\right)\left(\frac{p_i^\nu}{\tilde{z}_i}-\frac{p_j^\nu}{\tilde{z}_j}\right)\right\}. \end{aligned} \tag{D.21}$$

These relations also hold if a quark is replaced by an anti-quark wherever this is possible.

The endpoint is given by:

$$\begin{aligned}\mathcal{J}_j^{ai} &= \Delta_2(m_Q^2-t_{aj})+\left[\frac{\gamma_a}{\mathbf{T}_a^2}+\ln\left(1+\mu_Q^2\right)\right]\Delta_1(m_Q^2-t_{aj})\\ &\quad+\frac{1}{2}\ln^2\left(1+\mu_Q^2\right)+2\,\mathrm{Li}_2\left(\frac{1}{1+\mu_Q^2}\right)-\frac{1}{3}\pi^2. \end{aligned} \tag{D.22}$$

The γ_a are defined in Eq. (4.36). The endpoint $\mathcal{J}_j^a$ given in Eq. (4.32) is the sum of the two endpoints in Eq. (D.19) and Eq. (D.22).

D.5 Initial-State Emitter and Initial-State Spectator

The formulae in this section are taken from Ref. [63]. The following auxiliary quantities are defined:

$$
\begin{aligned}
Q^\mu &= p_a^\mu + p_b^\mu - p_i^\mu, && \text{(D.23)}\\
\widetilde{Q}^\mu &= \tilde{p}_{ai}^\mu + p_b^\mu, && \text{(D.24)}\\
x_{i,ab} &= \frac{p_a p_b - p_i p_a - p_i p_b}{p_a p_b}. && \text{(D.25)}
\end{aligned}
$$

For the mapping of the momenta the momentum of the spectator b is fixed but all other momenta p_l change:

$$
\begin{aligned}
\tilde{p}_{ai}^\mu &= x_{i,ab}\, p_a^\mu,\\
\tilde{p}_b^\mu &= p_b^\mu,\\
\tilde{p}_l^\mu &= p_l^\mu - \frac{2p_l\cdot(Q+\widetilde{Q})}{(Q+\widetilde{Q})^2}\,(Q^\mu+\widetilde{Q}^\mu) + \frac{2p_l\cdot Q}{Q^2}\,\widetilde{Q}^\mu. && \text{(D.26)}
\end{aligned}
$$

The momenta fulfill the on-shell conditions $\tilde{p}_a^2 = p_a^2 = 0$ and $\tilde{p}_l^2 = p_l^2 = m_l^2$.

The needed dipole functions for the splitting $a \to i + \widetilde{ai}$ contain spin correlations if the parton $\widetilde{ai}$ is a gluon,

$$
\begin{aligned}
\mathbf{V}^{q_a g_i, b} &= 8\pi\alpha_s \left\{ \frac{2}{1-x_{i,ab}} - (1+x_{i,ab}) \right\},\\
\mathbf{V}^{g_a q_i, b} &= 8\pi\alpha_s \frac{T_R}{C_F} \left\{ 1 - 2x_{i,ab}(1-x_{i,ab}) \right\},\\
\mathbf{V}^{q_a q_i, b, \mu\nu} &= 8\pi\alpha_s \frac{C_F}{C_A} \Bigg\{ - g^{\mu\nu} x_{i,ab}\\
&\qquad + \frac{1-x_{i,ab}}{x_{i,ab}} \frac{2(p_a p_b)(p_a p_i)}{p_b p_i} \left(\frac{p_i^\mu}{p_a p_i} - \frac{p_b^\mu}{p_a p_b} \right) \left(\frac{p_i^\nu}{p_a p_i} - \frac{p_b^\nu}{p_a p_b} \right) \Bigg\},\\
\mathbf{V}^{g_a g_i, b, \mu\nu} &= 8\pi\alpha_s \Bigg\{ - 2g^{\mu\nu} \left[\frac{1}{1-x_{i,ab}} - 1 + x_{i,ab}(1-x_{i,ab}) \right]\\
&\qquad + \frac{1-x_{i,ab}}{x_{i,ab}} \frac{2(p_a p_b)(p_a p_i)}{p_b p_i} \left(\frac{p_i^\mu}{p_a p_i} - \frac{p_b^\mu}{p_a p_b} \right) \left(\frac{p_i^\nu}{p_a p_i} - \frac{p_b^\nu}{p_a p_b} \right) \Bigg\}.
\end{aligned}
\qquad \text{(D.27)}
$$

These relations also hold if a quark is replaced by an anti-quark wherever this is possible.

Bibliography

[1] S. L. Glashow, "Partial Symmetries of Weak Interactions", *Nucl. Phys.* **22** (1961) 579–588.

[2] A. Salam, "Weak and Electromagnetic Interactions". Originally printed in "Svartholm: Elementary Particle Theory, Proceedings of the Nobel Symposium Held 1968 at Lerum, Sweden", Stockholm 1968, 367-377.

[3] S. Weinberg, "A Model of Leptons", *Phys. Rev. Lett.* **19** (1967) 1264–1266.

[4] M. Gell-Mann, "A Schematic Model of Baryons and Mesons", *Phys. Lett.* **8** (1964) 214–215.

[5] G. Zweig, "An SU(3) Model for Strong Interaction Symmetry and its Breaking". In "Lichtenberg, D. B. (Ed.), Rosen, S. P. (Ed.): Developments in the Quark Theory of Hadrons, Vol. 1", 22-101 and CERN Geneva - TH. 401 (rec. Jan. 1964) 24p.

[6] O. W. Greenberg, "Spin and Unitary Spin Independence in a Paraquark Model of Baryons and Mesons", *Phys. Rev. Lett.* **13** (1964) 598–602.

[7] M. Y. Han and Y. Nambu, "Three-Triplet Model with Double SU(3) Symmetry", *Phys. Rev.* **139** (1965) B1006–B1010.

[8] H. Fritzsch and M. Gell-Mann, "Current Algebra: Quarks and What Else?", in *Proceedings XVI International Conference on High Energy Physics*, p. 135. Chicago, 1972.

[9] H. Fritzsch, M. Gell-Mann, and H. Leutwyler, "Advantages of the Color Octet Gluon Picture", *Phys. Lett.* **B47** (1973) 365–368.

[10] H. Spiesberger, M. Spira, and P. M. Zerwas, "The Standard Model: Physical Basis and Scattering Experiments", `hep-ph/0011255`. Published in "Scattering", P. Sabatier, editor. Academic Press, London, 2000.

[11] **LEP** Collaboration, "A Combination of Preliminary Electroweak Measurements and Constraints on the Standard Model", `hep-ex/0103048`.

[12] P. W. Higgs, "Broken Symmetries, Massless Particles and Gauge Fields", *Phys. Lett.* **12** (1964) 132–133.

[13] P. W. Higgs, "Broken Symmetries and the Masses of Gauge Bosons", *Phys. Rev. Lett.* **13** (1964) 508–509.

[14] P. W. Higgs, "Spontaneous Symmetry Breakdown without Massless Bosons", *Phys. Rev.* **145** (1966) 1156–1163.

[15] F. Englert and R. Brout, "Broken Symmetry and the Mass of Gauge Vector Mesons", *Phys. Rev. Lett.* **13** (1964) 321–322.

[16] G. S. Guralnik, C. R. Hagen, and T. W. B. Kibble, "Global Conservation Laws and Massless Particles", *Phys. Rev. Lett.* **13** (1964) 585–587.

[17] T. W. B. Kibble, "Symmetry Breaking in Non-Abelian Gauge Theories", *Phys. Rev.* **155** (1967) 1554–1561.

[18] M. Spira and P. M. Zerwas, "Electroweak Symmetry Breaking and Higgs Physics", `hep-ph/9803257`. Lectures given at 36th Internationale Universitätswochen für Kernphysik und Teilchenphysik: Nuclear and Particle Physics): Computing Particle Properties (36 IUKT), Schladming, Austria, 1-8 Mar 1997.

[19] B. A. Kniehl, "Theoretical Aspects of Standard-Model Higgs-Boson Physics at a Future e^+e^- Linear Collider", `hep-ph/0112023`.

[20] M. Carena *et al.*, "Report of the Tevatron Higgs Working Group", `hep-ph/0010338`.

[21] "ATLAS: Detector and Physics Performance. Technical Design Report. Vol. 1". CERN-LHCC-99-14.

[22] "ATLAS: Detector and Physics Performance. Technical Design Report. Vol. 2". CERN-LHCC-99-15.

[23] "CMS, the Compact Muon Solenoid: Technical Proposal". CERN-LHCC-94-38.

[24] **LEP Higgs Working Group for Higgs Boson Searches** Collaboration, "Search for the Standard Model Higgs Boson at LEP", `hep-ex/0107029`.

[25] T. Kawamoto, "Electroweak Data and Standard Model Fit Results", `hep-ex/0105032`.

[26] E. Tournefier, "Electroweak Results from LEP and SLC and Tests of the Standard Model", `hep-ex/0105091`.

[27] J. A. Bagger, A. F. Falk, and M. Swartz, "Precision Observables and Electroweak Theories", *Phys. Rev. Lett.* **84** (2000) 1385–1388, `hep-ph/9908327`.

[28] M. E. Peskin and J. D. Wells, "How can a heavy Higgs Boson be consistent with the Precision Electroweak Measurements?", *Phys. Rev.* **D64** (2001) 093003, hep-ph/0101342.

[29] M. S. Chanowitz, "The $Z \to \bar{b}b$ Decay Asymmetry: Lose-Lose for the Standard Model", hep-ph/0104024.

[30] H. M. Georgi, S. L. Glashow, M. E. Machacek, and D. V. Nanopoulos, "Higgs Bosons from Two Gluon Annihilation in Proton–Proton Collisions", *Phys. Rev. Lett.* **40** (1978) 692.

[31] A. Djouadi, M. Spira, and P. M. Zerwas, "Production of Higgs Bosons in Proton Colliders: QCD Corrections", *Phys. Lett.* **B264** (1991) 440–446.

[32] M. Spira, A. Djouadi, D. Graudenz, and P. M. Zerwas, "Higgs Boson Production at the LHC", *Nucl. Phys.* **B453** (1995) 17–82, hep-ph/9504378.

[33] R. N. Cahn and S. Dawson, "Production of Very Massive Higgs Bosons", *Phys. Lett.* **B136** (1984) 196.

[34] G. Altarelli, B. Mele, and F. Pitolli, "Heavy Higgs Production at Future Colliders", *Nucl. Phys.* **B287** (1987) 205–224.

[35] T. Han, G. Valencia, and S. Willenbrock, "Structure Function Approach to Vector Boson Scattering in pp Collisions", *Phys. Rev. Lett.* **69** (1992) 3274–3277, hep-ph/9206246.

[36] D. Rainwater, D. Zeppenfeld, and K. Hagiwara, "Searching for $H \to \tau\tau$ in Weak Boson Fusion at the LHC", *Phys. Rev.* **D59** (1999) 014037, hep-ph/9808468.

[37] S. L. Glashow, D. V. Nanopoulos, and A. Yildiz, "Associated Production of Higgs Bosons and Z Particles", *Phys. Rev.* **D18** (1978) 1724–1727.

[38] Z. Kunszt, Z. Trocsanyi, and W. J. Stirling, "Clear Signal of Intermediate Mass Higgs Boson Production at LHC and SSC", *Phys. Lett.* **B271** (1991) 247–255.

[39] T. Han and S. Willenbrock, "QCD Correction to the $pp \to WH$ and ZH Total Cross-Sections", *Phys. Lett.* **B273** (1991) 167–172.

[40] Z. Kunszt, "Associated Production of Heavy Higgs Boson with Top Quarks", *Nucl. Phys.* **B247** (1984) 339.

[41] W. J. Marciano and F. E. Paige, "Associated Production of Higgs Bosons with $t\bar{t}$ Pairs", *Phys. Rev. Lett.* **66** (1991) 2433–2435.

[42] J. F. Gunion, "Associated Top Anti-Top Higgs Production as a Large Source of W H Events: Implications for Higgs Detection in the Lepton Neutrino Gamma Gamma Final State", *Phys. Lett.* **B261** (1991) 510–517.

[43] A. Djouadi, M. Spira, and P. M. Zerwas, "QCD Corrections to Hadronic Higgs Decays", *Z. Phys.* **C70** (1996) 427–434, hep-ph/9511344.

[44] M. Spira, "QCD Effects in Higgs Physics", *Fortsch. Phys.* **46** (1998) 203–284, hep-ph/9705337.

[45] V. Drollinger, T. Müller, and D. Denegri, "Searching for Higgs Bosons in Association with Top Quark Pairs in the $H \to b\bar{b}$ Decay Mode", hep-ph/0111312.

[46] J. Goldstein *et al.*, "$p\bar{p} \to t\bar{t}H$: A Discovery Mode for the Higgs Boson at the TEVATRON", *Phys. Rev. Lett.* **86** (2001) 1694–1697, hep-ph/0006311.

[47] M. Carena, S. Mrenna, and C. E. M. Wagner, "MSSM Higgs Boson Phenomenology at the Tevatron Collider", *Phys. Rev.* **D60** (1999) 075010, hep-ph/9808312.

[48] M. Beneke *et al.*, "Top Quark Physics", hep-ph/0003033.

[49] A. Djouadi, J. Kalinowski, and P. M. Zerwas, "Higgs Radiation off Top Quarks in High-Energy e^+e^- Colliders", *Z. Phys.* **C54** (1992) 255–262.

[50] S. Dittmaier, M. Krämer, Y. Liao, M. Spira, and P. M. Zerwas, "Higgs Radiation off Top Quarks in e^+e^- Collisions", *Phys. Lett.* **B441** (1998) 383–388, hep-ph/9808433.

[51] S. Dawson and L. Reina, "QCD Corrections to Associated Higgs Boson-Heavy Quark Production", *Phys. Rev.* **D59** (1999) 054012, hep-ph/9808443.

[52] S. Dawson and L. Reina, "Associated Higgs Production in the MSSM", *Phys. Rev.* **D60** (1999) 015003, hep-ph/9812488.

[53] S. Dittmaier, M. Krämer, Y. Liao, M. Spira, and P. M. Zerwas, "Higgs Radiation off Quarks in Supersymmetric Theories at e^+e^- Colliders", *Phys. Lett.* **B478** (2000) 247–254, hep-ph/0002035.

[54] S. Dawson and L. Reina, "QCD Corrections to Associated Higgs Boson Production", *Phys. Rev.* **D57** (1998) 5851–5859, hep-ph/9712400.

[55] W. Beenakker, S. Dittmaier, M. Krämer, B. Plümper, M. Spira, and P. M. Zerwas, "Higgs Radiation off Top Quarks at the TEVATRON and the LHC", *Phys. Rev. Lett.* **87** (2001) 201805, hep-ph/0107081.

[56] W. Beenakker, S. Dittmaier, M. Krämer, B. Plümper, M. Spira, and P. M. Zerwas, "NLO QCD Corrections to $t\bar{t}H$ Production in Hadron Collisions." In preparation.

[57] L. Reina and S. Dawson, "Next-to-Leading Order Results for $t\bar{t}H$ Production at the TEVATRON", hep-ph/0107101.

[58] L. Reina, S. Dawson, and D. Wackeroth, "QCD Corrections to Associated $t\bar{t}H$ Production at the TEVATRON", `hep-ph/0109066`.

[59] Z. Bern, L. J. Dixon, and D. A. Kosower, "Dimensionally Regulated One-Loop Integrals", *Phys. Lett.* **B302** (1993) 299–308, `hep-ph/9212308`.

[60] Z. Bern, L. J. Dixon, and D. A. Kosower, "Dimensionally Regulated Pentagon Integrals", *Nucl. Phys.* **B412** (1994) 751–816, `hep-ph/9306240`.

[61] S. Catani, S. Dittmaier, M. H. Seymour, and Z. Trocsanyi, "The Dipole Formalism for NLO QCD Calculations with Massive Partons", `hep-ph/0201036`.

[62] S. Catani and M. H. Seymour, "The Dipole Formalism for the Calculation of QCD Jet Cross Sections at Next-to-Leading Order", *Phys. Lett.* **B378** (1996) 287–301, `hep-ph/9602277`.

[63] S. Catani and M. H. Seymour, "A General Algorithm for Calculating Jet Cross Sections in NLO QCD", *Nucl. Phys.* **B485** (1997) 291–419, `hep-ph/9605323`. [Erratum-ibid. **B510** (1997) 503].

[64] C. Itzykson and J.-B. Zuber, *Quantum Field Theory*. McGraw-Hill, 1980.

[65] O. Nachtmann, *Phänomene und Konzepte der Elementarteilchenphysik*. Vieweg, 1986.

[66] R. K. Ellis, W. J. Stirling, and B. R. Webber, *QCD and Collider Physics*. Cambridge Univ. Press, 1996.

[67] M. Böhm, A. Denner, and H. Joos, *Gauge Theories of the Strong and Electroweak Interaction*. B.G. Teubner Verlag, 3. rev. ed., 2001.

[68] C. S. Wu, E. Ambler, R. W. Hayward, D. D. Hoppes, and R. P. Hudson, "Experimental Test of Parity Conservation in Beta Decay", *Phys. Rev.* **105** (1957) 1413–1414.

[69] **SuperKamiokande** Collaboration, Y. Fukuda *et al.*, "Measurement of the Flux and Zenith-Angle Distribution of Upward Through-Going Muons by Super-Kamiokande", *Phys. Rev. Lett.* **82** (1999) 2644–2648, `hep-ex/9812014`.

[70] **SNO** Collaboration, Q. R. Ahmad *et al.*, "Measurement of the Rate of $\nu_e + d \to p + p + e$ Interactions Produced by B-8 Solar Neutrinos at the Sudbury Neutrino Observatory", *Phys. Rev. Lett.* **87** (2001) 071301, `nucl-ex/0106015`.

[71] Y. Nambu, "Axial Vector Current Conservation in Weak Interactions", *Phys. Rev. Lett.* **4** (1960) 380–382.

[72] J. Goldstone, "Field Theories with 'Superconductor' Solutions", *Nuovo Cim.* **19** (1961) 154–164.

[73] J. Goldstone, A. Salam, and S. Weinberg, "Broken Symmetries", *Phys. Rev.* **127** (1962) 965–970.

[74] N. Cabibbo, "Unitary Symmetry and Leptonic Decays", *Phys. Rev. Lett.* **10** (1963) 531–532.

[75] M. Kobayashi and T. Maskawa, "CP Violation in the Renormalizable Theory of Weak Interaction", *Prog. Theor. Phys.* **49** (1973) 652.

[76] B. Plümper, *Renormierung und Skalenabhängigkeit der Cabibbo-Kobayashi-Maskawa-Matrix*. Diploma thesis, Universität Karlsruhe, 1998.

[77] G. 't Hooft and M. Veltman, "Regularization and Renormalization of Gauge Fields", *Nucl. Phys.* **B44** (1972) 189–213.

[78] C. G. Bollini and J. J. Giambiagi, "Lowest Order Divergent Graphs in ν-Dimensional Space", *Phys. Lett.* **B40** (1972) 566–568.

[79] T. Kinoshita, "Mass Singularities of Feynman Amplitudes", *J. Math. Phys.* **3** (1962) 650–677.

[80] T. D. Lee and M. Nauenberg, "Degenerate Systems and Mass Singularities", *Phys. Rev.* **133** (1964) B1549–B1562.

[81] G. Sterman and S. Weinberg, "Jets from Quantum Chromodynamics", *Phys. Rev. Lett.* **39** (1977) 1436.

[82] Y. L. Dokshitzer, D. Diakonov, and S. I. Troian, "Hard Processes in Quantum Chromodynamics", *Phys. Rept.* **58** (1980) 269–395.

[83] G. 't Hooft, "Renormalization of Massless Yang-Mills Fields", *Nucl. Phys.* **B33** (1971) 173–199.

[84] G. 't Hooft, "Renormalizable Lagrangians for Massive Yang-Mills Fields", *Nucl. Phys.* **B35** (1971) 167–188.

[85] D. A. Ross and J. C. Taylor, "Renormalization of a Unified Theory of Weak and Electromagnetic Interactions", *Nucl. Phys.* **B51** (1973) 125–144. [Erratum-ibid. **B58** (1973) 643].

[86] K. I. Aoki, Z. Hioki, R. Kawabe, M. Konuma, and T. Muta, "One-Loop Corrections to νe Scattering in Weinberg–Salam Theory: Neutral Current Processes", *Prog. Theor. Phys.* **64** (1980) 707.

[87] K. I. Aoki, Z. Hioki, R. Kawabe, M. Konuma, and T. Muta, "Electroweak Radiative Corrections to High-Energy νe Scatterings", *Prog. Theor. Phys.* **65** (1981) 1001.

[88] K. I. Aoki, Z. Hioki, M. Konuma, R. Kawabe, and T. Muta, "Electroweak Theory. Framework of On-Shell Renormalization and Study of Higher-Order Effects", *Prog. Theor. Phys. Suppl.* **73** (1982) 1–225.

[89] A. Denner, "Techniques for Calculation of Electroweak Radiative Corrections at the One-Loop Level and Results for W Physics at LEP200", *Fortschr. Phys.* **41** (1993) 307–420.

[90] W. A. Bardeen, A. J. Buras, D. W. Duke, and T. Muta, "Deep Inelastic Scattering Beyond the Leading Order in Asymptotically Free Gauge Theories", *Phys. Rev.* **D18** (1978) 3998.

[91] G. 't Hooft, "Dimensional Regularization and the Renormalization Group", *Nucl. Phys.* **B61** (1973) 455–468.

[92] D. J. Gross and F. Wilczek, "Asymptotically Free Gauge Theories I", *Phys. Rev.* **D8** (1973) 3633–3652.

[93] H. D. Politzer, "Asymptotic Freedom: an Approach to Strong Interactions", *Phys. Rept.* **14** (1974) 129–180.

[94] H. Lehmann, K. Symanzik, and W. Zimmermann, "On the Formulation of Quantized Field Theories", *Nuovo Cim.* **1** (1955) 205–225.

[95] A. D. Martin, R. G. Roberts, and W. J. Stirling, "Parton Distributions: A Study of the New HERA Data, alpha(s), the Gluon and P Anti-P Jet Production", *Phys. Lett.* **B387** (1996) 419–426, `hep-ph/9606345`.

[96] **H1 and ZEUS** Collaboration, D. Wegener, "The Parton Structure of Protons and Photons Measured at the *ep* Storage Ring HERA", *Nucl. Phys.* **A680** (2000) 184–195.

[97] J. C. Collins, D. E. Soper, and G. Sterman, "Factorization of Hard Processes in QCD", *Adv. Ser. Direct. High Energy Phys.* **5** (1988) 1–91. Published in "Perturbative QCD", A.H. Mueller (ed.), World Scientific Publ., 1989.

[98] W. Furmanski and R. Petronzio, "Lepton–Hadron Processes Beyond Leading Order in Quantum Chromodynamics", *Zeit. Phys.* **C11** (1982) 293.

[99] G. Altarelli, R. K. Ellis, and G. Martinelli, "Large Perturbative Corrections to the Drell-Yan Process in QCD", *Nucl. Phys.* **B157** (1979) 461.

[100] G. Altarelli and G. Parisi, "Asymptotic Freedom in Parton Language", *Nucl. Phys.* **B126** (1977) 298.

[101] **Particle Data Group** Collaboration, D. E. Groom *et al.*, "Review of Particle Physics", *Eur. Phys. J.* **C15** (2000) 1.

[102] **CTEQ** Collaboration, J. Botts *et al.*, "CTEQ Parton Distributions and Flavor Dependence of Sea Quarks", *Phys. Lett.* **B304** (1993) 159–166, `hep-ph/9303255`.

[103] G. Passarino and M. J. G. Veltman, "One Loop Corrections for e^+e^- Annihilation into $\mu^+\mu^-$ in the Weinberg Model", *Nucl. Phys.* **B160** (1979) 151.

[104] D. B. Melrose, "Reduction of Feynman Diagrams", *Nuovo Cim.* **40** (1965) 181–213.

[105] A. Denner, S. Dittmaier, and M. Roth, "Non-Factorizable Photonic Corrections to $e^+e^- \to WW \to 4$ fermions", *Nucl. Phys.* **B519** (1998) 39–84, `hep-ph/9710521`.

[106] S. Dittmaier, "A General Approach to Photon Radiation off Fermions", *Nucl. Phys.* **B565** (2000) 69–122, `hep-ph/9904440`.

[107] S. Catani, S. Dittmaier, and Z. Trocsanyi, "One-Loop Singular Behaviour of QCD and SUSY QCD Amplitudes With Massive Partons", *Phys. Lett.* **B500** (2001) 149–160, `hep-ph/0011222`.

[108] A. Sommerfeld, *Atombau und Spektrallinien*, vol. II, p. 457. F. Vieweg und Sohn, Braunschweig, 1939.

[109] T. Stelzer and W. F. Long, "Automatic Generation of Tree Level Helicity Amplitudes", *Comput. Phys. Commun.* **81** (1994) 357–371, `hep-ph/9401258`.

[110] H. Murayama, I. Watanabe, and K. Hagiwara, "HELAS: HELicity Amplitude Subroutines for Feynman Diagram Evaluations". KEK-91-11.

[111] H. Weyl, *The Theory of Groups and Quantum Mechanics*. Dover, New York, 1931.

[112] B. L. van der Waerden, *Group Theory and Quantum Mechanics*. Springer-Verlag, Berlin, 1974.

[113] P. A. Carruthers, *Spin and Isospin in Particle Physics*. Gordon and Breach Science Publishers, New York, 1971.

[114] F. A. Berends and W. Giele, "The Six Gluon Process as an Example of Weyl-van der Waerden Spinor Calculus", *Nucl. Phys.* **B294** (1987) 700.

[115] F. A. Berends, W. T. Giele, and H. Kuijf, "Exact Expressions for Processes Involving a Vector Boson and up to Five Partons", *Nucl. Phys.* **B321** (1989) 39.

[116] W. T. Giele, *Properties and Calculations of Multiparton Processes*. PhD thesis, University of Leiden, 1989.

[117] H. Kuijf, *Multiparton Production at Hadron Colliders*. PhD thesis, University of Leiden, 1991.

[118] S. Dittmaier, *Gauge-Boson Production in Electron-Photon Collisions*. PhD thesis, University of Würzburg, 1993.

[119] S. Dittmaier, "Weyl-van-der-Waerden Formalism for Helicity Amplitudes of Massive Particles", *Phys. Rev.* **D59** (1999) 016007, `hep-ph/9805445`.

[120] E. Byckling and K. Kajantie, *Particle Kinematics*. Wiley, 1973.

[121] B. W. Harris and J. F. Owens, "The Two Cutoff Phase Space Slicing Method", `hep-ph/0102128`.

[122] A. Bassetto, M. Ciafaloni, and G. Marchesini, "Jet Structure and Infrared Sensitive Quantities in Perturbative QCD", *Phys. Rept.* **100** (1983) 201–272.

[123] Y. L. Dokshitzer, V. A. Khoze, A. H. Mueller, and S. I. Troian, *Basics of Perturbative QCD*. Editions Frontieres. Gif-sur-Yvette, 1991.

[124] R. K. Ellis, D. A. Ross, and A. E. Terrano, "The Perturbative Calculation of Jet Structure in e^+e^- Annihilation", *Nucl. Phys.* **B178** (1981) 421.

[125] S. D. Ellis, Z. Kunszt, and D. E. Soper, "The One Jet Inclusive Cross Section at Order α_s^3. 1. Gluons Only", *Phys. Rev.* **D40** (1989) 2188.

[126] Z. Kunszt and D. E. Soper, "Calculation of Jet Cross Sections in Hadron Collisions at Order α_s^3", *Phys. Rev.* **D46** (1992) 192–221.

[127] S. Frixione, Z. Kunszt, and A. Signer, "Three-Jet Cross Sections to Next-to-Leading Order", *Nucl. Phys.* **B467** (1996) 399–442, `hep-ph/9512328`.

[128] Z. Nagy and Z. Trocsanyi, "Calculation of QCD Jet Cross Sections at Next-to-Leading Order", *Nucl. Phys.* **B486** (1997) 189–226, `hep-ph/9610498`.

[129] L. Phaf and S. Weinzierl, "Dipole Formalism with Heavy Fermions", *JHEP* **04** (2001) 006, `hep-ph/0102207`.

[130] T. O. Eynck, E. Laenen, L. Phaf, and S. Weinzierl, "Comparison of Phase Space Slicing and Dipole Subtraction Methods for $\gamma^* \to Q\bar{Q}$", `hep-ph/0109246`.

[131] W. Beenakker, H. Kuijf, W. L. van Neerven, and J. Smith, "QCD Corrections to Heavy Quark Production in $p\bar{p}$ Collisions", *Phys. Rev.* **D40** (1989) 54–82.

[132] P. Nason, S. Dawson, and R. K. Ellis, "The Total Cross Section for the Production of Heavy Quarks in Hadronic Collisions", *Nucl. Phys.* **B303** (1988) 607.

[133] P. Nason, S. Dawson, and R. K. Ellis, "The One Particle Inclusive Differential Cross Section for Heavy Quark Production in Hadronic Collisions", *Nucl. Phys.* **B327** (1989) 49–92.

[134] W. Beenakker, W. L. van Neerven, R. Meng, G. A. Schuler, and J. Smith, "QCD Corrections to Heavy Quark Production in Hadron–Hadron Collisions", *Nucl. Phys.* **B351** (1991) 507–560.

[135] D. Dicus and S. Willenbrock, "Higgs Boson Production From Heavy Quark Fusion", *Phys. Rev.* **D39** (1989) 751.

[136] D. Dicus, T. Stelzer, Z. Sullivan, and S. Willenbrock, "Higgs Boson Production in Association With Bottom Quarks at Next-to-Leading Order", *Phys. Rev.* **D59** (1999) 094016, `hep-ph/9811492`.

[137] R. M. Barnett, H. E. Haber, and D. E. Soper, "Ultraheavy Particle Production from Heavy Partons at Hadron Colliders", *Nucl. Phys.* **B306** (1988) 697.

[138] F. I. Olness and W.-K. Tung, "When is a Heavy Quark Not a Parton? Charged Higgs Production and Heavy Quark Mass Effects in the QCD Based Parton Model", *Nucl. Phys.* **B308** (1988) 813.

[139] M. Spira. Private communication.

[140] G. P. Lepage, "A New Algorithm for Adaptive Multidimensional Integration", *J. Comput. Phys.* **27** (1978) 192.

[141] J. Hilgart, R. Kleiss, and F. Le Diberder, "An Electroweak Monte Carlo for Four Fermion Production", *Comput. Phys. Commun.* **75** (1993) 191–218.

[142] F. A. Berends, R. Pittau, and R. Kleiss, "All Electroweak Four Fermion Processes in Electron–Positron Collisions", *Nucl. Phys.* **B424** (1994) 308–342, `hep-ph/9404313`.

[143] R. Kleiss and R. Pittau, "Weight Optimization in Multichannel Monte Carlo", *Comput. Phys. Commun.* **83** (1994) 141–146, `hep-ph/9405257`.

[144] A. Denner, S. Dittmaier, M. Roth, and D. Wackeroth, "Predictions for all Processes $e^+e^- \to 4\,\text{fermions} + \gamma$", *Nucl. Phys.* **B560** (1999) 33–65, `hep-ph/9904472`.

[145] W. Beenakker and A. Denner, "Infrared Divergent Scalar Box Integrals with Applications in the Electroweak Standard Model", *Nucl. Phys.* **B338** (1990) 349–370.

[146] G. 't Hooft and M. J. G. Veltman, "Scalar One Loop Integrals", *Nucl. Phys.* **B153** (1979) 365–401.

[147] A. Denner, U. Nierste, and R. Scharf, "A Compact Expression for the Scalar One Loop Four Point Function", *Nucl. Phys.* **B367** (1991) 637–656.

Acknowledgments

First of all I thank my advisor Peter M. Zerwas for offering me the opportunity to do my thesis on a very interesting topic within an encouraging environment.

I would like to thank Wim Beenakker, Stefan Dittmaier, Michael Krämer, and Michael Spira for a pleasant collaboration. They have performed completely independent calculations for most of the results presented in this thesis. In addition I am grateful to Michael Krämer, Michael Spira, and especially Stefan Dittmaier for reading the manuscript and giving me plenty of valuable suggestions.

Special thanks to Stefan Dittmaier for his help in every-day life. I have profited a lot from his advice.

I would also like to thank Milada Margarete Mühlleitner, Markos Maniatis, Markus Weber, and Ayres Freitas for the kind atmosphere in our office, as well as the whole DESY theory group for the pleasant working environment.

Muchisimas gracias a Amaya López-Durán Viani. Conocerle es el resultado más importante de los tres años pasados.